INFORMATION TO USERS

This manuscript has been reproduced from the microfilm master. UMI films the text directly from the original or copy submitted. Thus, some thesis and dissertation copies are in typewriter face, while others may be from any type of computer printer.

The quality of this reproduction is dependent upon the quality of the copy submitted. Broken or indistinct print, colored or poor quality illustrations and photographs, print bleedthrough, substandard margins, and improper alignment can adversely affect reproduction.

In the unlikely event that the author did not send UMI a complete manuscript and there are missing pages, these will be noted. Also, if unauthorized copyright material had to be removed, a note will indicate the deletion.

Oversize materials (e.g., maps, drawings, charts) are reproduced by sectioning the original, beginning at the upper left-hand corner and continuing from left to right in equal sections with small overlaps.

Photographs included in the original manuscript have been reproduced xerographically in this copy. Higher quality 6" x 9" black and white photographic prints are available for any photographs or illustrations appearing in this copy for an additional charge. Contact UMI directly to order.

Bell & Howell Information and Learning
300 North Zeeb Road, Ann Arbor, MI 48106-1346 USA

UMI®
800-521-0600

ESL-TH-00-08-03

MODELING OF REFRIGERANT FLOW THROUGH FLEXIBLE SHORT TUBE ORIFICES

A Dissertation

by

RAMADAN BASSIOUNY MOHAMED ABDEL GHANI

Submitted to the Office of Graduate Studies of
Texas A&M University
in partial fulfillment of the requirements for the degree of

DOCTOR OF PHILOSOPHY

August 2000

Major Subject: Mechanical Engineering

MODELING OF REFRIGERANT FLOW THROUGH FLEXIBLE SHORT TUBE ORIFICES

A Dissertation

by

RAMADAN BASSIOUNY MOHAMED ABDEL GHANI

Submitted to Texas A&M University
in partial fulfillment of the requirements
for the degree of

DOCTOR OF PHILOSOPHY

Approved as to style and content by:

Dennis L. O'Neal
(Chair of Committee)

N. K. Anand
(Member)

Y. Hassan
(Member)

H. Hogan
(Member)

Suhada Jayasuriya
(Head of Department)

August 2000

Major Subject: Mechanical Engineering

ABSTRACT

Modeling of Refrigerant Flow through Flexible Short Tube Orifices. (August 2000)

Ramadan Bassiouny Mohamed Abdel Ghani,

B.S., Minia University; M.S., Minia University

Chair of Advisory Committee: Dr. Dennis L. O'Neal

Single-phase flow of refrigerants R-22, R-134a, and R-410a through flexible short tube orifices with three different geometries and a range in upstream operating conditions was modeled using the finite element method, FEM. A commercial package, ANSYS with its CFD counterpart, FLOTRAN, was used. Three tube moduli of elasticity, 5513 kPa (800 psi), 7084 kPa (1028 psi), and 9889 kPa (1435 psi) with three different L/D ratios as 5.5, 6.4, and 11.2 were investigated. The predicted mass flow rate values were compared to available published experimental results.

The study showed that upon deformation, the short tube resembled the shape of a converging-diverging nozzle. Both tube inlet and outlet had a chamfered-like shape after deformation which reduced the sharp pressure drop at the tube inlet. The less modulus the tube, the larger chamfered-like angle at the inlet. Further, the more flexible tube, the higher pressure drop along the tube due to the higher tube contraction.

The mass flow rates estimated with the numerical model were 14% over those from the experimental results. The model also indicated a pressure dip due to the

contraction in the tube area just downstream of the vena-contracta region. The results illustrate that as the upstream pressure increased by 45%, the tube area deformed by 35-60% related to the tube geometry. The study showed that the more flexible tube restricted the mass flow rate by 2-6% less than the less flexible tube depending on the upstream pressure.

A non-linear correlation to estimate the flow rate of a single-phase flow through flexible short tubes was predicted based on the model results. The percentage difference between the predicted mass flow rate and the experimental results was 13%.

The tube deformed more in the case of R-410a and less in the case of R-134a compared to R-22 at the same condensing temperature, 46.2 °C. R-410a showed a higher mass flow rate than R-22; while R-134a showed less variation in flow rate compared to R-22. This can be attributed to the higher pressure differential in case of R-410a compared to R-134a, and R-22 at the same condensing and evaporating temperatures.

To all my teachers and whoever has a right on me,

To the dear departed, to the soul of my beloved brother, *TAREQ,*

To my beloved parents; my Father and my Mother,

To my beloved brother, YASER,

To the soul of my father-in-law,

To my mother and my brothers-in-law,

To my dear family; my wife, and my beautiful and cheerful kids,

ESRA' and TAREQ.

ACKNOWLEDGEMENTS

Glory is to Allah Almighty, the lord of the world and blessings upon his beloved messenger and prophet, Muhammad (peace be upon him). All praise is due to Allah for granting me the power and will, relieving me during hard times, and helping me throughout my whole life.

I would like to express my sincere gratitude and appreciation to my committee chair, Dr. Dennis L. O'Neal, for his sincere help and encouragement through the study. His outstanding supervision and continuous cooperation helped me a great deal in overcoming the research problems. I really appreciate his style of supervision and manner in dealing with his students.

I wish to express my deep thanks to my advisory committee, Dr. N. K. Anand, Dr. Yassin Hassan, and Dr. Harry Hogan. Their cooperation and support during the study is really impressive. My appreciation and warm thanks to Dr. Ben Welch for his kindness and taking the time to be my graduate council representative. I really appreciate working with the chair and members of my advisory committee.

I also would like to thank Mr. Rich Lange from ANSYS Inc. for helping me in understanding the code. My appreciation to Ms Kim Moses, Graduate Program Advisor, for facilitating any administrative requirements.

Finally, I must express my deep thanks, love, and appreciation to my father, mother, brother, mother-in-law, and brothers-in-law for their continuous prayers and support. I also express my sincere gratitude and gratefulness to my wife for her patience and support for bearing the responsibility during our four years at Texas A&M University, and for taking care of our two lovely kids, Esra' and Tareq.

I would like to thank all my friends here with whom I dealt. I enjoyed the time and benefited from their experience. They helped me feel at home and sped up the long days I endured during my study. May Our Lord bless and reward all those with whom I have been dealing.

NOMENCLATURE

A	Orifice area, m^2
C_c	Orifice constant
Cp	Specific heat at constant pressure, kJ/(kg K)
D	Short-tube diameter, m
E	Modulus of elasticity, kPa (psi)
G	Mass flux, kg/(m^2 h)
g_{ca}	Dimension gravity constant, 1.296×10^{10} (s^2.N/(h^2.kN))
h	Enthalpy, kJ/kg
K	Thermal conductivity, W/(m K), turbulence kinetic energy, m^2/s^2
k	Slip ratio (V_g/V_f)
L	Short-tube length, m
L/D	Length over diameter ratio of short-tube
P	Pressure, kPa
Q	Heat generation, W/m^3
T	Temperature, K
U	Displacement, m, Velocity vector, m/s
V	Fluid velocity, m/s
v	Specific volume, m^3/kg,
x_i	Global coordinates system
x	Fluid quality

Greek symbols

μ	Dynamic viscosity, $N/(m^2. S)$
δ	Distance from the wall, m
ρ	Fluid density, kg/m^3
τ	Shear stress, N/m^2
ν_t	Turbulence kinematics viscosity, m^2/s
ν	Poisson Ratio
σ_k, σ_ε	Turbulence Prandtle numbers
σ	Stress, N/m^2
ε	Strain, turbulence kinetic energy dissipation rate, m^2/s

Subscripts

Cr	Critical
down	Downstream
f	Saturated liquid
g	Saturated vapor
nw	Near wall
ref	Reference
sat	Saturation
tan	Tangential
th	Thermal, throat
up	Upstream

TABLE OF CONTENTS

LIST OF TABLES

LIST OF FIGURES

FIGURE Page

FIGURE Page

FIGURE Page

FIGURE Page

FIGURE Page

CHAPTER I

INTRODUCTION

The past decade has been a challenging time for the refrigeration industry worldwide. Stratospheric ozone depletion and global warming are two critical problems which are mostly related to the use of chlorofluorocarbons (CFCs) and hydrocloro-fluorocarbons (HCFCs) in refrigeration and air conditioning applications. International agreements have been held to discuss a remedy for these problems. The Montreal Protocol and its amendments require the phase-out of CFCs and HCFCs compounds that have been extensively used as refrigerants in heat pumps, air conditioners and refrigeration systems. The Kyoto Protocol requires accelerated reduction of emission of HCFCs to minimize the potential risk of excessive global warming (Baxter et al 1998).

To design a high efficiency refrigeration system, performance data for the behavior of the new refrigerants through each component in the system is needed. As the transition from CFCs and HCFCs to hydrofluorocarbons (HFCs) progresses, efforts are increased and research is underway to evaluate the performance of the new refrigerants in refrigeration and air conditioning systems.

This dissertation follows the style and format of the *ASHRAE Transactions.*

The basic components of an air conditioner or a heat pump include a compressor, condenser, expansion device and evaporator. A schematic of the refrigeration cycle along with a pressure-enthalpy diagram of the cycle is shown in Figure 1.1. In this cycle, the refrigerant leaves the evaporator in the vapor phase after receiving the thermal load to the compressor which pumps the vapor to the condenser. While flowing through the condenser, the refrigerant rejects heat to the surroundings and changes to a liquid phase. Leaving the condenser, the liquid refrigerant exhibits a large pressure drop while expanding through the expansion device. The expansion process, 3-4, is found in all vapor compression refrigeration and air conditioning systems. The refrigerant partially flashes to vapor inside the expansion device due to a large pressure drop through the expansion process and produces a two-phase flow mixture at the exit. If there is uncondensed vapor from the condenser, a low quality refrigerant enters the expansion device (process 3′-4′) which allows less mass flow through the expansion device. Conversely, if the refrigerant entering the expansion device receives a large amount of subcooling (process 3"-4"), the mass flow rate through the expansion device becomes larger than process 3-4. Processes 3′-4′ and 3"-4" can result from an improperly sized expansion device, rapidly changing conditions such as start up, or an excessive or light thermal load in the evaporator.

Although it is of simple construction, the expansion device is very important to the control of the refrigeration system. It is used to control the mass flow and to produce the desired pressure differential across the compressor. Further, the expansion device

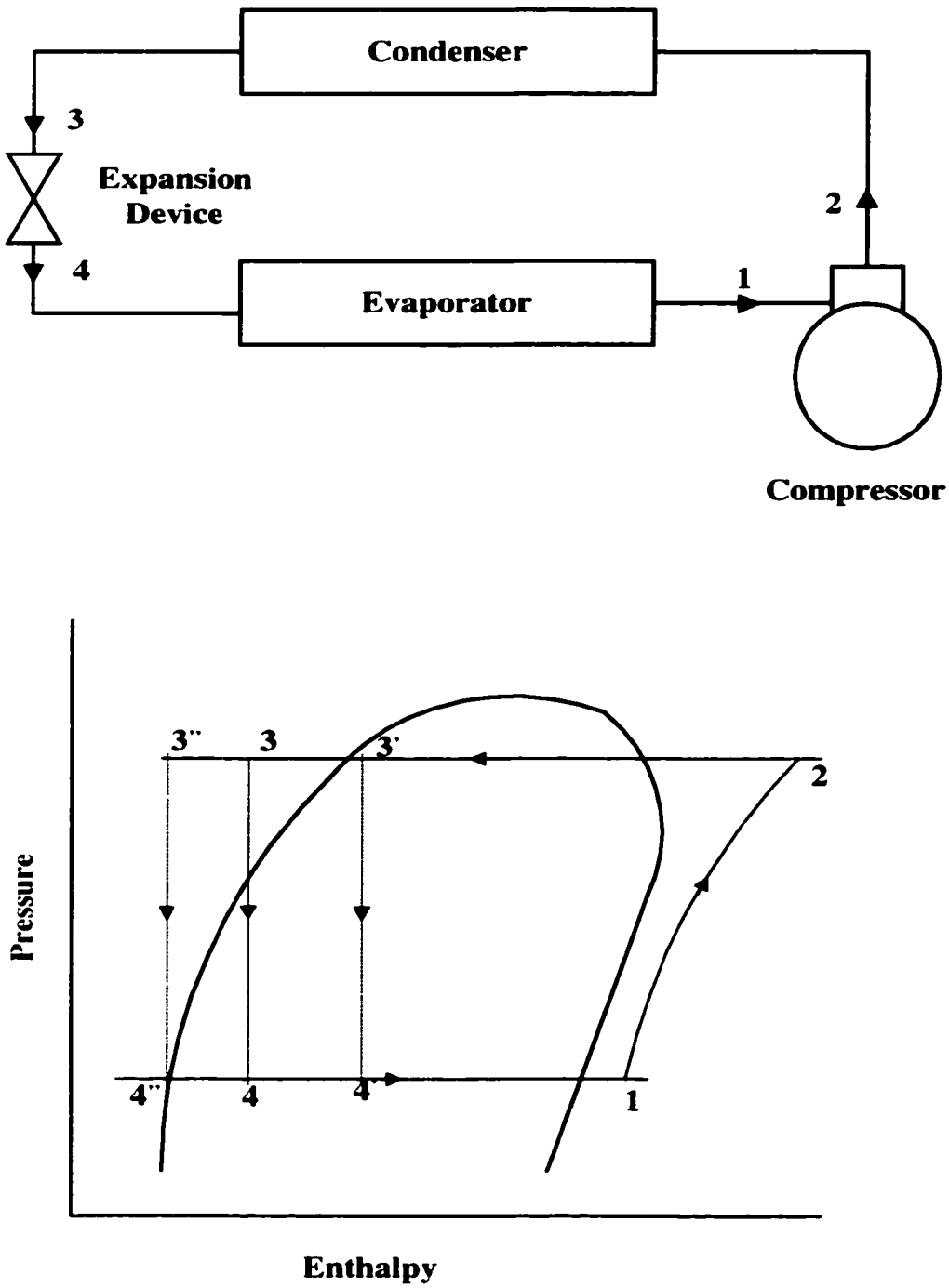

Figure 1.1 A Schematic of the Refrigeration Cycle with a Corresponding Flow Regimes Diagram.

can protect the compressor by maintaining superheated vapor at the inlet of the compressor (Drucker 1992).

The most widely used expansion devices are classified into variable flow area devices such as thermal expansion valves, (TXVs), and constant flow area such as capillary tubes, and short-tube orifices. All expansion devices perform the same basic function even though each may operate in a slightly different manner. TXVs control the refrigerant flow based on the superheat of the refrigerant leaving the evaporator. A sensing bulb that is located at the evaporator exit senses the leaving refrigerant temperature and based on this temperature, the expansion valve changes its cross-sectional area to adjust the refrigerant flow rate. The TXV is responsive to changes in loads; however, it is an expensive compared to either capillary tubes or short tube orifices (Drucker 1992, Drucker and Conn 1991, Drucker and Abbott 1993).

Capillary tubes are often used in small applications such as domestic refrigerators. Although capillary tubes are simple and inexpensive, they have limited performance if the system has to operate over wide range of temperature or loads (Drucker 1992).

Traditionally, short tube orifices, which have length to diameter (L/D) ratios ranging from 3-20, are rigid with either constant inner diameter or have a small change in inner diameter from inlet to outlet (Kim 1993). A simple schematic for the rigid short tube is shown in Figure 1.2. A rigid short tube controls flow rate by throttling refrigerant from the high pressure side to the low pressure side, (Kim 1993). Rigid short

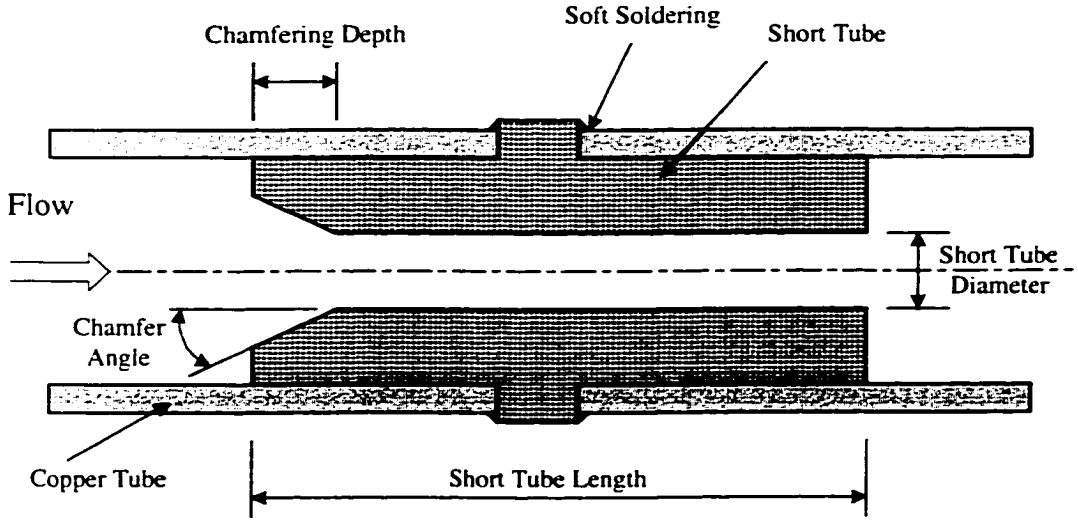

Figure 1.2 A Schematic of a Rigid Short-Tube Orifice.

tube orifices are as cheap as capillary tubes and produce the desired pressure differential across the compressor. They are not capable of controlling flow as well as TXVs over a wide range of conditions. Hence, rigid short tubes still have some of the same limitations as capillary tubes.

In 1992, Drucker patented a flexible short tube orifice (Figure 1.3), which could be used as an expansion device in heat pumps. This flexible orifice is capable of changing its flow cross sectional area as the upstream pressure in the system changes. It controls the refrigerant flow in response to the change in the upstream pressure of the system. The orifice is made of an elastomeric expansion device. The deformation decreases the orifice diameter which helps control the flow through the orifice.

The advantage of the flexible orifice over the rigid one is that it can provide better flow control by varying its cross sectional area in response to the pressure change across the compressor. When the condenser pressure increases due to an increase in the ambient temperature above the system design point, a rigid orifice sometimes provides a high enough flow rate to flood the compressor with saturated refrigerant. When the condenser pressure decreases due to a decrease in the ambient temperature, a rigid orifice passes a lower refrigerant flow rate which can produce high superheating leaving the evaporator. A saturated liquid-vapor mixture can damage valves in some compressors while too high superheat reduces compressor capacity and produces excessively high discharge temperature.

It is crucial for the designer to have a better insight into the performance of the flexible short tube orifice while under a range of operating conditions. The present study focuses on flow of different refrigerants through flexible short tube orifices. The study includes a review of the available and related literature, numerical modeling and validation, numerical results and discussion, and mass flow rate predicted correlation. Chapter II summarizes the previous available researches on flow of saturated water, R-12 , R-22, and R-134a through short tube orifices and restrictors in addition to critical

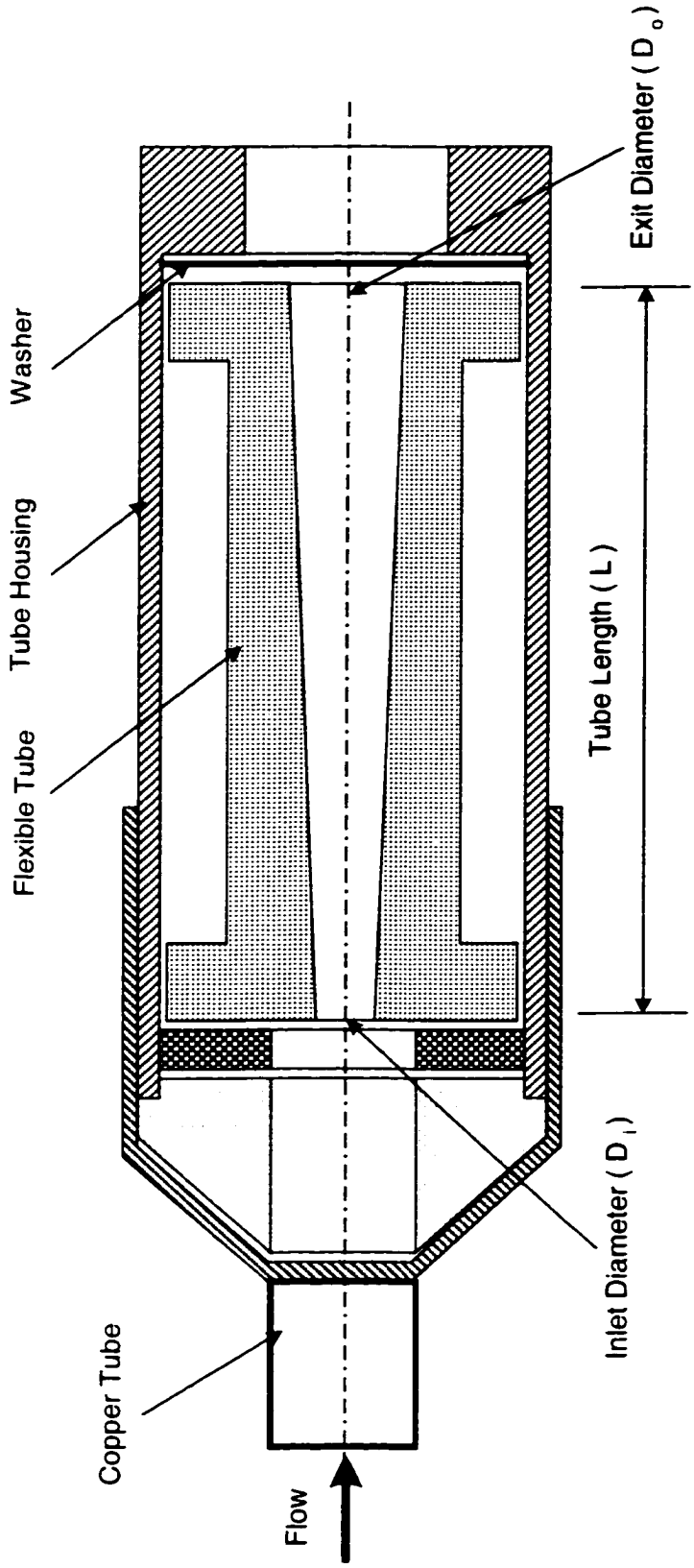

Figure 1.3 A Schematic of the Flexible Short-Tube Orifice Test Section with Downstream Washer.

phase flow. The numerical, FEM, model and the computational domain are introduced in Chapter III. Chapter IV shows a comparison between available published experimental data collected by (Kim 1993) for rigid short tubes as well as some data for flexible short tubes with the numerical results. The complete numerical results and discussion of R-22 single phase flow through flexible short tubes are presented in Chapter V. A predicted mass flow rate correlation to calculate the mass flow through flexible orifices is given also in Chapter V. Results of Flow of R-134a and R-410a through flexible short tube orifices are presented in Chapter VI. Finally, conclusions and recommendations are given in Chapter VII.

CHAPTER II

LITERATURE REVIEW

The short tube orifice is used by U.S. heat pump manufactures because of its low cost, ease of installation, low maintenance, and high reliability. Two phase refrigerant flow behavior through the orifices was a major focus of several previous studies: Mei (1982), Krakow and Lin (1988), Aaron and Domanski (1990), Kuehl and Goldschmidt (1992), Kim (1993), Kim and O'Neal (1994a, 1994b, 1995). These studies dealt with flow behavior, flow metastability, or mass flow-rate modeling for single and two-phase flow of refrigerants. They considered different operating conditions that include inlet subcooling/quality, upstream and downstream pressure, and inlet and exit edge shape. Older studies such as Sajben (1961), Zaloudek (1963), Starkman et al (1964), Levy (1965), Moody (1965), Henry and Fauske (1971), Wallis (1980), have focused on two-phase critical flow modeling of different fluids. The literature can be divided into three sections: (1) flow behavior in short tube restrictors, (2) mass flow rate modeling, and (3) critical two-phase flow. Each is summarized below.

Flow Behavior in Short Tube Restrictors

Flow through short tube restrictors is complicated because it combines turbulence, choked, and two-phase flow. Recalling the function of the short tube restrictors as expansion devices, a rapid depressurization mainly occurs at the tube inlet due to abrupt change in the cross sectional area. This rapid drop in pressure is

accompanied with flow acceleration that accordingly results in thermodynamic metastable flow.

Zaloudek (1963) mentioned that the rapid expansions produced in orifices and short tubes resulted in metastable flow. This metastability was characterized by a failure of the two-phase mixture to attain equilibrium conditions during flashing in the region of rapid depressurization. The metastability phenomenon was comprehensively discussed by others such as Bailey (1951), Fauske (1962), Mikol (1963), Mei (1982), Aaron and Domanski (1990), Kim (1993), and Kim and O'Neal (1994a, 1994b). Bailey (1951) discussed the metastability of upward adiabatic, saturated and nearly saturated flow of water in four different L/D ratios of short tubes. He presented the flow characteristics curves of the tube. Three different well-defined regimes were observed. Zaloudek (1963) observed the same flow regimes as shown in Figure 2.1. In the first regime, curve AB, the flow follows the conventional single-phase flow $G^2 \alpha \Delta P$ characteristic. The shift or discontinuity in the flow curve at B occurs because the pressure at the vena contracta has reached the saturation pressure corresponding to the inlet temperature and the relationship between flow and pressure differential became unstable. He added that visual observation demonstrated that the flow had completely separated from the wall of the tube at C and was apparently annular in form. Increasing the pressure differential led to the reestablishment of the $G^2 \alpha \Delta P$ characteristic again, curve CD. At the point D, Bailey (1951) and Zaloudek (1963) observed the establishment of a choking phenomenon, which resembled gaseous critical flow. Any further increase of the

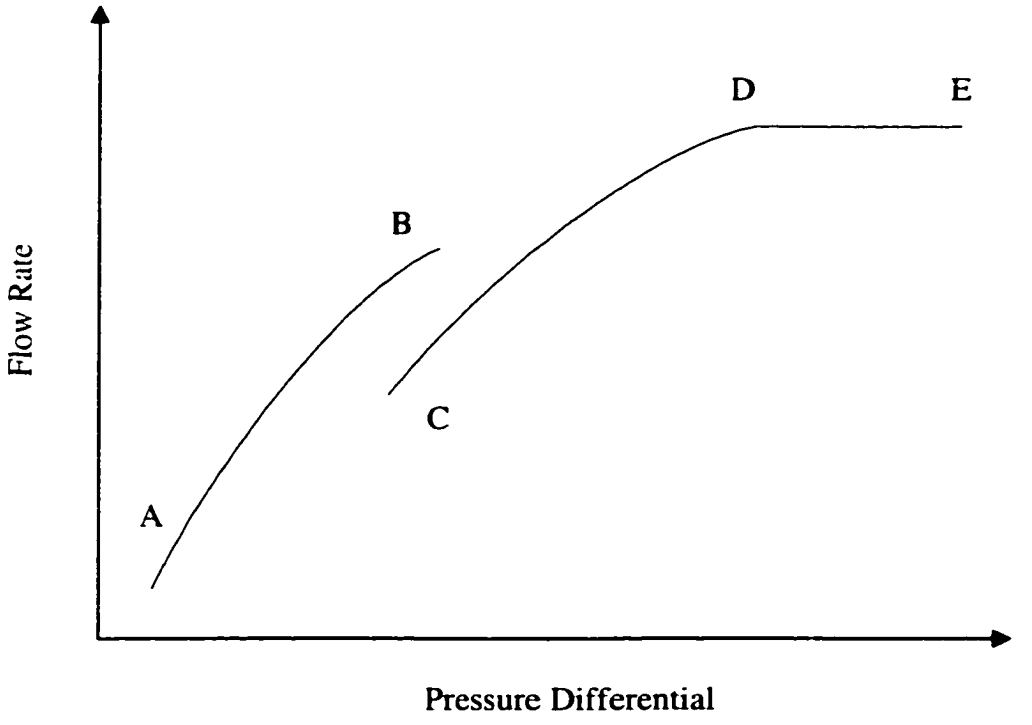

Figure 2.1 The Characteristic Curves of Flow through Short-Tube Orifices.

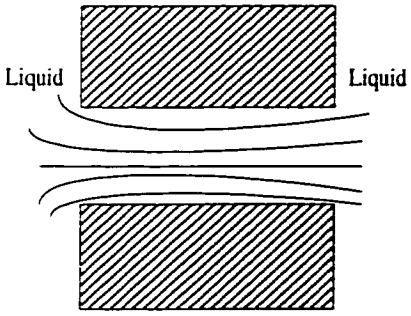

Regime (AB) Liquid at all points

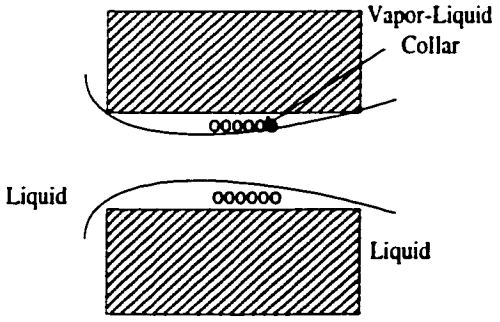

Regime (BC) Vapor-Liquid Collar (upstream chocking)

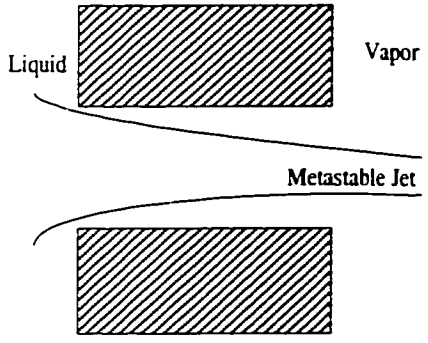

Regime (CD) Free Discharge of Metastable Liquid

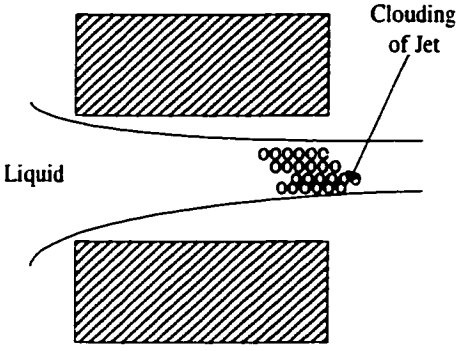

Regime (DE) Downstream Chocking

Figure 2.2 A Schematic Plot for the Four Regimes Shown in the Flow Characteristic Curves, Zaloudek (1963).

pressure differential beyond point D no longer affected the mass flow rate, curve DE. These four regions are schematically depicted in Figure 2.2.

Zaloudek observed that the inception of these flow regions in the characteristic appeared to be path independent. He explained that these four regions can be equally produced by increasing the downstream pressure to the desired value. Mikol (1963) observed choked flow and noted that as long as the flow temperature remained constant, the fluid remains liquid and the pressure drop remains approximately linear. The effect of subcooling on choked flow at the vena contracta was experimentally studied by Mei (1982) using R12. He reported that for L/D ranging from 7.5 to 11.9, the first choking, vena contracta choking, was shown when the level of subcooling was in the range of $19.4<\Delta T<22.2$ °C. However, he did not observe the second choking, exit choking, caused by liquid flashing at the tube exit as did Bailey (1951) and Zaloudek (1963).

The sharp edge at the inlet of the short tube orifice significantly affects the pressure drop through the orifice, and consequently the mass flow rate. Krakow and Lin (1988) attributed the pressure drop across a fluid element to three effects: specific volume variation, which results primarily from a change of the refrigerant quality, cross-sectional area variation, and viscosity (wall friction). The effect of tube inlet and exit chamfering was investigated by Aaron and Domanski (1990), Kuehl and Goldschmidt (1992), Kim (1993), and Kim and O'Neal (1994a, 1994b). Aaron and Domanski (1990) reported that 45^0 chamfering at the tube inlet caused a 5%-25% increase in the mass flow rate depending on the L/D ratio and chamfering depth. Chamfering at the tube exit had

no appreciable effect on the mass flow rate. This was also noticed by Kim and O'Neal (1994a, 1994b). They reported that inlet chamfering increased the flow rate from 5-20% compared to the sharp-edged short tubes. However, the increase in flow rate accomplished by changing the chamfer depth was less than 7% for two-phase flow entering the short tube.

The effect of reducing the downstream pressure on the pressure distribution inside the tube was noticed by Aaron and Domanski (1990) and Kim (1993). Although their operating conditions were different, they reported that when the downstream pressure was reduced, the pressure everywhere inside the tube was also reduced. Aaron and Domanski (1998,1990) found that the tube diameter was the strongest variable in determining the flow rate. They mentioned that the mass flow rate was proportional to the short tube diameter, D^C, where c is found to be 2.11 for sharp-edged diameters, and 2.02 for chamfered inlet short-tubes. This was affirmed by Kuehl and Goldschmidt (1992) as well. They developed empirical correlations that related mass flow rate to upstream pressure, P^n, while the index, n ranged from 0.177 to 0.787 for different tube size and geometry. Their results showed that the mass flow rate increased with increasing the tube diameter and flow inlet subcooling. Kim and O'Neal (1995) reported that the mass flow rate was extremely sensitive to changes in short tube diameters. Based on their experimental data, they found that the mass flow rate was approximately proportional to D^2. The same authors (1994) showed that for upstream quality over 4%, the flow rate was almost linearly proportional to the tube diameter.

Mass Flow Rate Modeling

Models may be analytical, empirical, or semi-empirical. An analytical model is based on a rigorous theoretical analysis, and may require excessive computing time. An empirical model may be based on curve fitting of experimental data. The coefficients in an empirical model may not have any physical significance. Semi-empirical models are based on theoretical analysis but include experimentally determined coefficients that may have physical significance. Semi-empirical models are best suited for inclusion in heat pump simulation programs (Krakow and Lin 1988).

Davies and Daniels (1973) developed semi-empirical correlations that took into consideration the effect of upstream and downstream quality and pressure on the mass flow rate. They mentioned that in case of pure liquid flow, a static pressure recovery behind the orifice was fully established at a distance of 15.9 diameters. The recovery falls very sharply with increased vapor generation. Based on these correlations, they plotted the variation of mass flow rate versus downstream quality. The plot showed that increasing the downstream quality reduced the mass flow rate. Davies and Daniels (1973) were not able to measure the temperature downstream of the tube due to very small internal diameters of the tested tubes.

Mei (1982) presented a semi-empirical model that related the mass flow rate to the pressure differential between the upstream pressure and the saturation pressure based on the upstream temperature. This model predicted the mass flow rate for only liquid subcooling equal to 22.2 °C or less. However, for subcooling higher than 22.2 °C, he

introduced a modified first-stage choking model. The use of these two models was limited to the range 7.5<L/D<11.9 and for only liquid flow entering the orifice.

Kim and O'Neal (1994a, 1994b) developed a semi-empirical correlation to predict the mass flow rate before the flashing point as a function of both the upstream and saturation pressure. In their model, they modified the orifice single-phase flow equation by introducing two new parameters: two-phase flow constant, and pressure before flashing in place of downstream pressure. They correlated the pressure before flashing to the saturation pressure and obtained the coefficients in the correlation experimentally. The model is given as:

$$M = C_c A_s \sqrt{2 g_{ca} \rho (P_{up} - P_f)} \tag{2.1}$$

where;

$$P_f = P_{sat} \left\{ \begin{array}{c} 1.005 + 5.7367 (P_{up}/P_{Cr})^{-0.485} (L/D)^{-0.179} SUBC^{0.9948} + 0.268 (P_{up}/P_{Cr})^{2.716} \\ -0.226 \, Exp(-0.021 (D/D_{ref}) (L/D))^2 - 0.092 \, EVAP \end{array} \right\}$$

$SUBC = (T_{sat} - T_{up})/T_{Cr}$,

$EVAP = (P_{Cr} - P_{down})/P_{Cr}$, and

T and P are absolute Temperature and Pressure, respectively.

Kim and O'Neal (1994a, 1994b) found that the reduction in the downstream pressure caused a corresponding reduction in the downstream temperatures due to the fact that the downstream is saturated. Consequently, the heat transfer along the tube

would delay the onset of flashing inside the orifice. Hence, this would tend to increase the mass flow.

A numerical model was developed by Krakow and Lin (1988) that was based on assuming that when the upstream refrigerant was subcooled, the exit plane of the orifice was saturated liquid, and when the upstream refrigerant was two-phase, the exit plane was sonic. They justified the validity of their model by experimental data.

Goldstein (1981) presented a mathematical iterative approach to modeling flashing flow in small diameter tubes. In this approach, the solution started by assuming a pressure drop over the tube length and solved for the flow rate iterativelly until the calculated pressure drop equaled the assumed value.

A flexible short tube orifice, which was capable of changing its flow cross sectional area as the upstream pressure in the system changed was patented by Drucker and Cann (1991), Drucker (1992), and Drucker and Abbott (1993). The orifice worked efficiently in the overall system. However, there was no study either on the flow structure inside the orifice or on the flexible orifice surface deformation. Therefore, comprehensive information about the flow behavior through the flexible orifice and surface deformation was needed.

One related experimental study on flexible short tubes was found, which was done by Kim et al (1996). In this study, the authors experimentally evaluated the overall performance of two flexible short tube orifices with two different moduli of

elasticity, 7084 kPa (1028 psi), and 9889 kPa (1435 psi). The tests included a range of operating variables such as inlet subcooling/quality, upstream pressure, and downstream pressure. They observed that the mass flow rate through the flexible orifices was strongly dependent on the modulus of elasticity of the material and on upstream pressure. Further, Kim et al (1996) concluded that, with using two washers upstream and downstream, the more flexible orifice produced less flow than the less flexible orifice as the upstream pressure was increased. However, by removing the upstream washer, the flow trend reversed. The same study focused on mass flow dependency on upstream conditions. A semi-empirical correlation was developed by Kim et al (1996) to predict the mass flow rate through flexible short tube orifices before flashing. This correlation was based on the single phase, single component orifice equation:

$$M = A_s \sqrt{2 g_{ca} \rho (P_{up} - P_f)} \qquad (2.2)$$

where;

$$P_f = P_{sat} \left\{ b_1 + b_2 \, PRA^{b3} \, SUBC^{b4} + b_5 \, EVAP^{b6} \right\}$$

and

$PRA = P_{up}/P_{Cr}$,

$SUBC = (T_{sat}-T_{up})/T_{Cr}$,

$EVAP = (P_{Cr}-P_{down})/P_{Cr}$,

T and P are absolute temperature and pressure, respectively.

The constants used in equation (2.2) are listed in Table 2.1 for two moduli of elasticity.

Table 2.1 Constants for the Semi-Empirical Correlation 2.2.

	E_1 7084 kPa (1028 psi)	E_2 9889 kPa (1435 psi)
b_1	0.9187	1.0434
b_2	10.4091	7.4048
b_3	-0.05	0.0191
b_4	1.1787	1.0421
b_5	-0.0276	-0.1683
b_6	0.9241	-0.7797

Kim et al (1996) made no observations on the effect of the upstream pressure on the flow behavior or tube deformation. The present study focuses on the orifice deformation and accordingly its effect on the flow behavior under different operating conditions.

Critical Two-Phase Flow

Two-phase critical flow phenomenon is significantly different from that of single-phase flow. In the latter, the critical discharge velocity is identical to the sonic velocity for flow of all liquid or vapor. However, two-phase critical flow is more complicated, since the velocities of the two-phases have their maximum values, but not identical to the sonic velocity in the same two media. A large number of models for

calculating critical flow have been presented and published. Theoretical models range all the way from the homogeneous equilibrium model (HEM), which is essentially a modified single phase technique, to models that attempt to represent all of the non-equilibrium two-phase phenomena in the short tube. Most of these models often apply the following equation proposed by Hsu and Graham (1976):

$$G_{Cr} = \left[\frac{-1}{\frac{\partial}{\partial P}\left\{ \frac{xk + (1-x)}{k} \left[(1-x)\, kv_f + xv_g \right] \right\}} \right]^{1/2} \qquad (2.3)$$

Mass, momentum, and energy transfer occur at the inter-phase. Henry and Fauske (1971) mentioned that these inter-phase processes determine the thermodynamic paths each phase follows during the expansion. The rate of evaporation, $\partial x / \partial P$, is determined by the interfacial mass transfer. The interfacial momentum estimates how fast each phase is accelerated, $\partial k / \partial P$. The specific volume change with respect to the pressure $\partial v_g / \partial P$ is determined from the interfacial energy transfer.

Kim and O'Neal (1995) presented a comparison to three groups of two-phase critical models: homogeneous equilibrium model (HEM), homogeneous frozen model (HFM), and non-homogeneous equilibrium model (NEM).

The HEM is considered the simplest model since the approach is to treat the two-phase mixture as a pseudo-fluid that can be described by the same equations as an equivalent single-phase flow (Wallis 1969 and 1980). This model is mainly based on the

assumptions: isentropic flow, equal average velocities for the phases (i.e. k=1), additive specific volumes, and thermodynamic equilibrium exists between the phases.

The HFM model assumes homogeneous flow but restricts the interfacial mass transfer between phases due to insufficient time for the process to occur. The model is based on the assumptions: homogeneous adiabatic flow with k=1, no mass transfer occurs between the phases, (i.e. $\partial x / \partial P = 0$), vapor expands isentropically as a perfect gas, kinetic energy in the stream all evolves from the vapor expansion, and critical flow rate follows the gas dynamic principles.

The NEM takes into consideration the effect of all three interfacial transports ($\partial v / \partial P, \partial x / \partial P, \partial k / \partial P$) assuming unequal velocities between phases (i.e. $k \neq 1$). It was based on deriving a relation for the slip ratio, k to calculate the critical mass flux.

Kim and O'Neal (1995) concluded that the HFMs provided the best agreement with the experimental results for a wide range of exit pressure except for the low-quality region ($x<0.06$). All the HEMs underpredicted the critical mass flow. Moreover, they mentioned that only the HFMs showed the physical realistic behavior that the critical discharge velocity increases as the outlet quality decreases to zero. The good agreement between the HFMs and the test data might be attributed to the well matching between the models assumptions and the flow conditions (Kim and O'Neal 1995).

Summary of the Literature

The tube geometry has a major influence on the mass flow rate. To build a high efficiency system, it is very crucial to evaluate the design and performance of its components. Mainly, the tube diameter plays a major role in predicting the mass flow in short tube restrictors. Thus, it is of great importance to have a better understanding about how the diameter of flexible orifices changes in response to pressure differential changes to better predict the mass flow.

Based on the literature, it can be concluded that the critical flow models are based on certain assumptions that the flow conditions have to match to accurately predict the flow rate. This works reasonably well with rigid short tubes rather than flexible short tubes. In flexible short tubes, the diameter changes according to upstream pressure change. Hence, the assumed restrictions may no longer exist as the shape changes.

A review of literature revealed that there were no comprehensive studies on either single-phase or two-phase flow through flexible short tube orifices. However, the literature showed extensive work on rigid short tube orifices. Having a comprehensive knowledge about the theory of operation and flow behavior through rigid orifice can be extremely helpful in understanding the performance of the flexible short-tubes. The motivation in investigating flexible short tube is that it might provide satisfactory overall system operating performance when tested experimentally. The importance of having an understanding about the refrigerant flow behavior through flexible short-tubes along

with the difficulties in measuring the pressure variation experimentally to depict the flow pattern inside these flexible tubes leads to the choosing of using a numerical technique.

CHAPTER III

NUMERICAL MODEL

Modeling flow through a flexible short tube orifice requires a methodology that can simulate the fluid-structure interaction and estimate changes in shape for the orifice as the upstream pressure changes. The finite element method, FEM, can be used to model the fluid-structure interaction problems. The basic advantage of the FEM over the other numerical techniques is that it allows for a flexible mesh which can be adjusted to the geometry of the problem. A finite element model for the problem was developed and solved using the Swanson Analysis System's FEM code, ANSYS, with its computational fluid dynamics, CFD, counterpart, FLOTRAN. The basic equations, modeling, and numerical procedure are described below.

Three different tube geometry configurations (Table 3.1) were investigated. Figure 3.1 shows the locations of particular dimensions on the flexible orifice.

Table 3.1 Short Tube Geometry Dimensions.

	L (mm)	$D_{i,in}$ (mm)	$D_{i,ex}$ (mm)	D_{fl} (mm)	t_{fl} (mm)	L/D^*
Model 1	14.5	2.06	2.46	9.5	2.5	6.42
Model 2	25.4	2.06	2.46	9.5	2.5	11.24
Model 3	14.5	2.46	2.86	9.5	2.5	5.45

$D^* = (D_{i,in} + D_{i,ex})/2$, $D_o = 5.9$ mm.

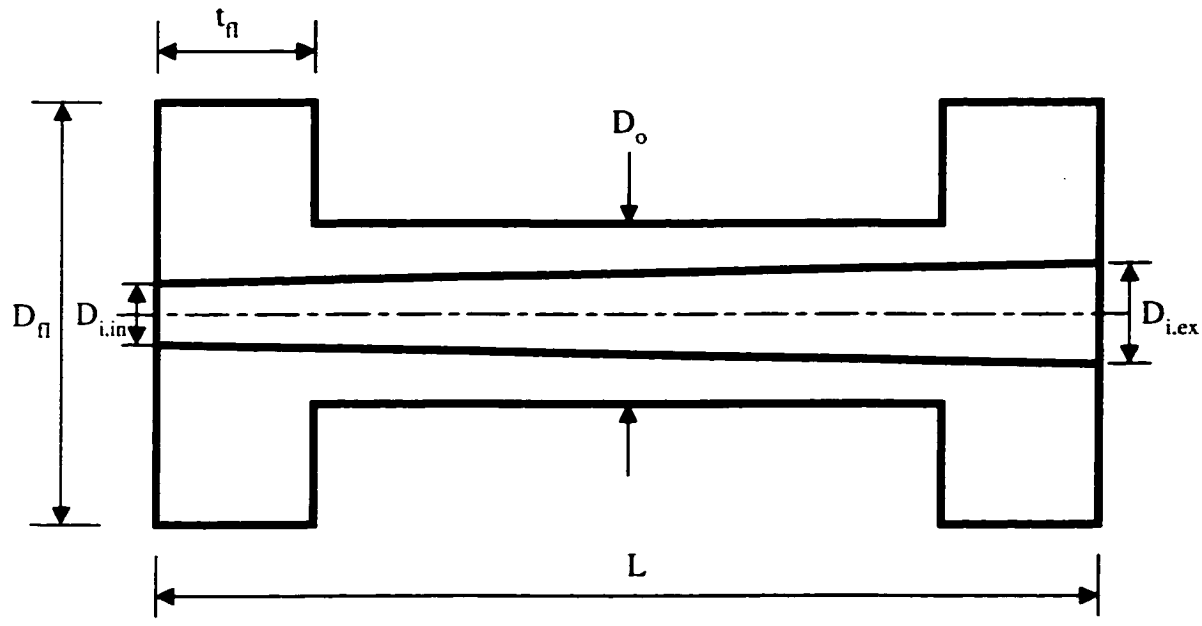

Figure 3.1 Flexible Short Tube Geometry.

The flexible short tube was designed with variable inner area as shown in Figure 3.1. The flexible orifice (L/D = 6.42) was experimentally tested by Kim et al (1996). Therefore, their data were chosen to validate the present numerical model. However, a preliminary investigation for a flexible orifice with a constant inner area was done because there were detailed experimental data that could be used to test the model and provide a comparison for the flexible orifice. This investigation showed that there was a slight pressure recovery very close to the inlet; however, there was no pressure recovery downstream of the tube inlet and the minimum cross sectional area occurred at almost

mid-length of the tube. Under high upstream pressures and/or very low modulus of elasticity, the flexible tube could collapse and overly restrict the flow.

For mesh generation, the choice of elements number, type (linear, quadratic), shape (triangular, rectangular), and density (mesh refinement) depended on a number of considerations. Reddy (1993) mentioned that engineering judgement was required in discretizing the problem domain with sufficiently small elements, so that steep gradients of the solution can be accurately calculated. He added that mesh refinement was required in places where acute changes in geometry, boundary conditions, loading, material properties or solution occurred. The axisymmetric mesh configuration for the tube geometry is shown in Figure 3.2. The figure shows three distinct regions. The first region, I, is called the fluid region which includes flow inlet and exit regions. The second region, II, is the axisymmetric flexible short tube body, and the third region, III, is the interaction region where the fluid interacts with the tube inner surface.

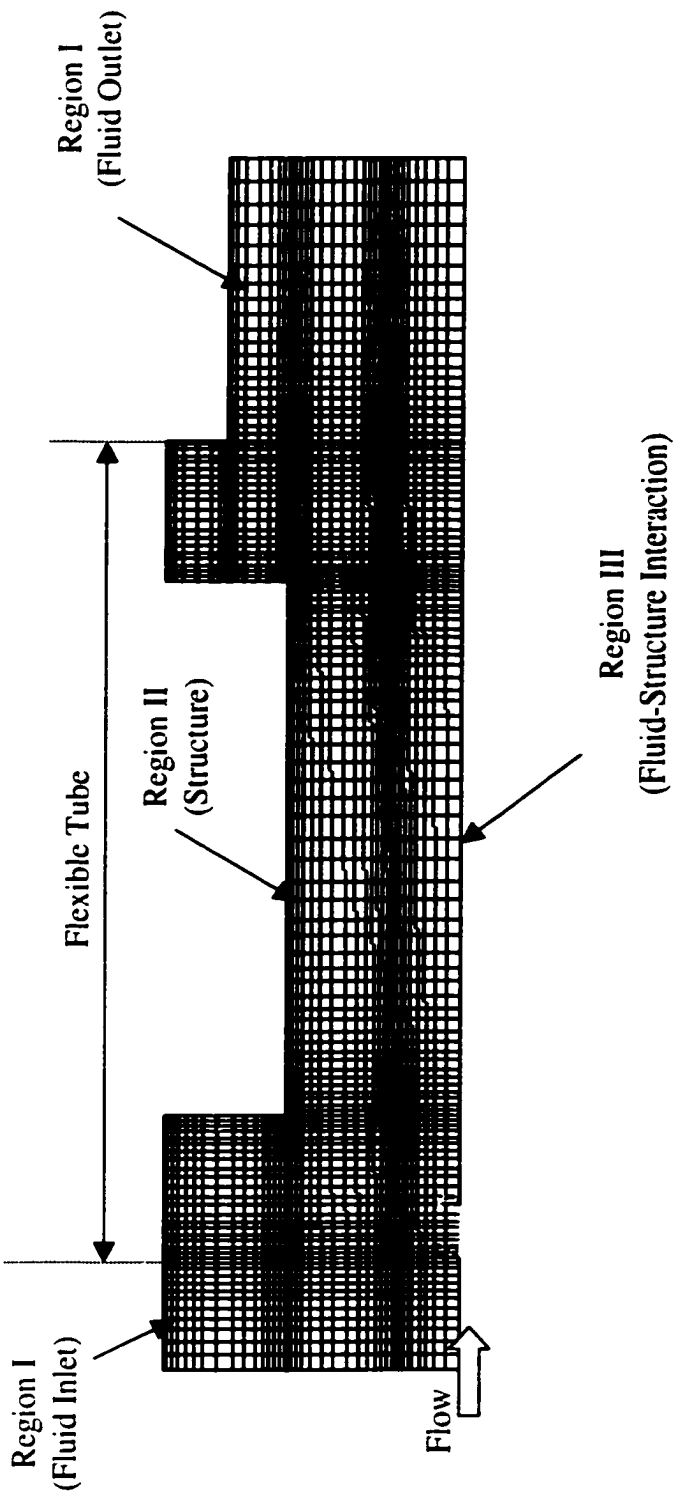

Figure 3.2 Axisymmetric Computational Domain for the Flexible Short Tube.

Quadrilateral elements (Figure 3.3) were chosen over triangular elements to better help in mesh refinement particularly near the walls. The axisymmetric mesh (Figure 3.2) is shown for the first geometrical configuration listed in table 3.1 which had a L/D of 6.42. A very fine mesh is used near the regions in which a steep gradient of the variable is expected to more accurately capture significant changes in variables such as velocity and pressure.

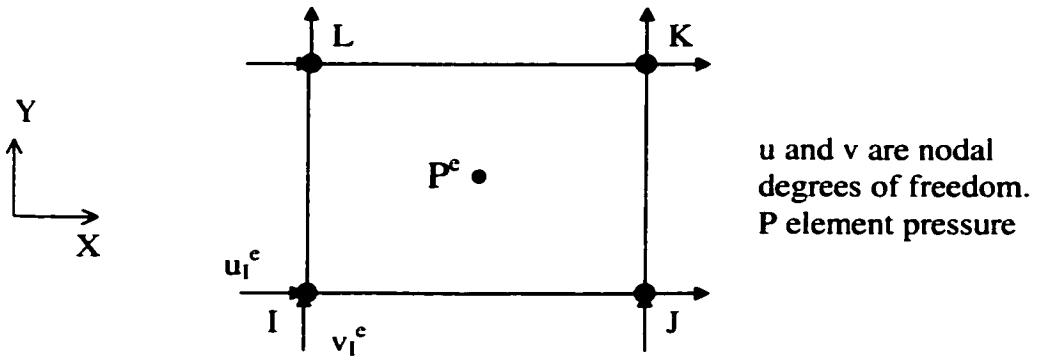

Figure 3.3 Quadrilateral Linear Element.

Grid Independent Solution

If the numerical method is stable and if all the approximations used in the discretization process are consistent, the solution converges to a grid independent solution (Ferziger and Peric 1997). To demonstrate grid independence, the solution was repeated on a series of successively refined grids until there was no significant change in the solution. The computational grid started with an initial number of elements (2858 elements) and proceeded to 3885 elements (2010 for the fluid domain and 1875 for the structure domain) with mesh refinement in the regions in which a steep gradient of the

variables was expected. An excessive increase of the number of nodes within the computational domain increases the round-off error; therefore unrealistic results might be obtained. Hence, there is an optimum number of nodes for which the error is minimum. The same procedure was implemented for the other two tube configurations. The 2-D quadrilateral mesh was (4510 elements) for model 2 listed in Table 3.1 with L/D of 11.24 and model 3 with L/D of 5.45.

Figure 3.4 (a) and (b) shows the pressure profile along the tube and at 3 mm from the sudden contraction section, respectively. As the mesh refinement proceeded, there was no significant change in the profile a long the tube, downstream of the sudden contraction. However, the sharp pressure drop at the tube inlet varied as the mesh refinement continued. Refining the mesh captured a larger sharp pressure drop at the tube inlet compared to the uniform mesh. Further, there was a 2% error in mass flow rate in the case of the refined mesh compared to the calculated mass flow rate based on the single-phase orifice equation.

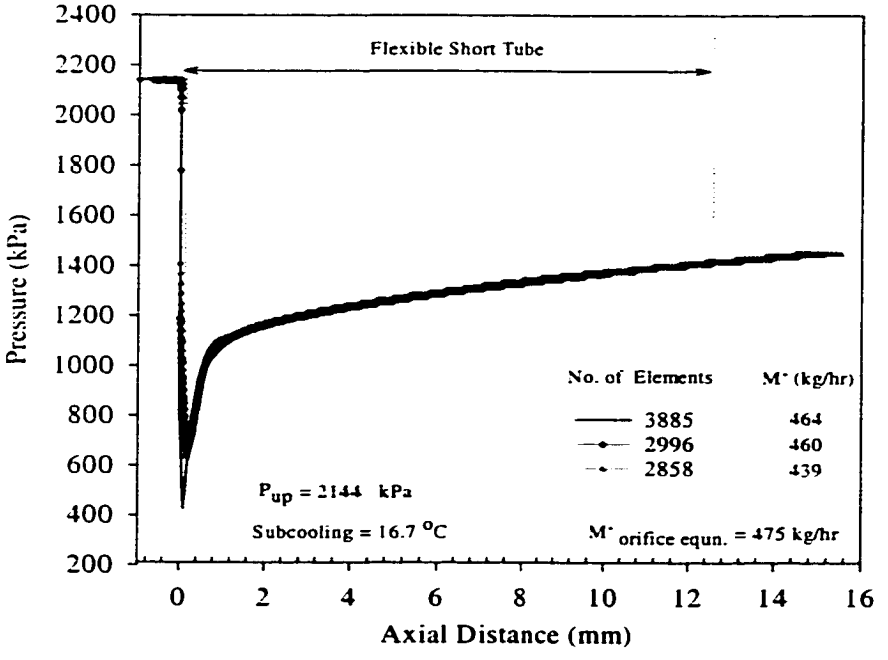

(a)

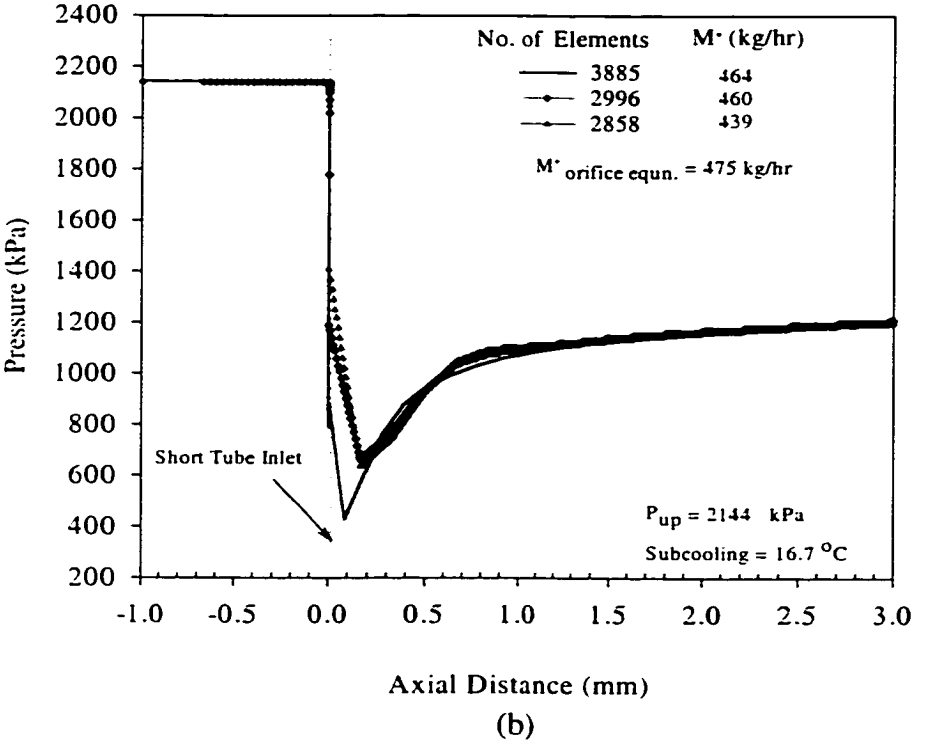

(b)

Figure 3.4 Pressure Profiles along a Flexible Short Tube Orifice, L= 14.5 mm, D_i = 2.06 mm, and D_e = 2.46 mm at Successive Mesh Refinement.
(a) The Whole Domain (b) The First 3 mm of the Tube Length.

Basic Equations

The problem under investigation involves a fluid-structure interaction. Hence, the basic equations must model this interaction.

The flow through flexible short tube orifices is expected to be turbulent. The very small inner diameter along with the refrigerant viscosity lead to higher Reynolds number values for a specific mass flow rate. Extra terms in the Reynolds Average Navier-Stokes equations, RANS, for turbulent flow are called the Reynolds stresses, $\overline{\rho u_i' u_j'}$. According to the Boussinesq assumption, (Tannehill et al 1997), the Reynolds stresses are given by:

$$\overline{\rho u_i' u_j'} = \mu_t \left(\frac{\partial u_i}{\partial x_j} + \frac{\partial u_j}{\partial x_i} \right) - \frac{2}{3} \delta_{ij} \left(\mu_t \frac{\partial u_k}{\partial x_k} + \rho k \right) \qquad (3.1)$$

where μ_t is the turbulent viscosity and k is the kinetic energy of turbulence, which is defined by $k = \overline{u_i' u_i'}/2$, Tannehill et al(1997). Therefore, the problem is getting the turbulence viscosity, μ_t. In terms of turbulence kinetic energy, k and turbulence energy dissipation, ε, the turbulent viscosity, μ_t, can be evaluated as $\mu_t = C_\mu (\rho k^2 / \varepsilon)$.

The k-ε model is a widely used model for internal flows, which provides an efficient method of calculating engineering flows, Nallasamy(1986). The Reynolds-

averaged momentum equations, the equation of continuity, and the k-ε turbulence model under the assumptions:

-2-D, steady axisymmetric flow

-Incompressible single-phase flow

-Isothermal expansion through the flexible tube

-Adiabatic flow due to low thermal conductivity of the tube material

-Potential effects are negligible

can be written in transport form, as used by ANSYS, as follows (Versteeg and Malalasekera 1995):

$$div\ (\rho\ \phi\ \mathbf{u}) = div\left(\Gamma_{\phi}\ \text{grad}\ \phi\right) + S_{\phi} \tag{3.2}$$

In the transport equation, the left hand side represents the convective or advection term and the first term in the right hand side is the diffusion term, (Γ_{ϕ} = diffusion coefficient). The second term in the right hand side is the source term. Table 3.2 shows the meaning of the variables, coefficients and source terms for the transport equation. The pressure equation is derived using the continuity equation. The continuity equation can be obtained from the transport equation (3.2) by setting $\phi = 1$, and $S_{\phi} = 0$. The table contains the 2-D momentum equations in addition to the turbulent kinetic energy, ENKE, and the turbulent energy dissipation, ENDS which both form the two equations, k-ε turbulence model.

Table 3.2 Variables Used in the Transport Equation (Equation 3.2).

ϕ	Γ_ϕ	S_ϕ
V_x	μ_e	$\rho g_x - \frac{\partial p}{\partial x}$
V_y	μ_e	$\rho g_y - \frac{\partial p}{\partial y}$
ENKE, k	μ_t/σ_k	$\mu_t \Phi - \rho\varepsilon$
ENDS, ε	μ_t/σ_ε	$C_1 \mu_t \varepsilon \Phi / k - C_2 \rho \varepsilon^2 / k$

While σ is the turbulent Prandtl number $\left(\frac{\mu_t C_p}{k_t}\right)$, :the other constants are given by:

C_μ	C_1	C_2	σ_k	σ_ε
0.09	1.44	1.92	1.0	1.3

The Φ term is called the viscous dissipation function, which is given by:

$$\Phi = \mu \left(\frac{\partial u_i}{\partial x_k} + \frac{\partial u_k}{\partial x_i} \right) \frac{\partial u_i}{\partial x_k} \tag{3.3}$$

Physically, it represents the rate at which mechanical energy is expended in the process of deformation of the fluid due to viscosity. The viscous dissipation function, Φ, includes both normal and shear stresses. The term, $\mu\Phi$, defines the work per volume done by stress in shearing and deforming fluid element and eventually it dissipates into heat.

The k-ε model is not valid immediately adjacent to the walls, in the viscous sublayer, because the damping effect associated with solid boundaries has not been included in the model, Tannehill et al (1997). Therefore, a wall turbulence model called the log-law of the wall is used. This law of the wall is employed in ANSYS. It is defined as:

$$U_{tan} \Big/ \sqrt{\frac{\tau_w}{\rho_w}} = \frac{1}{\kappa}\left[\mathrm{Ln}\,\frac{E\delta}{\nu}\sqrt{\frac{\tau_w}{\rho_w}}\right] \tag{3.4}$$

The values of κ (the von Karman constant), and E (a roughness parameter) are 0.4 and 9.0, respectively. Rodi(1993) mentioned that the law of the wall is sufficiently accurate in most situations. He commented by saying that the area near separation and stagnation points are an exception, but they are usually small and exert little overall influence on the flow.

The flexible orifice is made of an elastomeric material. Hence, it is important to understand the relationship between the elastic stresses and strains as a result of the applied external forces. An elastic strain is defined as a strain that disappears instantaneously once the forces that cause it are removed. The structure governing equations in matrix form, as used by ANSYS, and under the assumptions:

-Isotropic material, ($E_x = E_y = E_z = E$, and $\nu_{xy} = \nu_{yz} = \nu_{xz}$)

-Material is linear

-Axial and Radial Tube deformation with no rotation around the centerline

are simply written as:

$$\{\sigma\} = [D]\{\varepsilon^{el}\} \tag{3.5}$$

where: $\{\sigma\}$ = applied normal and shear stress vector =

$$[\sigma_x \quad \sigma_y \quad \sigma_z \quad \sigma_{xy} \quad \sigma_{yz} \quad \sigma_{xz}]^T$$

[D] = elasticity matrix, where its inverse in column normalized is written as:

$$[D]^{-1} = \begin{bmatrix} 1/E_x & -\nu_{xy}/Ey & -\nu_{xz}/E_z & 0 & 0 & 0 \\ -\nu_{yx}/E_x & 1/E_y & -\nu_{yz}/E_z & 0 & 0 & 0 \\ -\nu_{zx}/E_x & -\nu_{zy}/E_y & 1/E_z & 0 & 0 & 0 \\ 0 & 0 & 0 & 1/G_{xy} & 0 & 0 \\ 0 & 0 & 0 & 0 & 1/G_{yz} & 0 \\ 0 & 0 & 0 & 0 & 0 & 1/G_{xz} \end{bmatrix} \tag{3.6}$$

where: G is called the shear modulus and defined as:

$$G_{xy} = \frac{E_x E_y}{E_x + E_y + 2\nu_{xy} E_x} \tag{3.7}$$

For an isotropic material:

$$E_x = E_y = E_z = E$$

$$\nu_{xy} = \nu_{yz} = \nu_{xz} = \nu$$

$$G = \frac{E}{2(1+\nu)}$$

$$[D]^{-1} = \frac{1}{E}\begin{bmatrix} 1 & -\nu & -\nu & 0 & 0 & 0 \\ -\nu & 1 & -\nu & 0 & 0 & 0 \\ -\nu & -\nu & 1 & 0 & 0 & 0 \\ 0 & 0 & 0 & 2(1+\nu) & 0 & 0 \\ 0 & 0 & 0 & 0 & 2(1+\nu) & 0 \\ 0 & 0 & 0 & 0 & 0 & 2(1+\nu) \end{bmatrix} \tag{3.8}$$

$\{\varepsilon^{el}\}$ = elastic strain vector = total strain vector – thermal strain vector = $\{\varepsilon\} - \{\varepsilon^{th}\}$

$\{\varepsilon\}$ = total strain vector = $\left[\varepsilon_x \quad \varepsilon_y \quad \varepsilon_z \quad \varepsilon_{xy} \quad \varepsilon_{yz} \quad \varepsilon_{xz}\right]^T$

$\{\varepsilon^{th}\}$ = thermal strain vector = $(T-T_{ref})\left[\alpha_x \quad \alpha_y \quad \alpha_z \quad 0 \quad 0 \quad 0\right]^T$,

α is the thermal coefficient of expansion. The thermal strain vector is zero in this study. Inverting Equation 3.2 yields the strain vector as:

$$\{\varepsilon\} = \{\varepsilon^{th}\} + [D]^{-1}\{\sigma\} \tag{3.9}$$

FEM Model Developing

Fluid Flow Matrices

Derivation of the fluid flow matrices is based on applying the Galerkin's method of weighted residual on the scalar transport Equation (Equation 3.1). The form of the element equation is:

$$\left(\left[A_e^{\text{advection}}\right] + \left[A_e^{\text{diffusion}}\right]\right)\{\phi_e\} = \{S_e^{\phi}\} \tag{3.10}$$

In Galerkin's method, the weighting function of the element, W^e, is also the shape function. The derivation of element matrices for the terms in Equation 3.4 is introduced below.

The advection term is handled in ANSYS through a monotone streamline approach (Figure 3.5) based on the idea that pure advection transport is along characteristics lines. Assuming that no advection transport occurs across characteristics lines, but all transfer occurs along the streamline, the advection term ($div\ (\rho\ \varphi\ \mathbf{u})$) can be written as:

$div\ (\rho\ \varphi\ \mathbf{u}) = \dfrac{\partial \rho V_s \varphi}{\partial s}$. It is constant through out an element.

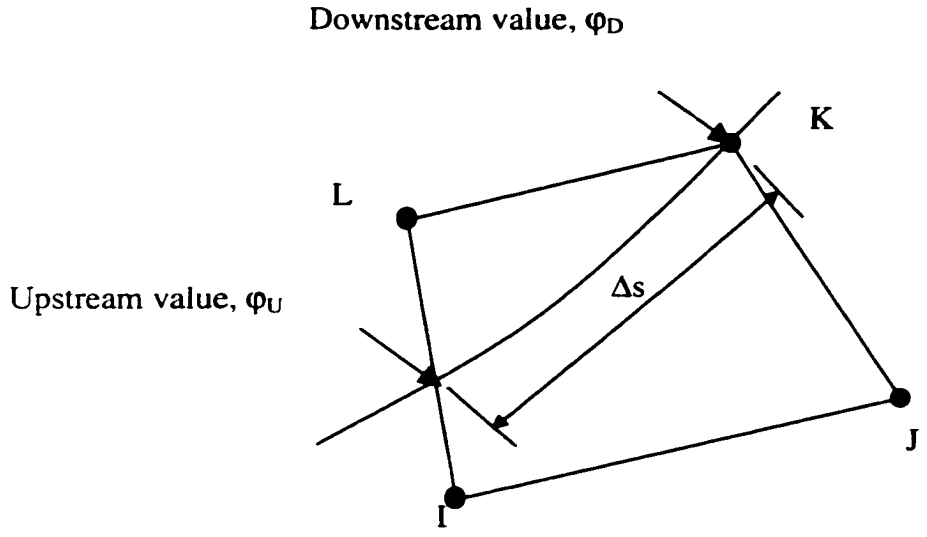

Figure 3.5 Streamline Upwind Approach, Swanson (1995).

Therefore, the advection term becomes:

$$\left[A_e^{\text{advection}}\right] = \frac{d(\rho V_s \phi)}{ds} \int W^e d(\text{vol}) \tag{3.11}$$

This formulation is made for every element. The derivative is simply calculated by using a finite difference as:

$$\frac{d(\rho \phi V_s)}{ds} = \frac{(\rho V_s \phi)_U - (\rho V_s \phi)_D}{\Delta s} \tag{3.12}$$

More details about the different first order and second order approaches for the advection term can be found in Swanson (1995).

The diffusion terms for 2-D come from an integration over the element area, Ω^e, after the multiplication by the weighting function and applying the integration by parts;

$$\left[A_e^{\text{diffusion}}\right] = \int_{\Omega^e} \left(\frac{\partial W^e}{\partial x} (\Gamma_\phi \frac{\partial W^e}{\partial x}) + \frac{\partial W^e}{\partial y} (\Gamma_\phi \frac{\partial W^e}{\partial y}) \right) \phi \, d(\Omega) \tag{3.13}$$

knowing that $\frac{\partial \phi}{\partial x} = W_x^e \phi$, and $W_x^e = \frac{\partial W^e}{\partial x}$. Similarly, the source term is written as:

$$S_\phi^e = \int_{\Omega^e} W^e S_\phi d(\Omega) \tag{3.14}$$

The segregated solution algorithm (Swanson 1995) in which each degree of freedom is solved in sequential fashion, is used to solve for the pressure equation. The preceding steps outlined the approach for every term except the pressure. In this approach, the momentum equation is used to generate an expression for the velocity in

terms of the pressure gradient. This is used in the continuity equation after being integrated by parts. The change in the product of density and velocity from iteration to the next is approximating by considering the change separately through a linearization process. In the x direction, for example, it gives:

$$(\rho V_x)^{i+1} = \rho^i V_x + \rho V_x^i - \rho^i V_x^i \tag{3.15}$$

where i represents the previous iteration and i+1 is the current iteration. Substituting Equation 3.15 in the continuity equation, applying Galerkin's method, and integrating by parts, yields three different groups. In the first group, the unknown velocity is integrated by parts; while in the second group, the unknown density is replaced by pressure. In the third group, the values from the previous iteration are used to evaluate the integral. The final form of the continuity is:

$$-\int_{\Omega^e}\left[\left(\rho^i V_x\right)\frac{\partial W^e}{\partial x}+\left(\rho^i V_y\right)\frac{\partial W^e}{\partial y}\right]d(\Omega)+\int_{\Omega^e}\left[\frac{W^e}{R}\frac{\partial}{\partial x}\left(V_x^i\frac{P}{T}\right)+\frac{W^e}{R}\frac{\partial}{\partial y}\left(V_y^i\frac{P}{T}\right)\right]d(\Omega)$$

$$-\int_{\Omega^e}W^e\left[\frac{\partial(\rho^i V_x^i)}{\partial x}+\frac{\partial(\rho^i V_y^i)}{\partial y}\right]d(\Omega)+\int_{\Gamma}W^e\left[\rho^i V_x+\rho^i V_y\right]d(\Gamma)=0 \tag{3.16}$$

The second and third terms in the above equation disappear for incompressible flow.

In Equation 3.16 there are unknown velocities, V_x and V_y. The momentum equations can be algebraically written in the form:

$$[A]\{V\}=\{S_o\}-\{\Delta\}^e \tag{3.17}$$

where [A] are the coefficient matrices which include the advection and diffusion contribution and $\{\Delta\}^e = \sum_{e=1}^{E} W^e \left\{\frac{\partial P}{\partial X_j}\right\}^e d(\Omega)$, j = 1,2,3. Nodal velocities in terms of the velocities of its neighbors, the source terms, and the pressure drop, after the summation of all the elements quantities, can be written as:

$$V_{x_j i} = \hat{V}_{x_j i} - \frac{1}{a_{ii}^{x_j}} \int_{\Omega^e} W^e \left(\frac{\partial P}{\partial x_j}\right) d(\Omega) \tag{3.18}$$

where the subscript i, denotes the nodal equation and varies from 1 to N, and j varies as 1,2,3. The hat velocities, $\hat{V}_{x_j i}$, contribute to the source term in the pressure equation, and it is defined as:

$$\hat{V}_{x_j i} = \frac{-\sum_{k}^{k\neq i} a_{ii}^{x_j} V_{x_j i} + S_{x_j}}{a_{ii}^{x_j}}, \quad j = 1,2,3 \tag{3.19}$$

Assuming that the pressure drop is constant over an element, then Equation 3.18 becomes:

$$V_{x_j i} = \hat{V}_{x_j i} - M_{x_j} \frac{\partial P}{\partial x_j} \tag{3.20}$$

where $M_{x_j} = \frac{1}{a_{ii}^{x_j}} \int_{\Omega^e} W^e \, d(\Omega)$. These expressions are used to replace the unknown velocities in the continuity equation to convert it into a pressure equation which has the following form on an element basis for an incompressible flow:

$$[P]^e \int_\Omega \left[\frac{\partial W^e}{\partial x} \rho^i M_x \frac{\partial W^e}{\partial x} + \frac{\partial W^e}{\partial y} \rho^i M_y \frac{\partial W^e}{\partial y} \right] d(area)^e = \int_\Omega \left[\frac{\partial W^e}{\partial x} \rho^i \hat{V}_x + \frac{\partial W^e}{\partial y} \rho^i \hat{V}_y \right] d(area)^e$$
$$- \int_\Gamma W^e \left[\rho^i \hat{V}_x \right] d(\Gamma) - \int_\Gamma W^e \left[\rho^i \hat{V}_y \right] d(\Gamma) \qquad (3.21)$$

After the solution of the pressure equation, the known pressures are used to evaluate the pressure drop which is added back into Equation 3.20 to update the velocity and to ensure that a velocity field conserves mass. The sequence for global iteration is shown in the following steps:

1. formulate and solve the two momentum equations approximately to calculate $\hat{V}_{x_j}$.
2. formulate pressure equation using $\hat{V}_{x_j}$.
3. solve pressure equation.
4. update velocities based on $\hat{V}_{x_j}$ and pressure.
5. solve turbulence equations, k-ε.
6. update effective properties based on turbulence solution.
7. check for convergence monitors.
8. end of one iteration.

Structural Matrices

Derivation of the structural matrices depends on the principle of virtual work, which states that a virtual change of the internal strain energy must be offset by an identical change in external work due to the applied load, Swanson (1995). Mathematically it is written as:

$$\delta U = \delta V \tag{3.22}$$

The strain energy, U, is divided into strain energy over the material volume, U_1, and strain energy over a surface area when a surface moves against a distributed resistance, U_2. The external work, V, includes inertial effects, V_1, applied pressure force, V_2, and nodal forces applied to the element, V_3.

The virtual strain energy is defined as:

$$\delta U_1 = \int_{vol^e} \{\delta\varepsilon\}^T \{\sigma\}\, d(vol) \tag{3.23}$$

and the strains may be related to the nodal displacement by: $\{\varepsilon\} = [B]\{u\}$; where [B] is the strain displacement matrix, based on the element shape functions. Similarly, the virtual strain energy over surface area is defined by:

$$\delta U_2 = \int_{area} \{\delta w_n\}^T \{\sigma\}\, d(area) \tag{3.24}$$

where $\{w_n\}$ is motion normal to the surface, and is related to the nodal displacement, $\{u\}$, by: $\{w_n\} = [N_n]\{u\}$; where $[N_u]$ is the matrix of shape functions for normal

motions at the surface. Further, the stress, $\{\sigma\}$, is defined as $\{\sigma\} = k\ \{w_n\}$, where k is the foundation stiffness in units of force per length per unit area.

The external work due to the applied pressure is defined by:

$$\delta V_2 = \int_{area} \{\delta w_n\}^T \{P\}\, d(area) \tag{3.25}$$

and the nodal forces applied to the element can be accounted for by:

$$\delta V_3 = \{\delta u\}^T \left\{F_e^{nd}\right\} \tag{3.26}$$

where $\left\{F_e^{nd}\right\}$ is the nodal forces applied to the element. Substituting Equations 3.5 through 3.8 and 3.23 to 3.26 into Equation 3.22 with neglecting the inertial effect and the acceleration vector $\delta^2 u/\delta t^2$ yields the structure FE model on one element:

$$\left([K_e] + \left[K^f{}_e\right]\right)\{u\} = \left\{F_e^{pr}\right\} + \left\{F_e^{nd}\right\} \tag{3.27}$$

where:

$$[K_e] = \int_{Vol} [B]^T [D][B]\, d(Vol) \qquad = \text{element stiffnes matrix}$$

$$\left[K_e^f\right] = k \int_{area} [N_n]^T [D][N_n]\, d(area) = \text{element foundation stiffnes matrix}$$

$$\left[F_e^{pr}\right] = \int_{area} [N_n]^T [P]\, d(area) \qquad = \text{element pressure vector}$$

Numerical Procedure

The sequential method for solving the model is as shown in the flow chart (Figure 3.6). The solution process occurs iteratively forward and backward between FLOTRAN and ANSYS until a convergence criteria is achieved. This criteria is defined as:

$$\frac{\sum_{i=1}^{n}\left|\phi_i^k - \phi_i^{k-1}\right|}{\sum_{i=1}^{n}\left|\phi_i^k\right|} \le \varepsilon, \tag{3.28}$$

where ϕ is an index for either the internal flow pressure distribution or the tube displacement, and ε is a predefined convergence criteria limit.

An external macro file using ANSYS Parametric Design Language, APDL, was written for each geometry model. The macro contains the different element types defined in ANSYS for the different regions. It has a fluid physics environment, a structural physics environment, and a fluid-structure loop which transfers the pressure loads from the fluid solver to the structure to solve for the nodal displacement. The interactive loop between the fluid and the structure executes the fluid-structure interaction part through coupled iterations. The macro starts by reading in the fluid physics environment which includes all boundary conditions and flow solver set up parameters. Then, the macro reads in the structure physics file, which contains all the boundary conditions, material properties (E, ν), and structure element types. The pressure results from the flow solver are transferred by the macro as internal loads to the

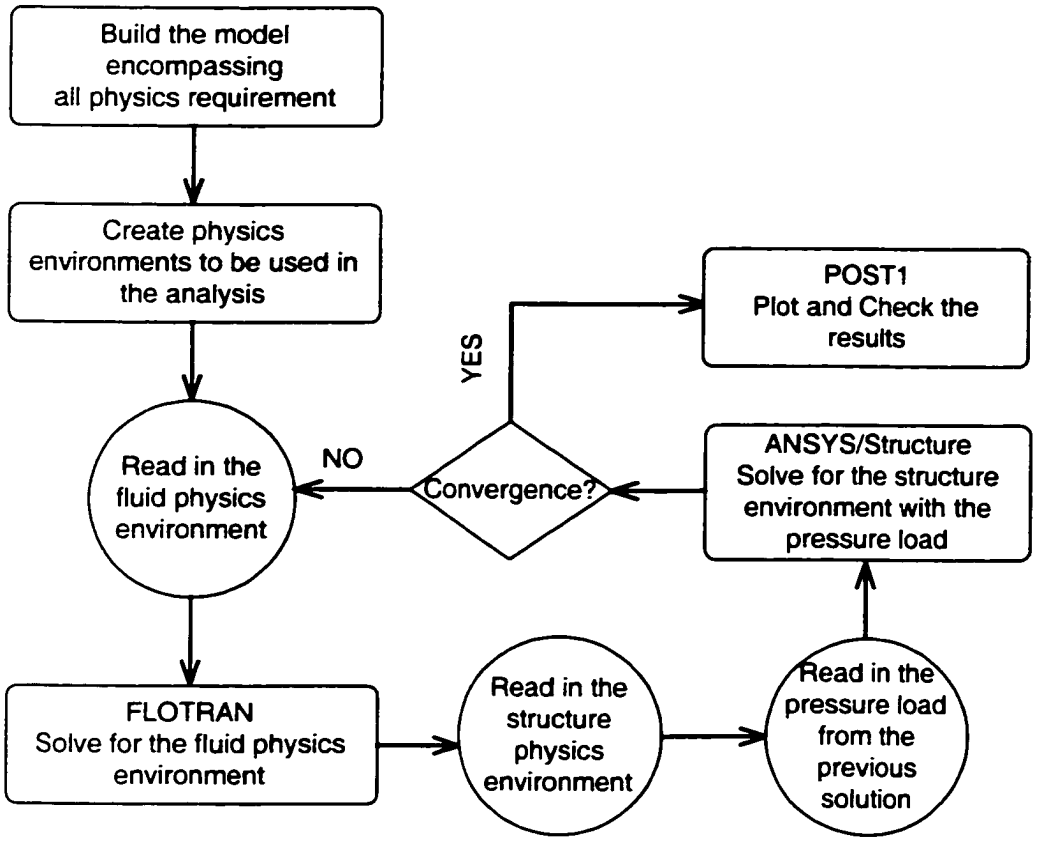

Figure 3.6 ANSYS Sequential Procedure for Coupled Problems Using Physics Environments.

structure, then the fluid-structure interaction loop solves for the tube nodal displacement and then finishes the solution process for one coupled iteration. The solution continues between fluid and structure till there is no significant change in the flow pressure distribution inside the tube for successive tube deformation.

CHAPTER IV

MODEL VALIDATION

It is difficult to assess the validity of the physical models embedded in a program as complex as a CFD code or the accuracy of its final results by any means other than comparison with experimental test work, (Versteeg and Malalasekera 1995). In the same reference, if experimental data are not available, validation could be assessed based on previous experience, previous analytical solution of similar but simple flow or with high quality data from closely related problems reported in the literature. Importantly, Versteeg and Malalasekera (1995), reported that the main ingredients for success in CFD are experience and a thorough understanding of the physics of the problem and the fundamentals of the numerical algorithm.

There were no previous comprehensive experimental or numerical studies on flow through flexible short tube orifices. Only one experimental study was published by Kim et al (1996) that mainly studied R-22 refrigerant flow rate through a flexible short tube orifice. On the other hand, adequate published experimental data for refrigerant flow through rigid short tubes are available in the literature, Mei (1982), Krakow and Lin (1988), Aaron and Domanski (1989), Kim(1993), and Kim and O'Neal (1994a,1994b,1995). Therefore, some of the published data of flow through rigid short tubes were used to assess the validity of the developed computational flow dynamic model.

Rigid Short Tube Model

The rigid short tube orifice along with the computational domain is shown in Figures 4.1 and 4.2, respectively. A short tube, typical in heat pump applications, with no chamfering at the inlet was chosen to be simulated. Quadrilateral rectangular elements were used in generating the mesh such that there was more flexibility in refining the mesh particularly near the tube walls to capture variables change in the boundary layer and in regions where a significant gradient of variables was expected. The boundary conditions were chosen to ensure a single-phase flow along the entire tube. These conditions were similar to some of the experimental data available (Kim 1993). Both upstream pressure and subcooling in addition to downstream pressure were given. Two rigid short tube configurations with the same diameter but different lengths were simulated.

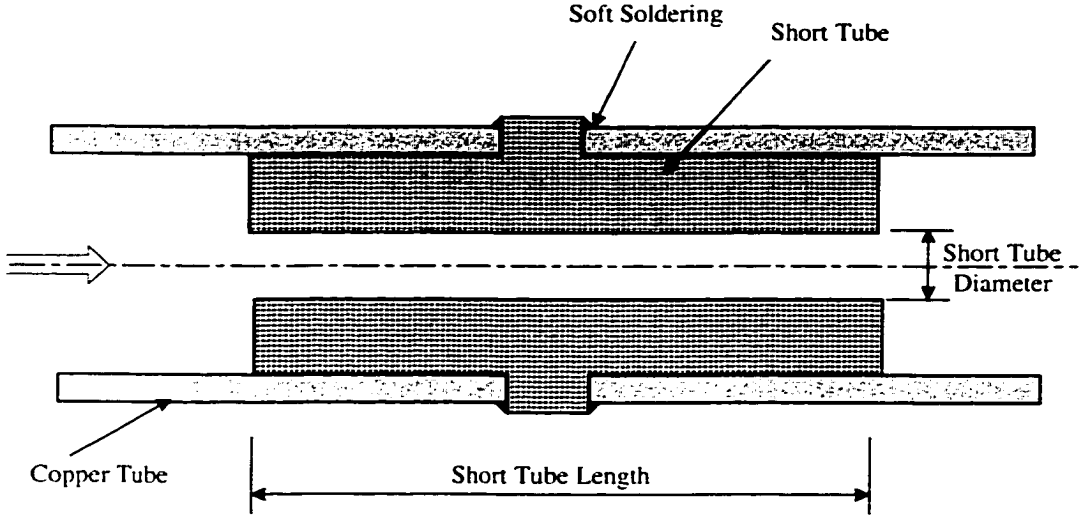

Figure 4.1 A Schematic of the Rigid Short-Tube Orifice.

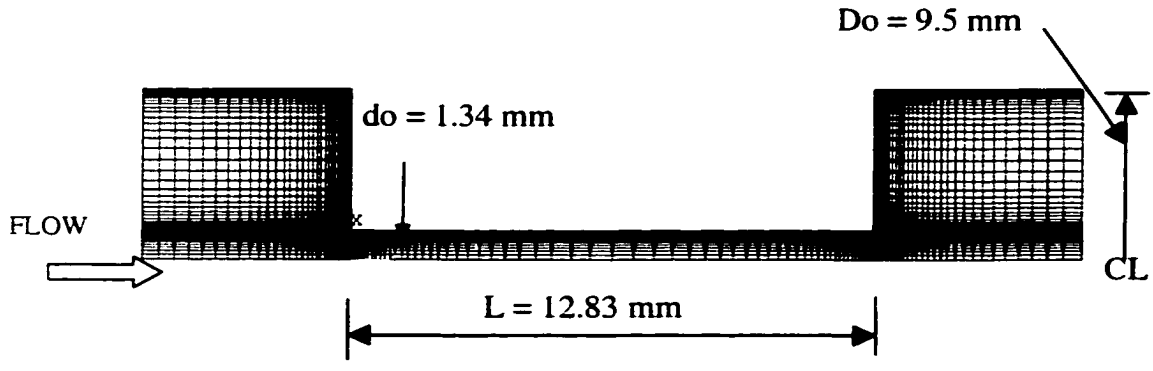

Figure 4.2 The Axisymmetric Computational Domain for a Rigid Short Tube Orifice.

Numerical Results Validation

The pressure profiles along a rigid short tube at two L/D ratios for single-phase flow of R-22 are shown in Figures 4.3 and 4.4. As shown by Figure 4.3, there was a close qualitative agreement between the numerical and experimental results by Aaron and Domanski (1990) and Kim (1993). The numerical model provided more details on the sharp pressure drop at the short tube inlet. Because of the restrictions in placing pressure transducers in the experiments, there were only five pressure readings in the short tube (Kim 1993). The numerical solution captured all the details without such restrictions, and as a result it yielded a smooth pressure recovery very close to the inlet. The maximum difference in pressure occurred downstream of the tube inlet and it was 11% and 20% for both downstream pressures studied 1361 kPa and 1234 kPa, respectively.

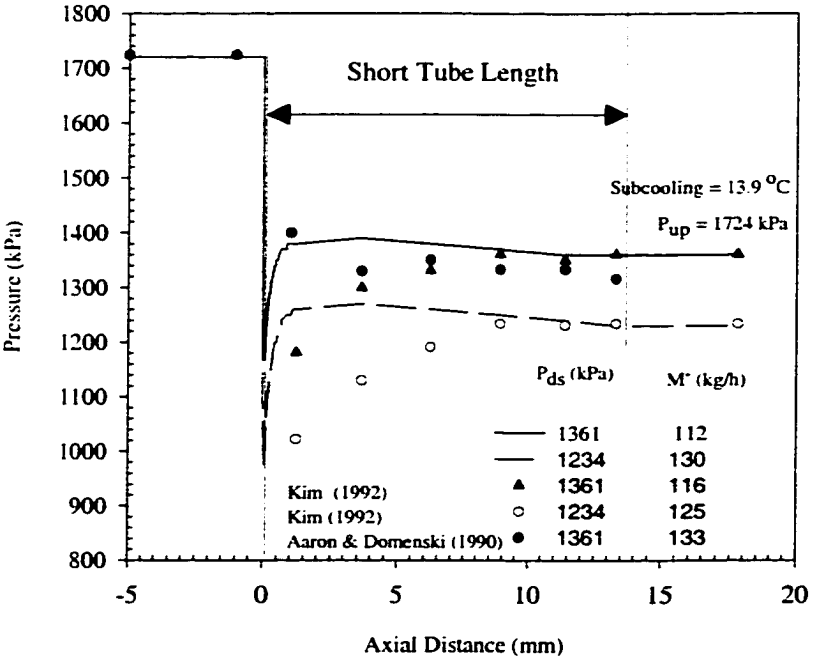

Figure 4.3 Axial Pressure Profiles Comparison for R-22 Single Phase Flow through a Short Tube Orifice, L=12.83 mm, D=1.34 mm.

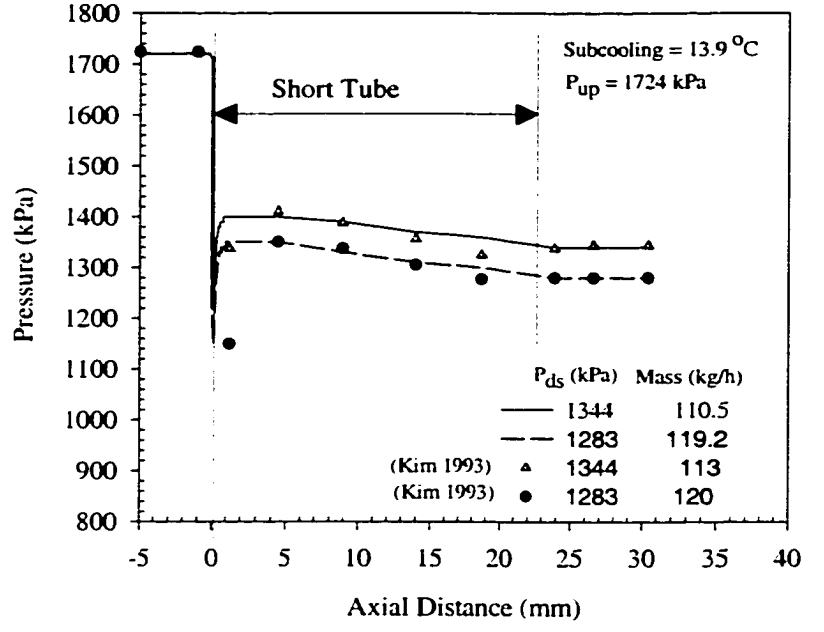

Figure 4.4 Axial Pressure Profiles Comparison for R-22 Single Phase Flow through a Rigid Short Tube Orifice, L=25.35 mm, D=1.34 mm.

For the second tube configuration $(L/D)_2$, Figure 4.4 displays the pressure variation along the tube compared to the experimental results. The figure shows very close qualitative as well as quantitative agreement between numerical and experimental results. The tube length in Figure 4.4 was twice that in Figure 4.3. The experimental data showed a flatter pressure profile for $(L/D)_2$ than for $(L/D)_1$ in Figure 4.3. There appeared to be a faster pressure recovery in Figure 4.4 after the vena contracta near the inlet. As the tube length increased, the mass flow rate decreased. The inlet loss is a function of the flow rate. Therefore, the inlet loss decreased, and consequently the pressure drop at the short tube inlet decreased.

The figures show qualitatively similar pressure trends. The maximum difference between numerical and experimental results was nearly 20%, which was mainly in the recovery zone after the vena contracta for the first tube geometry $(L/D)_1$.

Similar qualitative pressure profiles were obtained for R-134a single-phase flow through two tube configurations as shown in Figures 4.5 and 4.6. The numerical model captured the sharp drop in pressure at the tube inlet. However; the experimental data showed a much longer pressure recovery region compared to that predicted by the numerical model. The numerical model overpredicted the pressure downstream of the short tube inlet for both configurations. An overprediction of 25-30% was shown in the figure very close to the tube inlet (1.3 mm axial distance) for both downstream pressures. Along the tube axis, this overprediction decreased to 4% close to the tube exit.

For the same tube configuration, Figure 4.6 shows a distinctive difference in predicting pressure profiles of R-134a compared to that of R-22 (Figure 4.4). This

difference was in the recovery region. Kim (1993) reported that the flow dependency on downstream pressure for R-134a was slightly lower than that of R-22. However, similar to R-22, the sharp pressure drop at the tube inlet decreased as L/D increased. Increasing the tube length might allow the pressure waves inside the tube to relax and therefore the pressure drop decreased. An overpredicition of 28 to 30% was shown from Figure 4.6 very close to the contraction after the vena contracta, (1.5 mm axial distance). The overprediction in Figure 4.6, compared to Figure 4.4, could be due to a significant round-off error as a result of the excessive mesh refinement at the tube inlet. Since R-134a operated at almost 30% lower pressure than R-22, the effect of the round-off error might be significant. The mass flow rates corresponded to the downstream pressures are listed in Table 4.1. The maximum difference between the estimated and the measured values was almost ±5%.

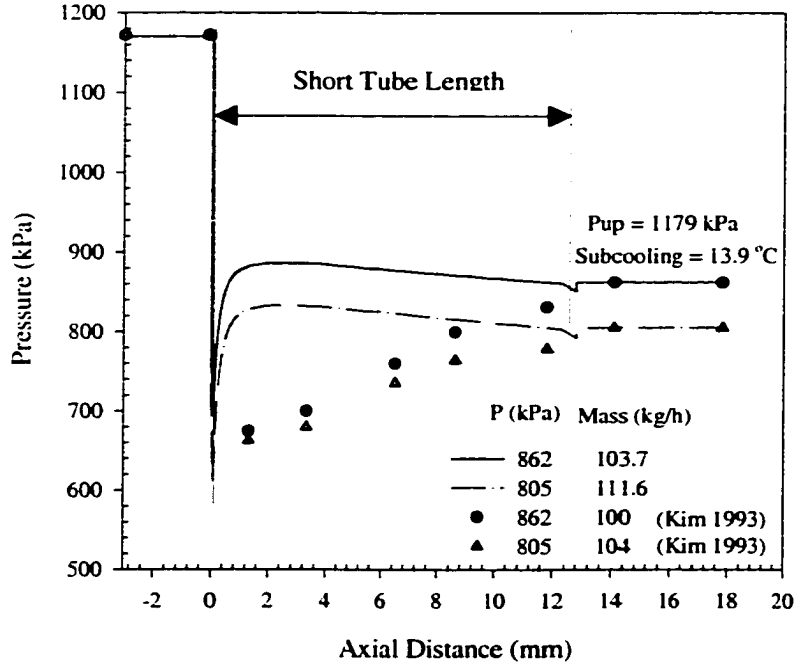

Figure 4.5 Axial Pressure Profiles Comparison for R-134a Single Phase Flow through a Rigid Short Tube Orifice. L = 12.83 mm, D=1.34 mm.

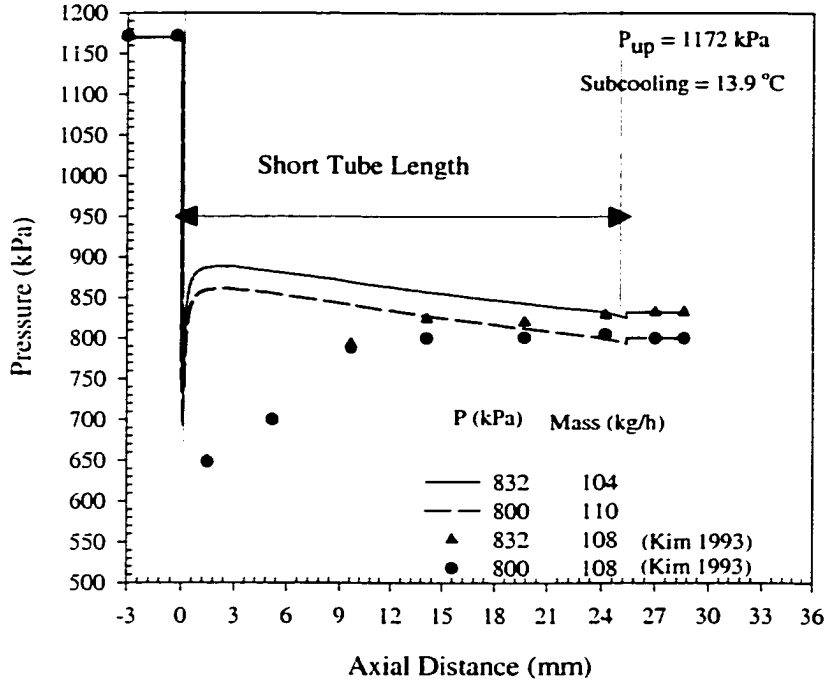

Figure 4.6 Axial Pressure Profiles Comparison for R-134a Single Phase Flow through a Rigid Short Tube Orifice. L=25.35 mm. D =1.34 mm.

Table 4.1 Numerical versus Experimental Mass Flow Rate Values.

	Geometry	$(L/D)_1 = 9.65$		$(L/D)_2 = 18.9$	
R-22	P_{down} (kPa)	1361	1234	1344	1283
	$M_{exp.}$ (kg/h)	116	125	113	120
	$M_{num.}$(kg/h)	112	130	111	119
R-134a	Geometry	$(L/D)_1 = 9.65$		$(L/D)_2 = 18.9$	
	P_{down} (kPa)	862	805	832	800
	$M_{exp.}$ (kg/h)	100	104	108	108
	$M_{num.}$(kg/h)	103	112	104	110

The dependence of the mass flow rate on downstream pressure is shown in Figures 4.7 and 4.8 for both R-22 and R-134a, respectively. Both figures show a close agreement between the estimated mass flow rate with the measured values. For R-22, the flow rate estimated by the numerical model was ±4% of the experimental values; while, it was within ±8% for R-134a. Both experimental and numerical values of mass flow showed the same trends as the downstream pressure changed. All the values of the downstream were either at or above the saturation pressure corresponding to the inlet temperature to ensure single-phase flow through the short tube.

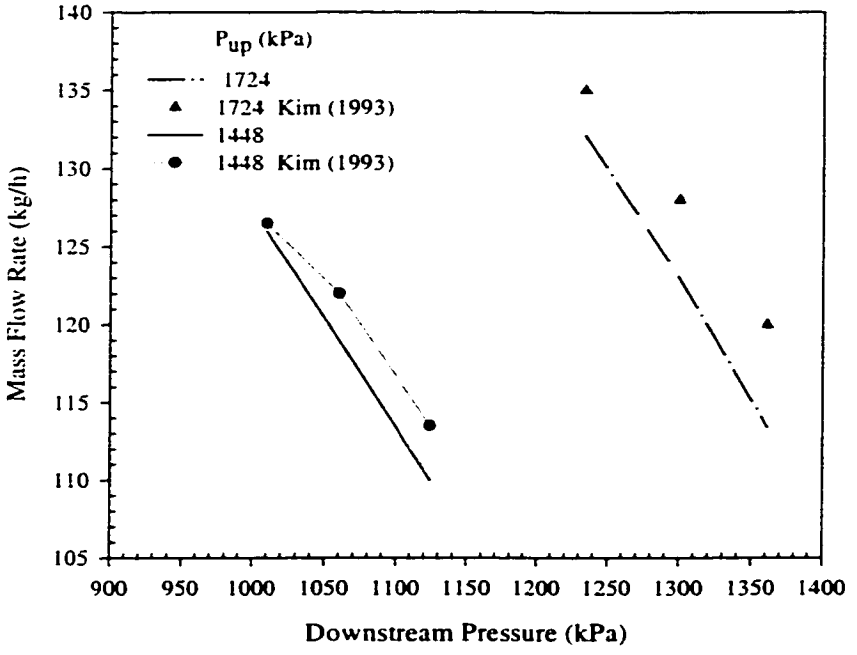

Figure 4.7 Mass Flow Rate Variation versus Downstream Pressure for R-22 Single Phase Flow through a Rigid Short Tube, L =12.83 mm, D =1.34 mm.

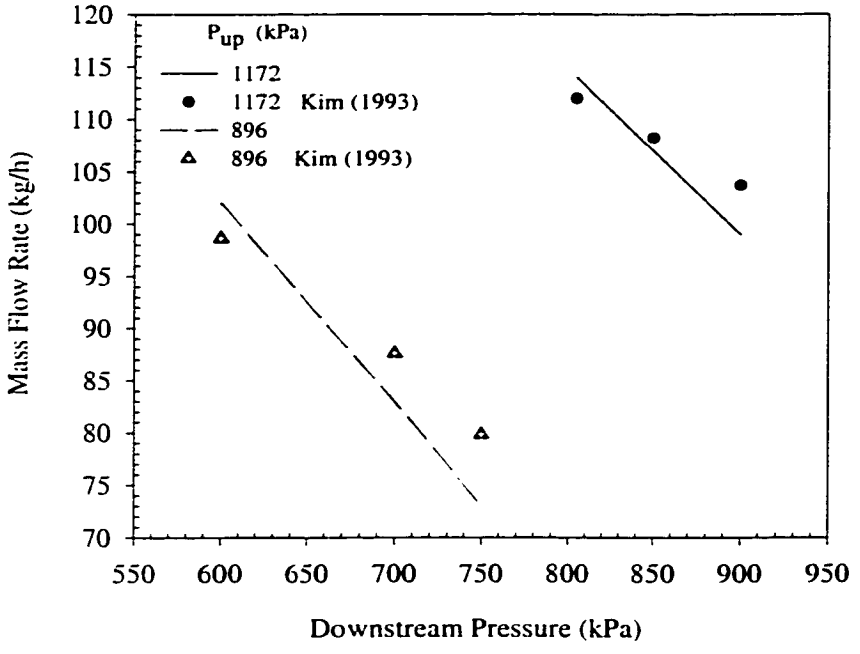

Figure 4.8 Mass Flow Rate versus Downstream Pressure for R-134a Single Phase Flow through a Rigid Short Tube Orifice, L = 12.83 mm, D =1.34 mm.

The estimated and measured effect of short tube geometry on mass flow rate is given in Figure 4.9 for both R-22 and R-134a. The figure shows the agreement between the estimated and the measured values. The trend was qualitatively similar for R-134a as well. Generally, the flow dependency upon tube length decreased as the tube diameter decreased (Kim 1993). This trend was consistent with that is shown in Figure 4.9 where there was no significant change in mass flow rate for L/D between 10 and 19, while there was a large change when L/D decreased below 10. This may indicate that the tube diameter is a more critical parameter than the tube length in affecting the mass flow rate. The mass flow rate was extremely sensitive to changes in short tube diameter. For the same subcooling, the mass flow rate was approximately proportional to D^2, which agreed with experiments by Kim(1993). The model predicted values were almost 40% higher for L/D less than 9, while it decreased to almost 4% for L/D ratios more than 9.

A final validation of the numerical model was performed by comparing the predicted values from the model with the available published data for R-22 flow through a flexible short tube. The available data are from a study by Kim et al (1996) that dealt with the effect of operating conditions on mass flow of R-22 carrying a 1.2 % of oil through flexible short tube orifices. The study was done for two moduli of elasticity. Figure 4.10 shows the comparison of the predicted results to the experimental data.

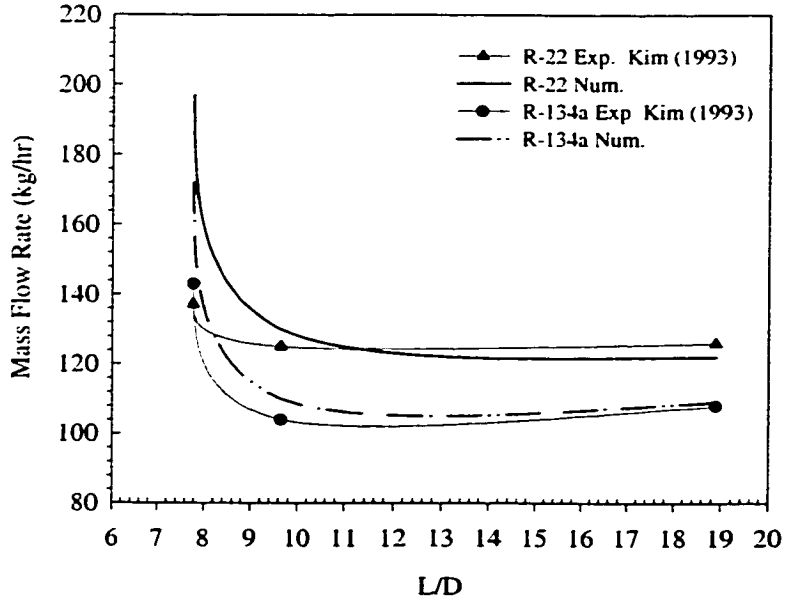

Figure 4.9 Numerical to Experimental Mass Flow Rate Variation versus L/D Ratio of a Rigid Short Tube for Refrigerant Single Phase Flow.

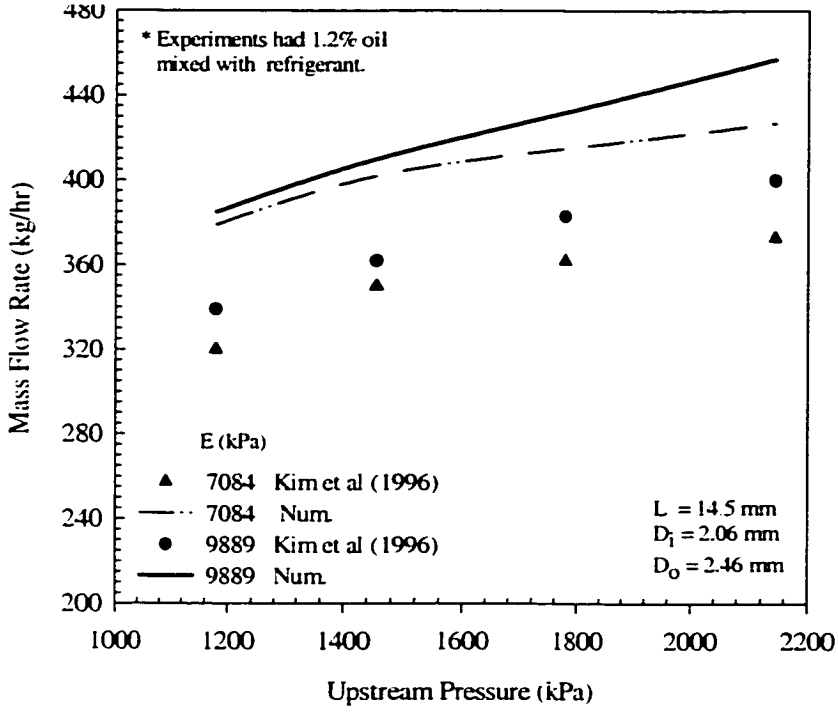

Figure 4.10 Mass Flow Rate Comparison between Numerical and Experimental Results for Single Phase Flow of R-22 through a Flexible Short Tube Orifice.

Figure 4.10 illustrates an overall qualitatively similar trends for both experiment and computation. As the upstream pressure increased, the mass flow rate increased for a single phase flow as shown in this figure. Furthermore, it is shown in Figure 4.10 the close agreement between numerical and experimental results as the slope of the trend changed for the lower modulus tube at upstream pressure more than 1400 kPa. Quantitatively, the numerical model overpredicted the mass flow rate. The numerical results were 14% higher than the experimental data which had a 1.2% of oil mixed with the refrigerant.

CHAPTER V

RESULTS AND DISCUSSION FOR R-22

Flow through flexible short tube orifices with L/D ratios ranging from 5.5 to 11.5 were modeled using ANSYS under various operating conditions. Three different tube configurations with material's modului of elasticity, 5513 kPa (800 psi), 7084 kPa (1028 psi), and 9889 kPa (1435 psi) were simulated. The numerical results, which include pressure profiles, tube material displacement, and tube radius variations of R-22 single phase flow are presented in this chapter. The effect of upstream, L/D ratio, and modulus of elasticity on mass flow rate is presented. The numerical results for R-22 were used as a base line to check the validation of the numerical solution based on comparing the predicted mass flow rates with the available published experimental results by Kim et al (1996).

Effect of Modulus of Elasticity on Tube Deformation and Pressure Profiles

Having a better understanding of flow behavior in flexible short tubes and the resultant tube deformation under various operating conditions can help the designer in selecting the right material and diameter to optimize heat pump performance. Figures 5.1a and 5.1b show the estimated velocity distribution inside a flexible short tube. The region of maximum velocity at the tube inlet due to the sudden contraction followed by another velocity increase due to the tube deformation is shown in Figure 5.1a. Various

Figure 5.1a Velocity Contours of R-22 Single Phase Flow through a Flexible Short Tube Orifice (L = 14.5 mm, D_i = 2.06 mm, D_o = 2.46 mm) at P_{up} = 2144 kPa and for E = 7084 kPa.

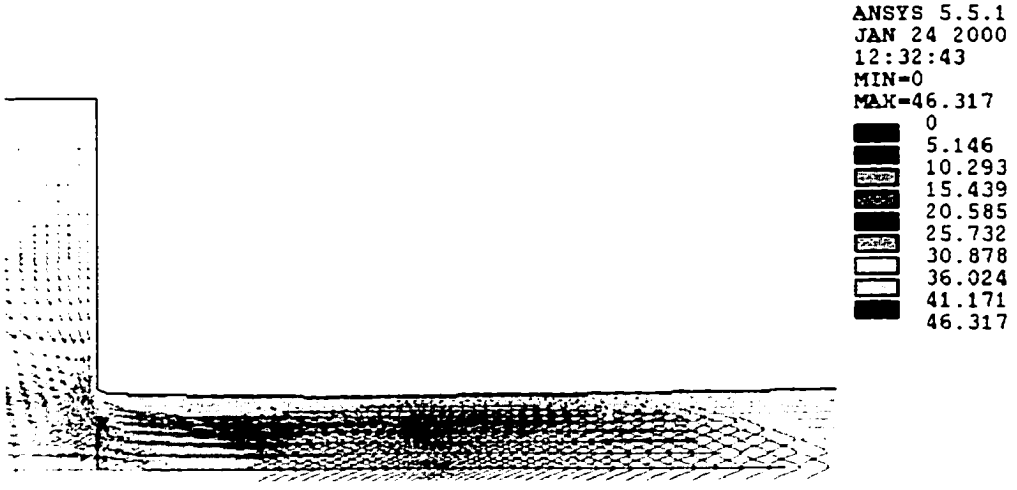

Figure 5.1b An Enlarged Section for the First 7mm of the Tube of Velocity Vectors of R-22 Single Phase Flow through a Flexible Short Tube Orifice (L = 14.5 mm, D_i = 2.06 mm, D_o = 2.46 mm) at P_{up} = 2144 kPa and for E = 7084 kPa.

regions where kinetic energy was gradually decreasing along the divergent section of the short tube till the tube exit edge are also shown in this figure. As the flow approached the tube inlet, the velocity exhibited inward radial turning due to the sudden change in the area and the failure of the flow to follow the sharp turn at the tube inlet (Figure 5.1b). Although the inlet edge was sharp, this figure showed a chamfered-like rounded inlet after deformation. The flow downstream of the short tube inlet was accelerated due to the contraction of the tube area as a result of the net pressure force exerted on the tube surface that led to a radial reduction in the tube cross sectional area. With the flow acceleration at the tube inlet, the flow separated from the tip of the tube inlet edge and then reattached itself to the tube wall downstream.

The corresponding pressure contours along a portion of the deformed tube are shown in Figure 5.2. This figure shows the different regions of minimum and maximum pressure. A low pressure region is illustrated very close to the inlet which corresponds to the sharp pressure drop at the tube inlet. This low pressure is an indication of the vena-contracta near the tube inlet.

Figure 5.3 presents an enlarged qualitative picture for the short tube deformation as a consequence of the interaction with refrigerant flow. It shows the cross section area variation along the axis of the tube and the minimum area at which the flow acceleration and maximum pressure drop took place.

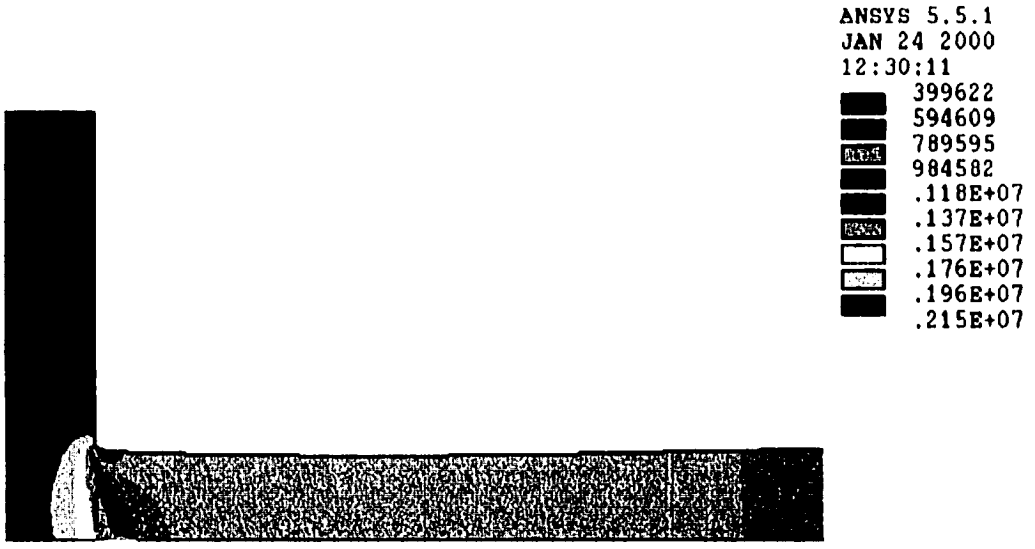

Figure 5.2 An Enlarged Section of Pressure Contours of R-22 Single Phase Flow through a Flexible Short Tube Orifice (L = 14.5 mm, D_i = 2.06 mm, D_o = 2.46 mm) at P_{up} = 2144 kPa and for E = 7084 kPa.

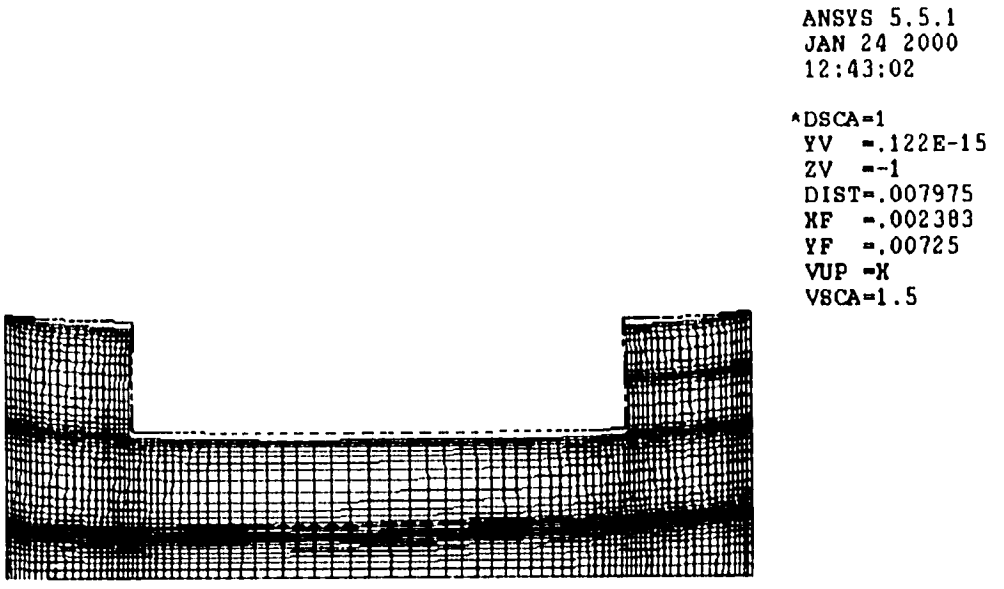

Figure 5.3 True Scale Deformation of a Flexible Short Tube Orifice (L = 14.5 mm D_i = 2.06 mm, D_o = 2.46 mm) as a Result of R-22 Single Phase Flow at P_{up} = 2144 kPa and for E = 7084 kPa.

First Tube Configuration $(L/D)_1$

Pressure profiles along a flexible short tube at two different moduli of elasticity are shown in Figure 5.4. The figure illustrates the successive coupled (global) iterations until the pressure profile converged after the fourth iteration. A coupled iteration means solving for the non-linear fluid governing equations, then transferring the resultant internal pressure distribution as an exerted load on the tube internal area to solve for the structure deformation. The profile corresponding to the first iteration in this figure represents the initial internal pressure distribution along the non-deformed tube. The figure displays a large dip in the pressure profiles as refrigerant flows downstream of the tube inlet for the more flexible material compared to the less flexible material. This indicates that the more flexible tube (lower modulus of elasticity) contracted to a minimum area at which this drop of pressure occurred more than the less flexible tube (higher modulus of elasticity). Quantitatively, the maximum pressure drop, at almost 4 mm from the short tube inlet estimated as $(P_{up} - P_{dip})$, increased by nearly 21% when the modulus of elasticity decreased (flexibility of the tube increased) by almost 28%. This indicates that the flow internal pressure variation for the less modulus tube was lower due to the more tube contraction compared to the higher modulus tube at the same upstream pressure.

To study the effect of modulus of elasticity and upstream pressure on flow pressure variation, the estimated pressure profiles for three moduli of elasticity as well

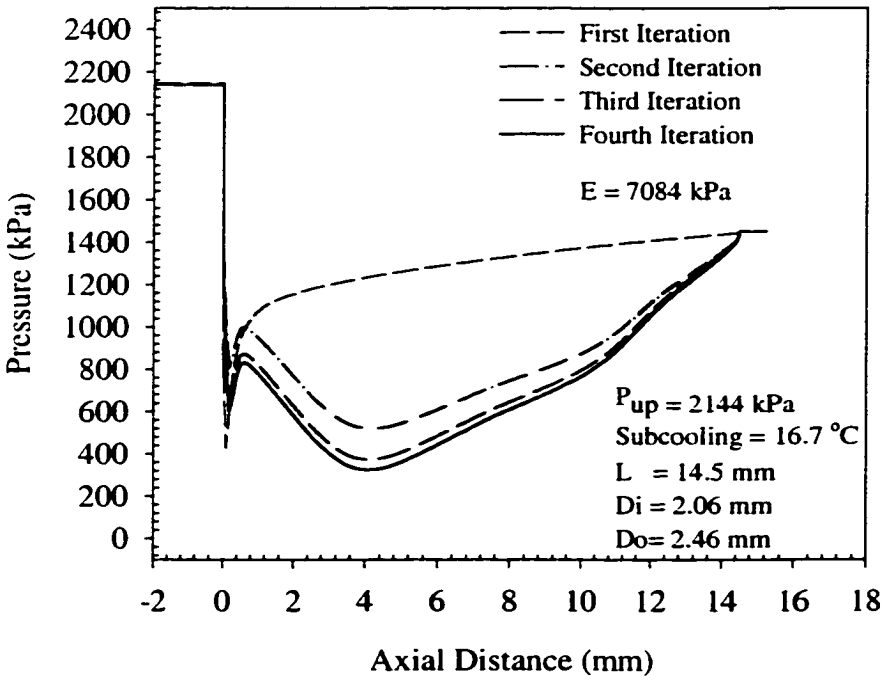

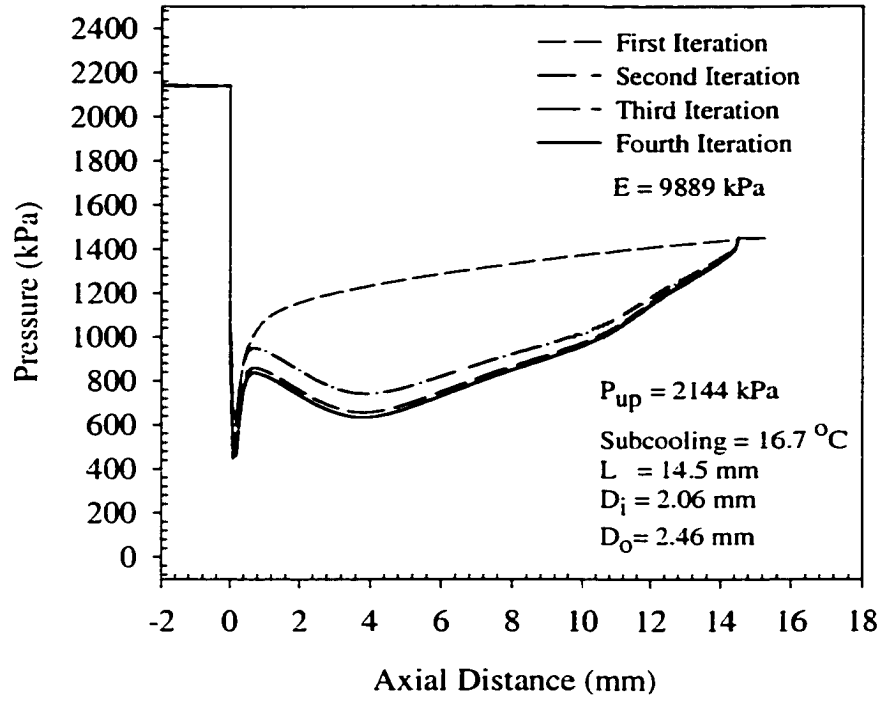

Figure 5.4 Pressure Profile Change for R-22 Single Phase Flow through a Flexible Short Tube Orifice $(L/D)_t$ at Successive Global Iterations for Two Moduli of Elasticity.

as for the undeformed tube at two upstream pressures are shown in Figure 5.5. The lowest modulus tube, (5513 kPa), yielded the lowest pressure profile for both upstream pressures, and consequently the maximum pressure drop along the tube. The figure also indicates two distinctive pressure drop regions. A sharp pressure drop occurred at the tube inlet due to the rapid acceleration of the fluid as a result of the sudden change in the cross sectional area and the inlet losses. This sharp drop at the inlet is an indication of the vena contracta effect. A close investigation of the sharp pressure drop at the tube inlet revealed that the less flexible tube, 9889 kPa, produced a higher pressure drop at the inlet than the more flexible one. This can be attributed to the smaller deformation at the tube inlet for the less flexible material compared to the more flexible material. As the modulus of elasticity decreases, the tube gets more flexible and hence the inlet edge buckles more (large chamfering angle) upon tube deformation. Therefore, there was a smaller pressure drop at the inlet for the more flexible short tube. This phenomenon was experimentally noticed by Kim et al (1996).

The tube radial deformation as well as the tube radius variation along the tube axis are shown by Figures 5.6 and 5.7, respectively. In Figure 5.5, the higher tube modulus had a 10% higher pressure drop at the inlet than the lower tube modulus at an upstream pressure of 1179 kPa. However, the more flexible tube had a 28% higher-pressure drop at approximately 4 mm from the tube inlet because of the large cross sectional area contraction compared to the stiff tube. Moreover, the maximum

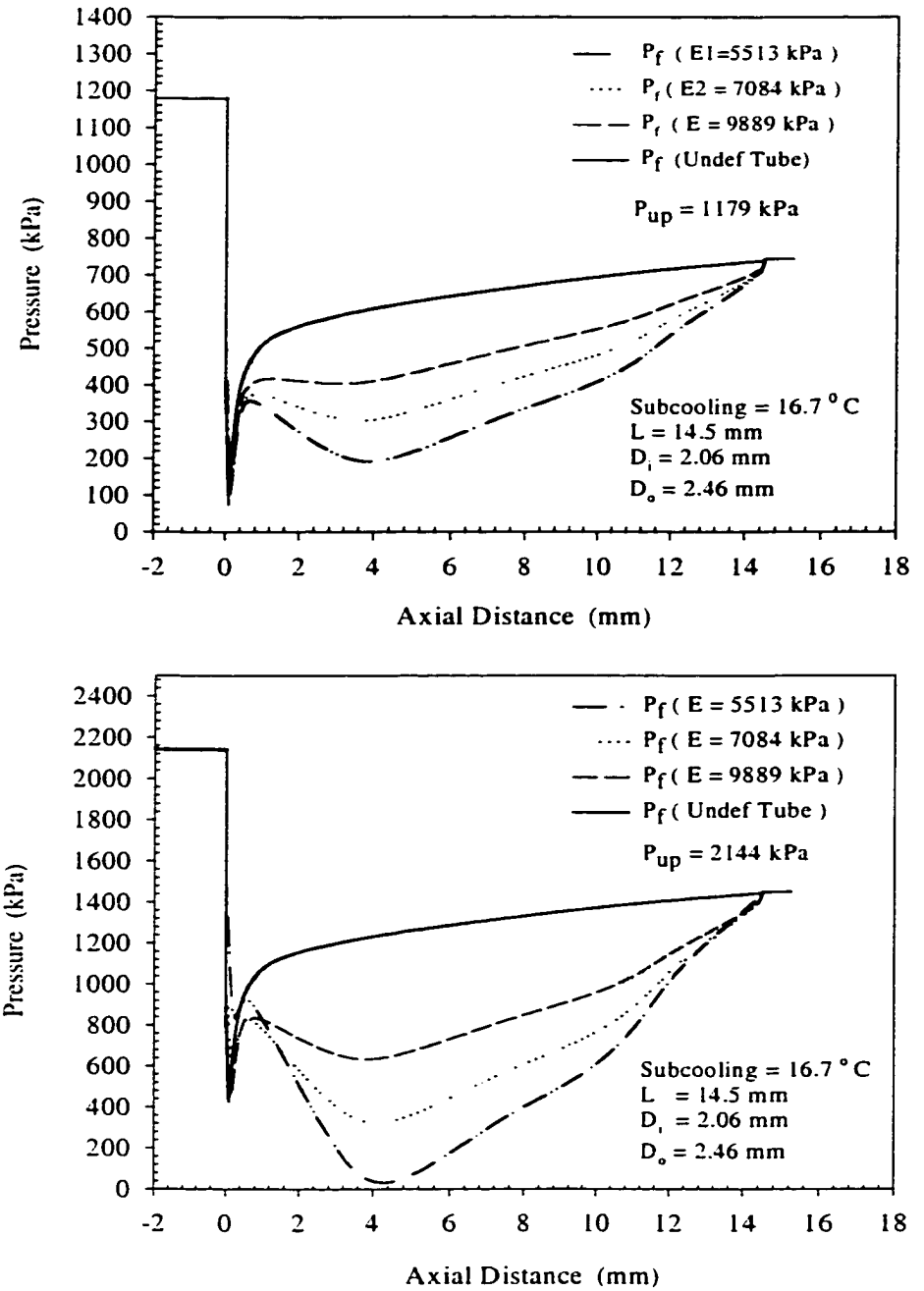

Figure 5.5 Pressure Profiles Comparison for R-22 Single Phase Flow through a Flexible Short Tube Orifice $(L/D)_i$ for Three Moduli of Elasticity and Two Upstream Pressures.

pressure drop at almost 4 mm from the short tube inlet increased by almost 72% compared to the pressure drop in the non deformed tube. On the other hand, a 28% increase in the pressure drop at the inlet was found for the higher modulus tube over the lower modulus tube as the upstream pressure was increased to 2144 kPa. Nevertheless, the lower modulus tube experienced a 45% larger pressure drop than the higher modulus tube at almost 4 mm from the tube inlet due to the large deformation corresponding to this axial distance. Figure 5.5 shows a smooth pressure variation profile without any dip for the non deformed tube. A pressure recovery downstream of the inlet as a result of the divergent shape of the tube internal area before deformation is shown by this figure.

Figures 5.6 and 5.7 assist explaining the refrigerant pressure variation along the tube (Figure 5.5). Figure 5.6 shows that the more flexible material (lower modulus of elasticity) had a larger deformation and consequently a smaller free cross sectional area. For the first tube configuration, $(L/D)_1$, Figure 5.6 illustrates that the tube radial deformation increased by 80% when the tube modulus of elasticity decreased (flexibility increased) by 45%. For the same tube configuration with the lowest modulus material, the radial deformation increased by almost 60% as the upstream pressure increased by almost 82%, as shown by Figure 5.6. Because of the constraints used at the tube ends (neglecting axial deformation compared to radial deformation) for numerical stability reasons, the radial displacement was zero at both ends of the tube.

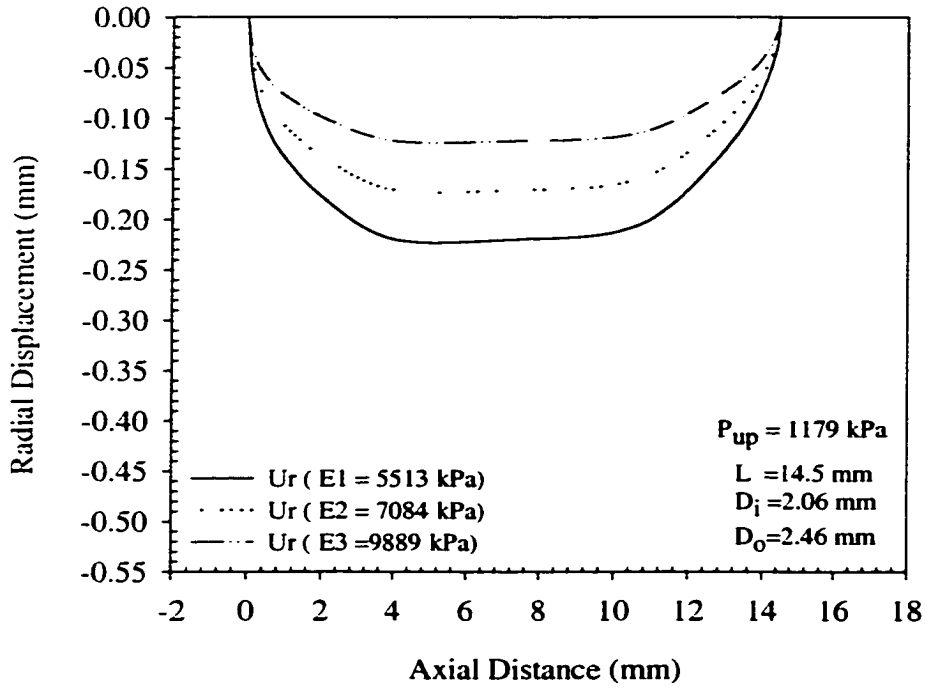

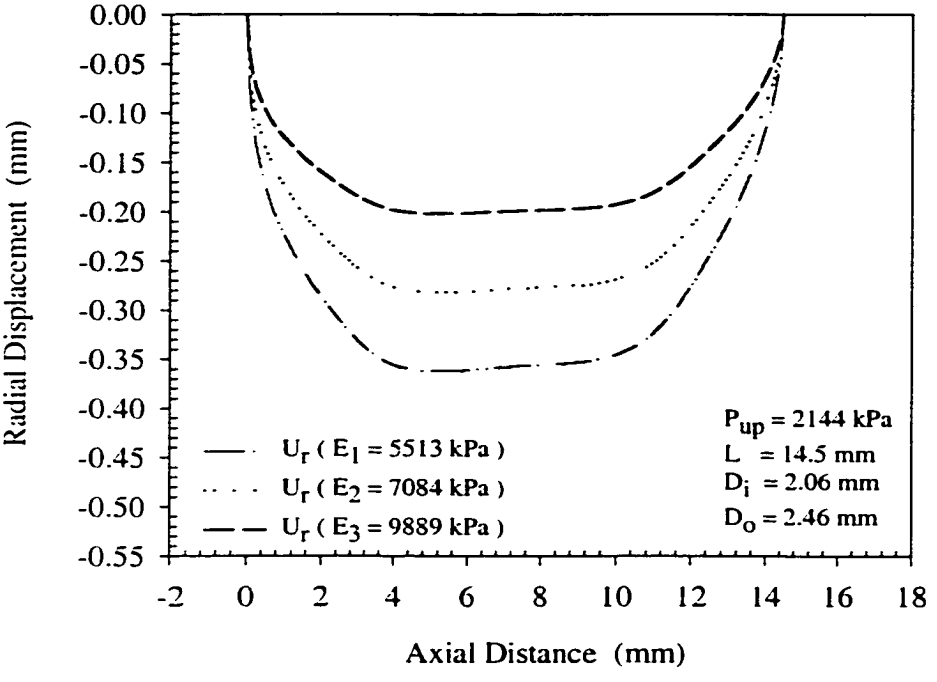

Figure 5.6 Radial Displacement Comparison along a Flexible Short Tube Orifice $(L/D)_i$ as a result of R-22 Single Phase Flow at Three Moduli of Elasticity and Two Upstream Pressures.

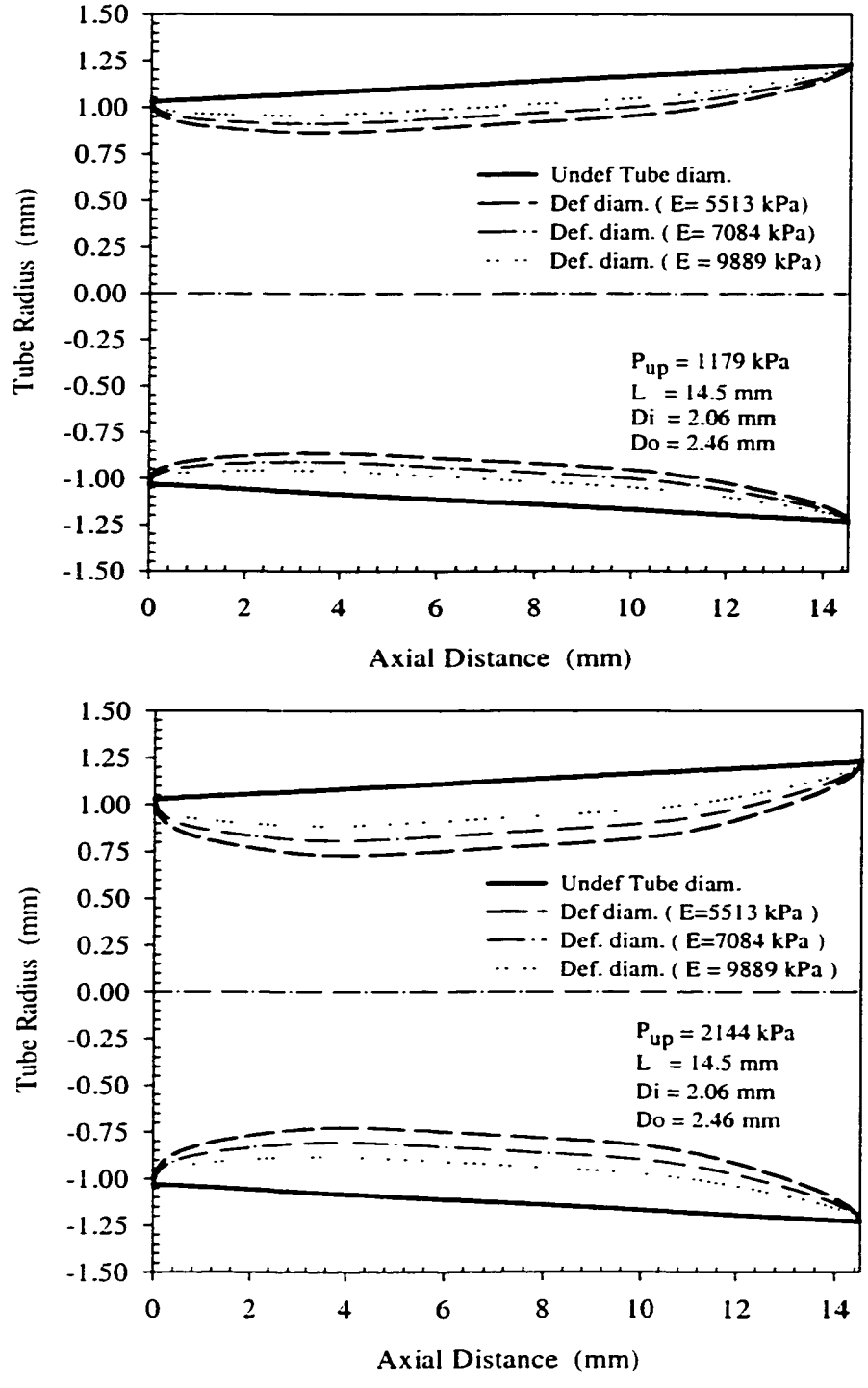

Figure 5.7 Radius Variation along the Axis of a Short Tube Orifice $(L/D)_1$ as a Result of R-22 Single Phase Flow for Three Moduli of Elasticity and Two Upstream Pressures.

An Alternative approach to presenting the displacement data is to plot how the radius of the tube axially changes (Figure 5.7). A close investigation of the shape in Figure 5.7 shows that the deformed shape resembles a converging-diverging nozzle. The tube had a chamfered-like rounded inlet and outlet as a result of the deformation caused by the pressure difference between external and internal pressures. A visible increase in the chamfering-like inlet angle was observed as the modulus of elasticity decreased (flexibility increased). Figure 5.7 shows that there was a measurable change in the new geometry of the short tube for the three mouduli of elasticity at the two pressures studied. The minimum tube cross section area occurred at an axial distance approximately 3 to 4.5 mm from the short tube inlet. This location corresponded to the pressure dip shown in Figure 5.5. The deformed shape helps explaining the pressure profiles along the tube. As the flow approached the tube inlet, a sharp pressure drop occurred due to the sudden reduction in area. This drop was higher for the stiff tube.

As the tube modulus decreased, the sharp pressure drop decreased due to the chamfered-like inlet after deformation. Downstream of the inlet, a pressure recovery was followed by another pressure drop corresponding to the minimum cross sectional area which resembled a nozzle throat at an axial distance ranges between 3 to 4 mm. The maximum reduction in tube diameter at this location for the lowest modulus of elasticity was 20% and 32%, respectively, when the upstream pressure increased from 1179 kPa to 2144 kPa. As flow passed through the minimum deformed area, its kinetic energy increased and accordingly its pressure decreased. Downstream of the throat,

another pressure recovery was noticed as the refrigerant flowed through the divergent section of the short tube. A verification for the lower pressure drop very close to the tube inlet (1 mm from the inlet) was performed using Bernoulli's equation along with taking into consideration the sudden contraction loss. The calculation yielded 2 to 7% higher pressure values than the numerically estimated values for the two studied upstream pressures.

Second Tube Configuration $(L/D)_2$

The pressure variations for the second tube configuration, $(L/D)_2$, for different material properties and upstream pressures are shown in Figure 5.8. The figure indicates the effect of increasing the tube length on pressure profiles. For this tube configuration, there were less differences between the pressure profiles as the tube flexibility increased compared to the equivalent profiles for the first tube configuration, $(L/D)_1$ (Figure 5.5). In Figure 5.8, the smooth pressure profile for the non deformed tube is shown. The estimated pressure drop associated with the vena contracta very close to the tube inlet was smaller for the longer tube. As the pressure at the inlet of the tube for $(L/D)_1$ reached almost 600 kPa below the saturation pressure, it was approximately 500 kPa below the saturation pressure for $(L/D)_2$. This may indicate that the longer tube buckled more, and then had more inlet chamfering than that for the shorter tube length. This effect clearly appeared when the upstream pressure increased (Figure 5.8). Quantitatively, for the 1179 kPa upstream pressure, a 15% pressure drop at the tube inlet was found for the stiff tube over the lower modulus tube. However, as the tube

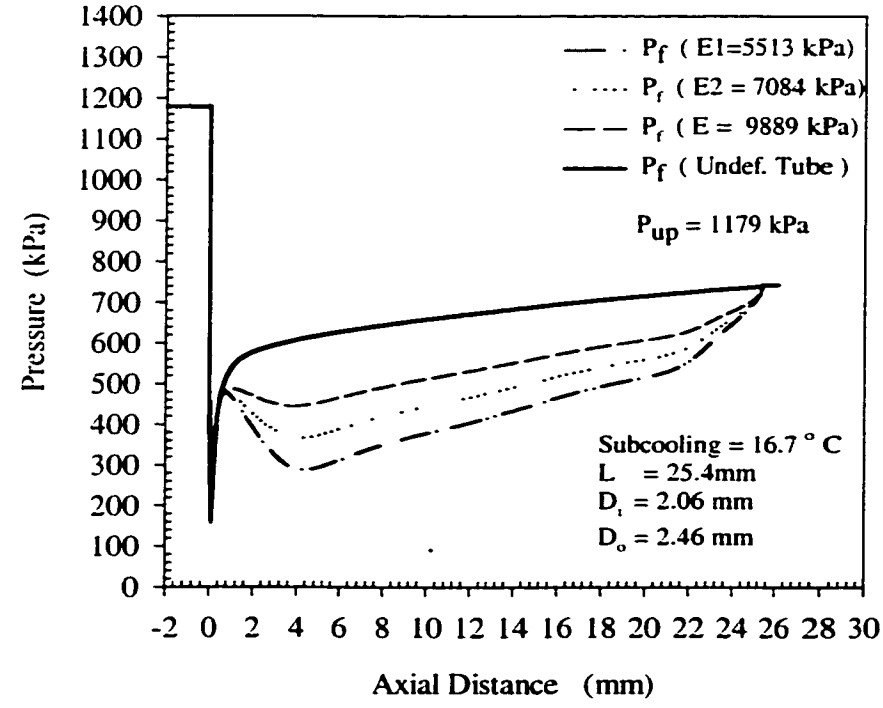

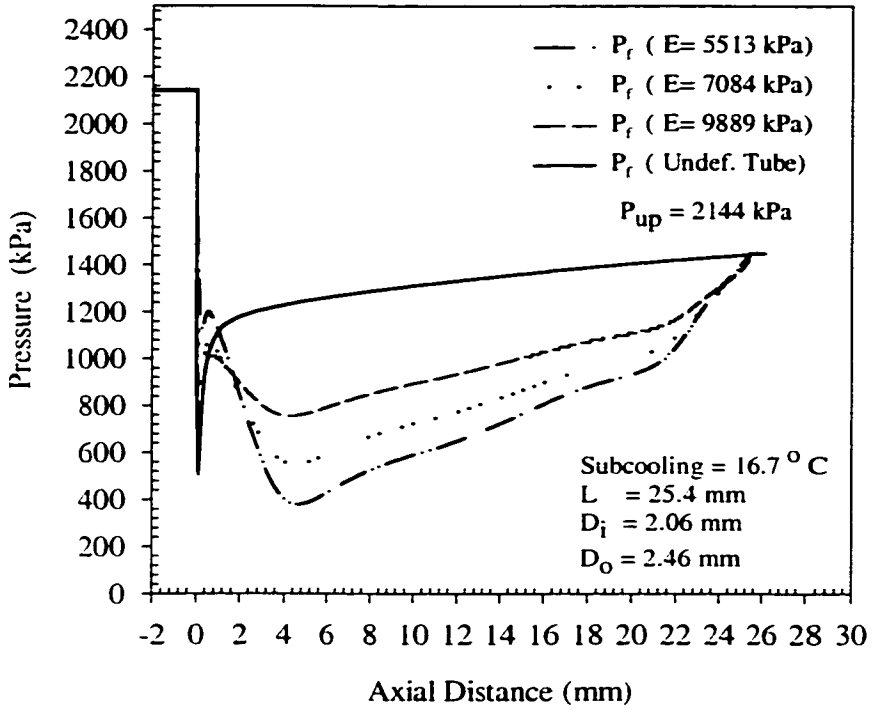

Figure 5.8 Pressure Profiles Comparison for R-22 Single Phase Flow through a Flexible Short Tube Orifice (L/D_i) for Three Moduli of Elasticity and Two Upstream Pressures .

flexibility increased, the pressure drop at the dip (3 – 4.5 mm from the tube inlet) increased by almost 28%. In addition, compared to the non deformed tube, the pressure drop at the dip, almost 4 mm from the short tube inlet, increased for the lower modulus deformed tube by almost 55%. On the other hand, as the upstream pressure was increased to 2144 kPa, a 43% increase in the sharp pressure drop at the inlet was found for the higher modulus tube over the lower modulus tube. Nevertheless, the lower modulus tube experienced a 29% pressure drop higher than the higher modulus tube at almost 4 mm from the tube inlet due to the large deformation corresponding to this axial distance.

The new deformed tube shown in Figure 5.9 can be used to help understanding the pressure behavior inside the tube. Similar to the first tube configuration $(L/D)_1$, the deformed shape resembles a converging-diverging nozzle. A distinctive increase in the chamfering-like inlet angle was observed as the upstream pressure increased for the same tube material. Figure 5.9 helps explain the lower dip in the pressure profile which corresponded to the minimum tube cross section area at an axial distance equal to approximately 4 mm from the tube inlet. According to the figure, the tube internal area contracted 36% under 1179 kPa upstream pressure, while this percentage was nearly 54% under the higher upstream pressure, 2144 kPa.

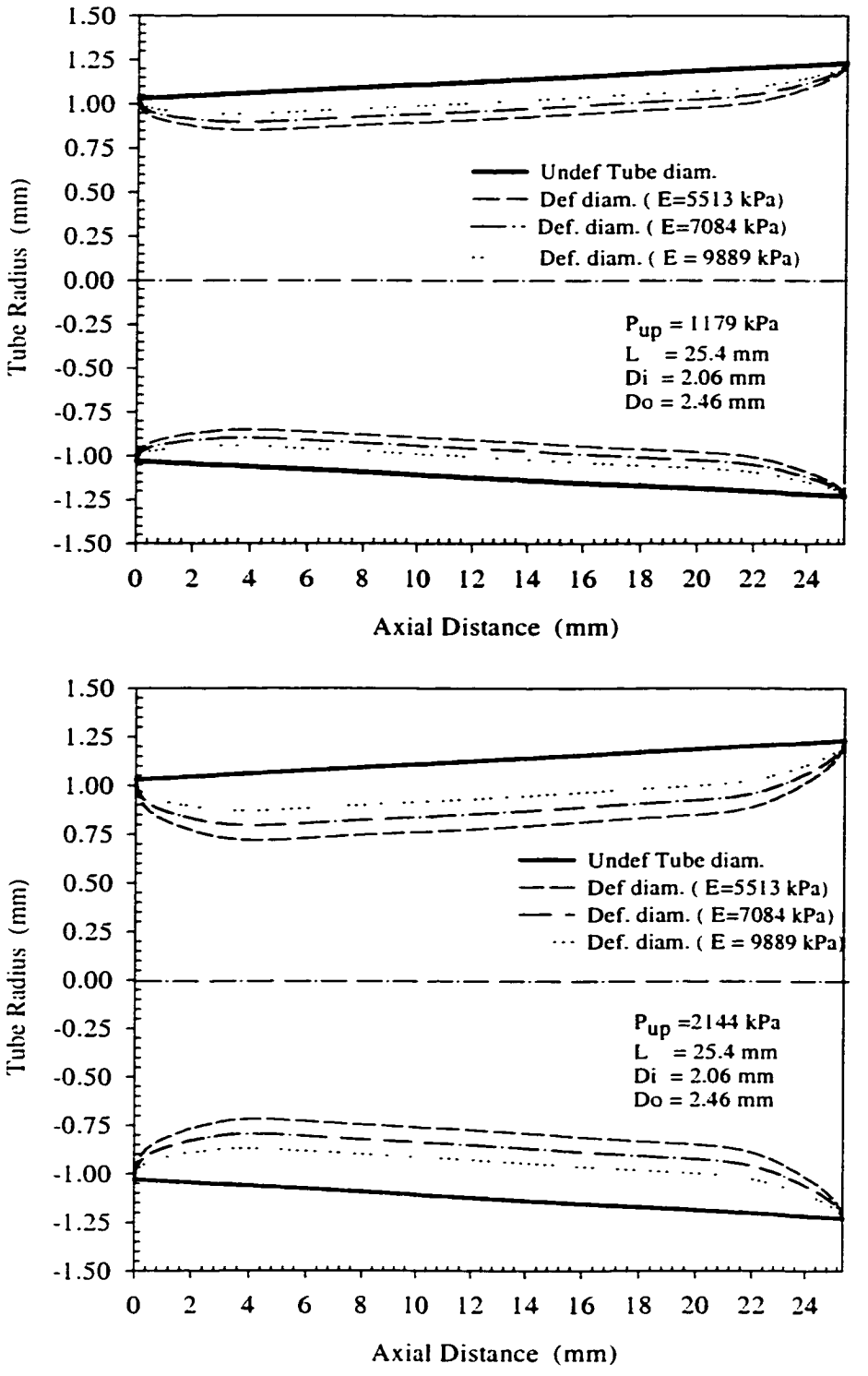

Figure 5.9 Radius Variation along the Axis of a Short Tube Orifice $(L/D)_2$ as a Result of R-22 Single Phase Flow for Three Moduli of Elasticity and Two Upstream Pressures.

Third Tube Configuration $(L/D)_3$

Figure 5.10 shows the estimated pressure profiles for the third tube configuration, $(L/D)_3$. Increasing the tube inner diameter for the same tube length, $(L/D)_3$, produced a significant change in the pressure profiles compared to those for increasing the tube length, $(L/D)_2$ (Figure 5.8) with the same upstream pressures. This trend would indicate the critical role the tube diameter plays in affecting the flow behavior. Although the profiles are qualitatively similar to those for $(L/D)_1$ (Figure 5.5), the slope of the pressure profiles in the recovery region downstream of the pressure dip (almost 4 mm from the inlet) was larger. This may be attributed to the increased flow rate for the larger diameter tube. As the mass flow rate increased, the pressure differential between the upstream and downstream sides increased.

Comparing the pressure profiles for the three tube configurations (Figures 5.5, 5.8 and 5.10) shows that influence of modulus of elasticity on pressure profiles was larger in the case of changing the diameter, $(L/D)_3$, than the tube length, $(L/D)_2$, in the range of lengths and diameters studied. A close investigation of Figure 5.10 demonstrated that under upstream pressure of 1179 kPa, the stiff tube produced a maximum pressure drop of 12% higher than the lower modulus tube. However, the pressure drop for the lower modulus tube, corresponding to the minimum internal area as shown by Figure 5.11, was 32% higher than the stiff tube. As the upstream pressure increased, pressure drop at the tube inlet as well as at the minimum cross sectional area (almost 4 mm from the inlet) increased. At the inlet of the tube, there was 39% larger

pressure drop for the stiff tube over the lower modulus tube. In a similar fashion, this is explained by analyzing Figure 5.11 and comparing the chamfering angle and depth under the two upstream pressures. At an axial distance of 4 mm from the short tube inlet, the pressure drop in the lower modulus tube increased by 42% over the stiff tube because of the decreasing of the flow free area as the tube elasticity increased.

Figure 5.11 displays the deformed tube under the different operating conditions. The deformed shape resembled a converging-diverging nozzle with deeper chamfering and bigger angle compared to Figures 5.6 and 5.8. In the figure, the tube internal area contracted by 38% under a upstream pressure of 1179 kPa which corresponded to the pressure drop increasing by 85%. When the upstream pressure increased to 2144 kPa, the area contraction increased to be 57% of the original non deformed area. Under this reduction, the pressure drop at the dip increased by almost one and half times the drop in the non deformed tube.

Kim (1993) observed experimentally that the flow dependency on tube diameter was more greater than the tube length. The mass flow rate was extremely sensitive to changes in short tube diameter and was approximately proportional to D^2. Therefore, it was necessary to investigate the diameter variation as the tube modulus of elasticity changed.

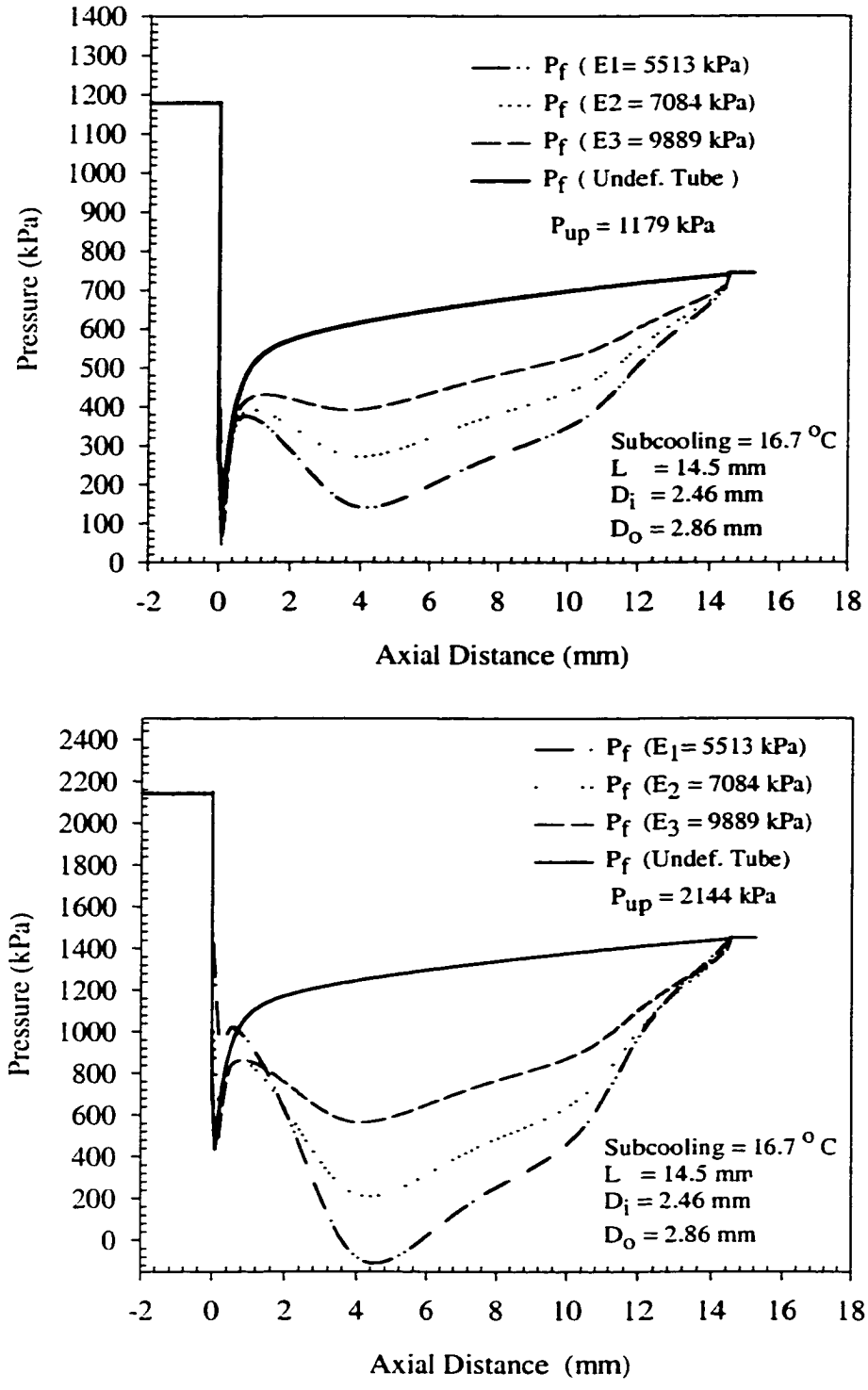

Figure 5.10 Pressure Profiles Comparison for R-22 Single Phase Flow through a Flexible Short Tube Orifice $(L/D)_3$ at Three Moduli of Elasticity and Two Upstream Pressures.

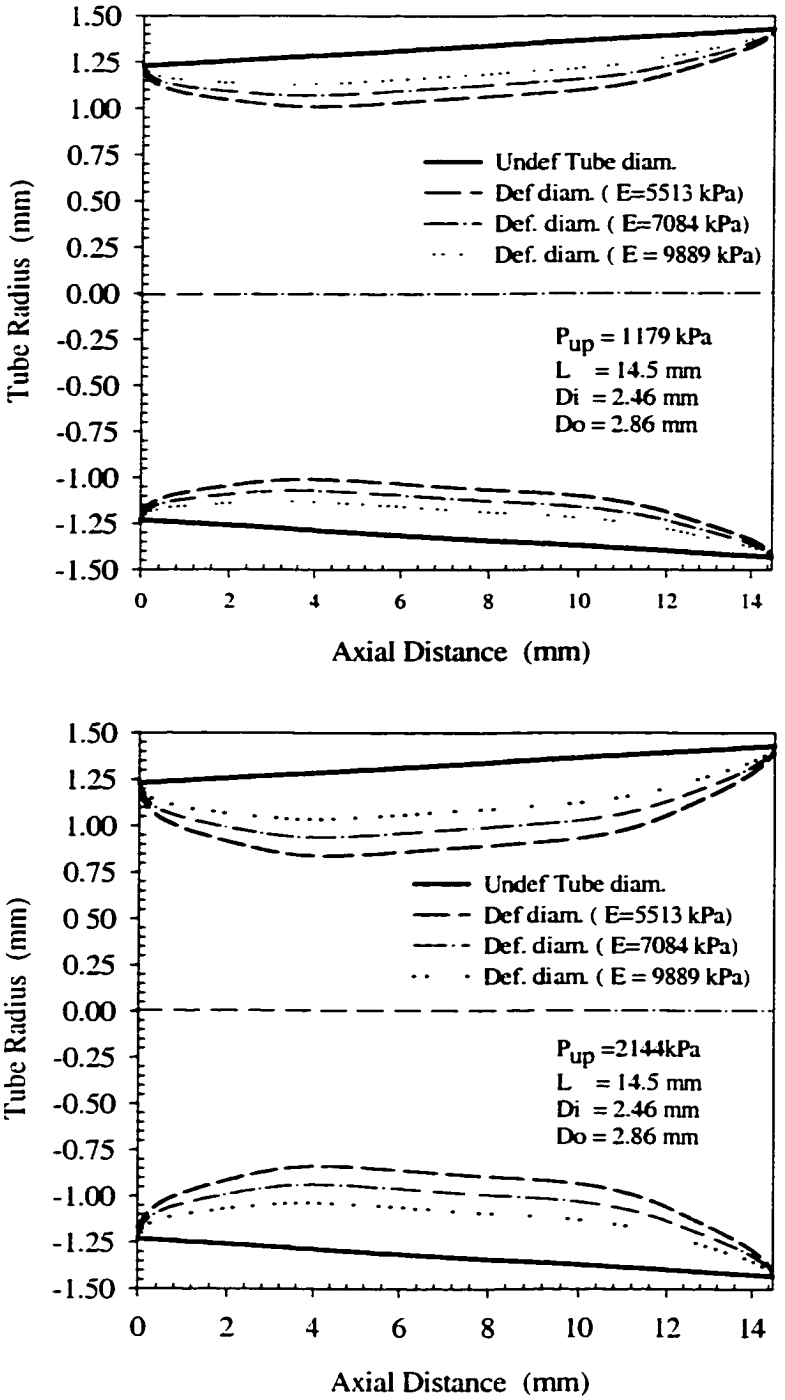

Figure 5.11 Radius Variation along the Axis of a Short Tube Orifice $(L/D)_3$ as a Result of R-22 Single Phase Flow for Three Moduli of Elasticity and Two Upstream Pressures.

A diameter ratio was defined as the deformed average diameter along the tube to the non deformed average diameter along the tube. This quantity was plotted as a function of the modulus of elasticity and upstream pressure to show the tube deformation trends (Figures 5.12 through 5.14). The trends were similar in all plots. As the modulus of elasticity increased, the diameter ratio increased which meant that the tube deformation increased for all upstream pressures. In Figure 5.12, for all upstream pressures, there was a change of the slope when the modulus of elasticity decreased beyond approximately 6800 kPa (960 psi). This indicated that under the same load, the more flexible the tube, the more sensitive response to the applied loads, and accordingly the higher the reduction in the tube cross sectional area. As the material gets stiffer, the diameter ratio was continuing to increase and would converge to unity for rigid tubes. Referring to the new axial radius distribution shown in Figure 5.7, the average increase of diameter ratio as the modulus of elasticity increased ranged from 5 to 13% as the upstream pressure varied from 1179 kPa to 2144 kPa. Similar trends are shown in Figures 5.13 and 5.14 for the other tube configurations. Both figures show that the diameter ratio increased within 8 to 15% as the modulus of elasticity increased for all upstream pressures. Thus, it can be concluded that the lower the modulus of elasticity, the lower the diameter ratio which means larger tube deformation and accordingly smaller flow diameters.

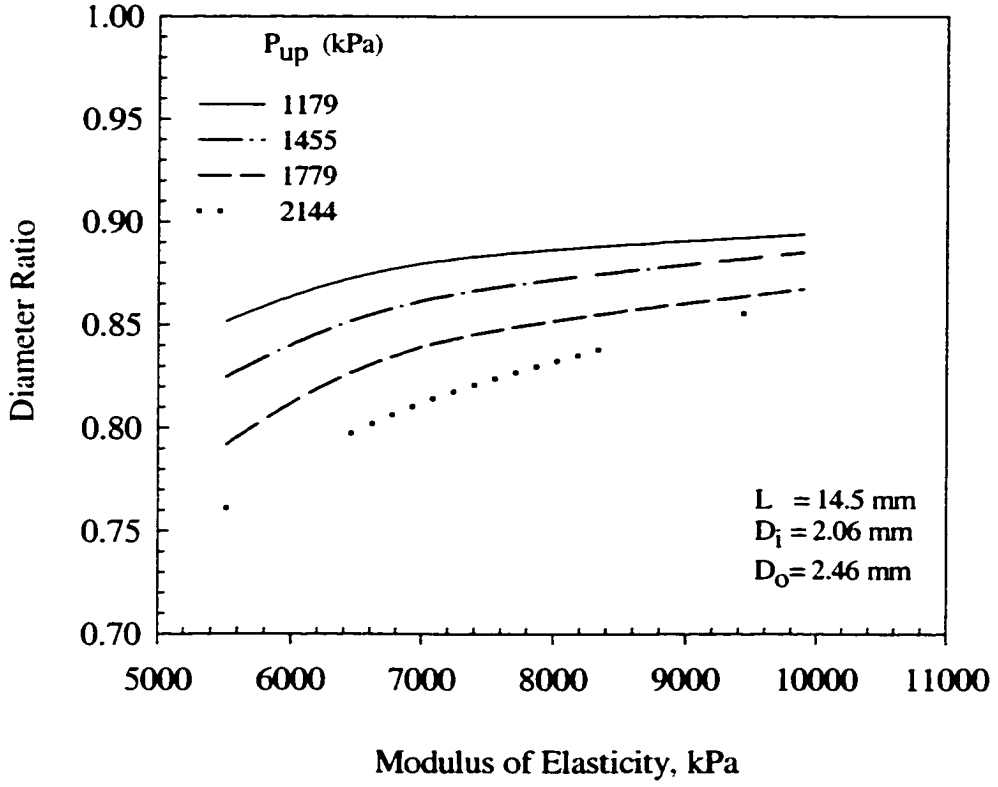

Figure 5.12 Effect of Modulus of Elasticity on Short Tube Orifice $(L/D)_1$ Diameter Variation at Different Upstream Pressures.

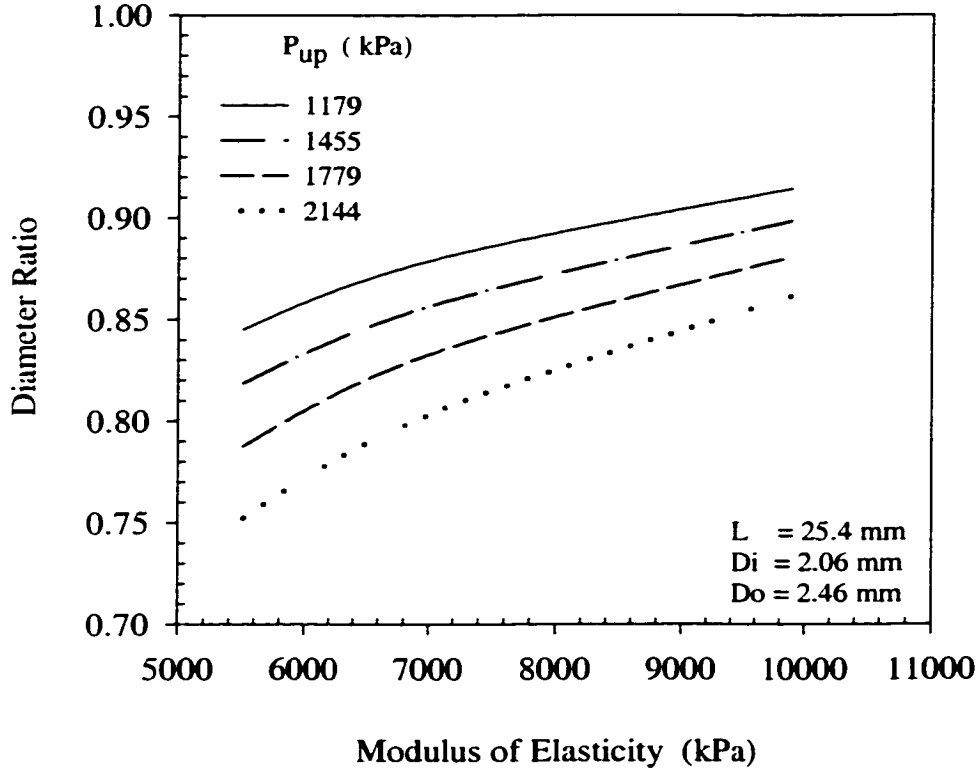

Figure 5.13 Effect of Modulus of Elasticity on Short Tube Orifice $(L/D)_2$ Diameter Variation at Different Upstream Pressures.

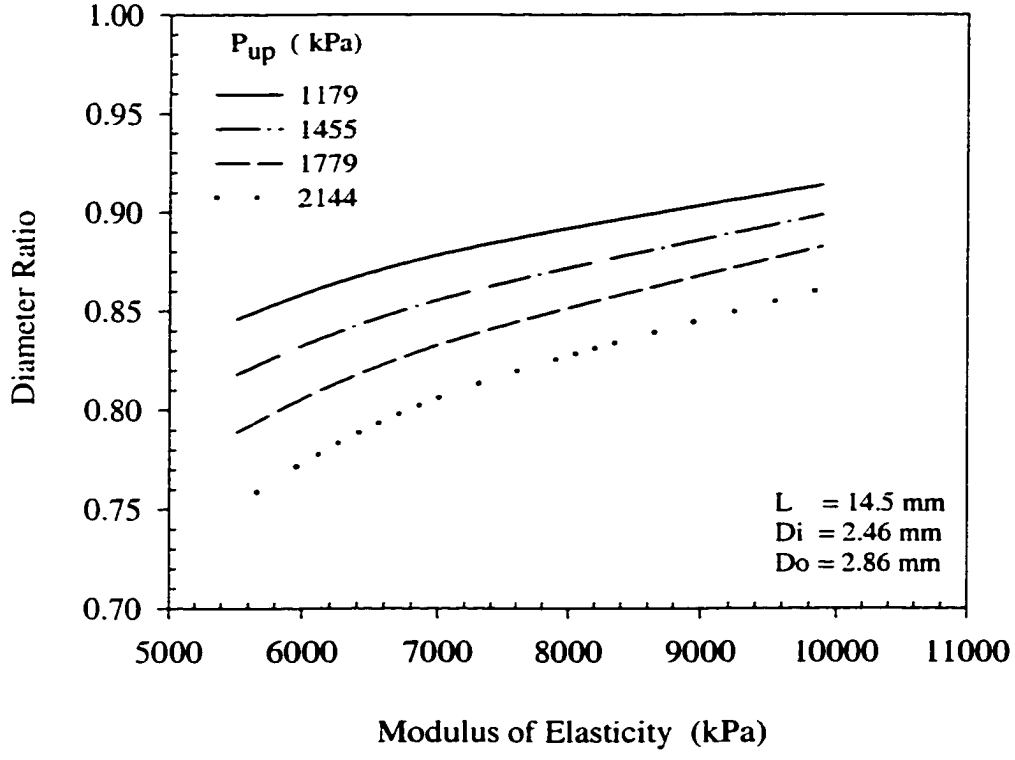

Figure 5.14 Effect of Modulus of Elasticity on Short Tube Orifice $(L/D)_3$ Diameter Variation at Different Upstream Pressures.

Effect of Modulus of Elasticity on Mass Flow Rate

The flexible short tube was designed to better control the refrigerant flow rate when the operating conditions change from the system design point. Figures 5.15 to 5.17 show the predicted mass flow rate versus modulus of elasticity at different upstream pressures. The general trend of the curves was that mass flow rate decreased as tube flexibility increased (modulus of elasticity decreases). Kim et al (1996) reported that the slope of the mass flow rate through the flexible orifice changed as a function of the modulus of elasticity of the orifice material. As the modulus of elasticity decreased below 6500 kPa (945 psi), the curves almost approached each other and showed rapid decrease in mass flow rate. Thus, reducing the modulus of elasticity of the short tube material may lead to an excessive contraction of the tube under higher upstream pressures which may overly restrict refrigerant flow. Hence, there might be a critical value for the tube modulus of elasticity under which the mass flow rate might sharply and undesirably decreases. As the modulus of elasticity increased (the tube gets stiffer), there was a tendency of the flow rate to reach a constant value for all upstream pressures at a saturation downstream pressure corresponding to the inlet upstream temperature. For upstream pressure of 1179 kPa, a constant mass flow rate was reached as the modulus of elasticity reached values greater than approximately 8500 kPa. As the upstream pressure increased, there was an increase in the slope of the curves for modulus of elasticity greater than 8500 kPa. This might be an indication that the upstream pressure exerted a force that had a significant effect on the deformation of the

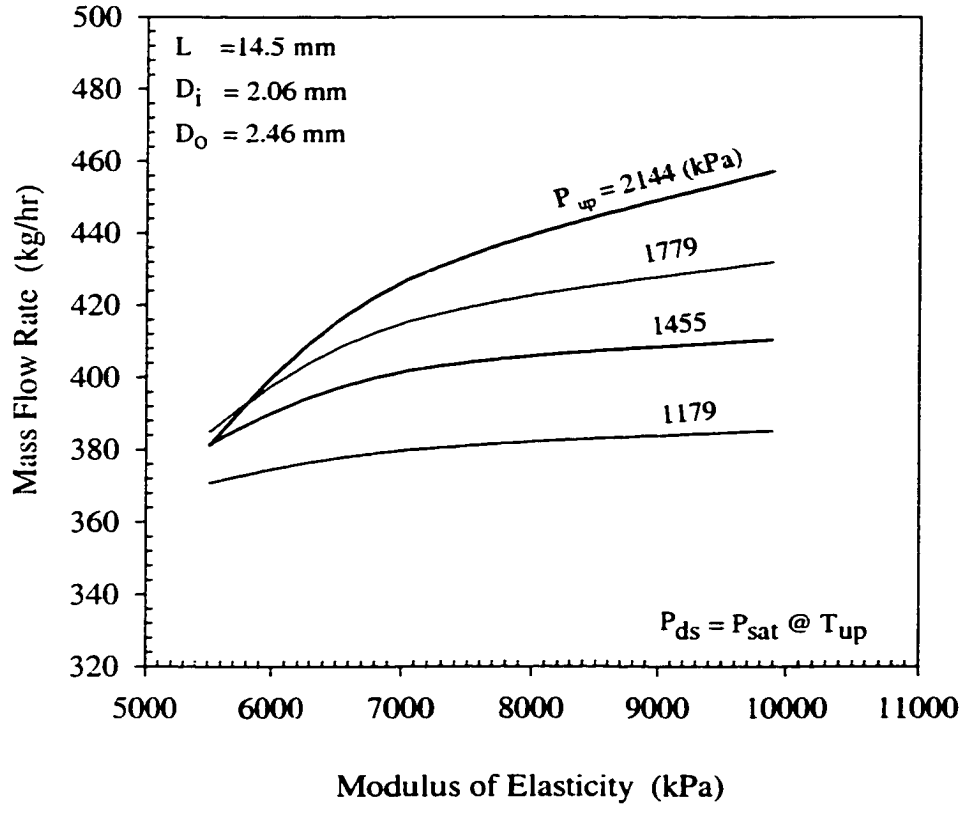

Figure 5.15 Mass Flow Rate Variation versus Tube Modulus of Elasticity for R-22 Single Phase Flow through a Flexible Short Tube Orifice $(L/D)_1$.

tube with lower modulus of elasticity (below 8500 kPa). When the modulus increased, the tube gets more stiffer to resist this exerted force. Then, the applied pressure would, no longer, significantly affect the tube deformation and hence the tube behaved as a rigid tube. For each upstream pressure, there was a different value of modulus of elasticity, at which the tube would resist the exerted force. This behavior is similar for all upstream pressures.

However, as the upstream pressure increases, the accompanied exerted force increases. Therefore, tube material with the same elasticity would have a different response to the exerted force (Figures 5.15, 5.16, and 5.17). For example, as the modulus of elasticity increased beyond 8500 kPa, the lower upstream pressures of 1179 kPa and 1455 kPa had almost no significant effect on the tube deformation. Consequently, the mass flow rate had nearly a zero slope (constant mass flow rate). However, there was a significant effect shown as an increase of the line slop as the upstream pressure increased to 1779 kPa, and 2144 kPa. Quantitatively, the increase of mass flow rate beyond a modulus of elasticity of 9000 kPa was almost zero percent for the lower upstream pressures; while it was about 5% for the higher upstream pressure.

In a similar fashion, Figures 5.16 and 5.17 illustrate the effect of the modulus of elasticity on mass flow rate for the $(L/D)_2$ and $(L/D)_3$ configurations. Increasing the tube length for the same tube diameter $(L/D)_2$ produced qualitative similar trends, but less differences between curves as the upstream pressure changes. Increasing the tube diameter

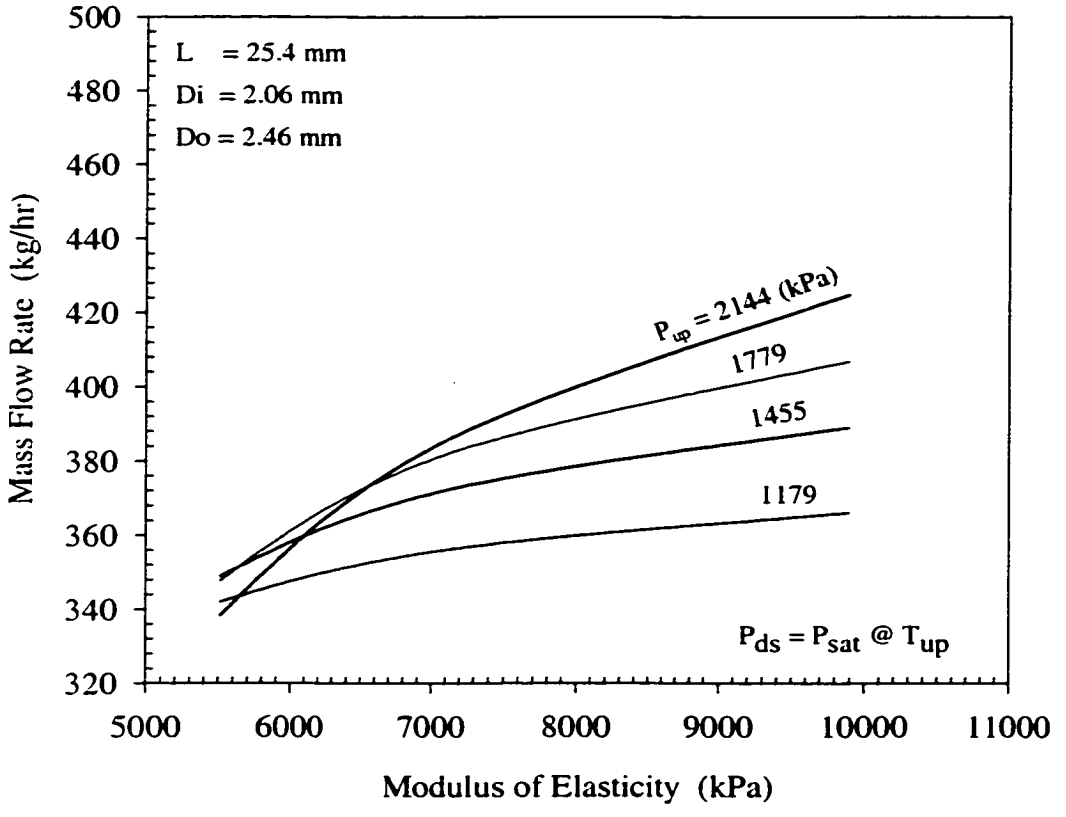

Figure 5.16 Mass Flow Rate Variation versus Tube Modulus of Elasticity for R-22 Single Phase Flow through a Flexible Short Tube Orifice $(L/D)_2$.

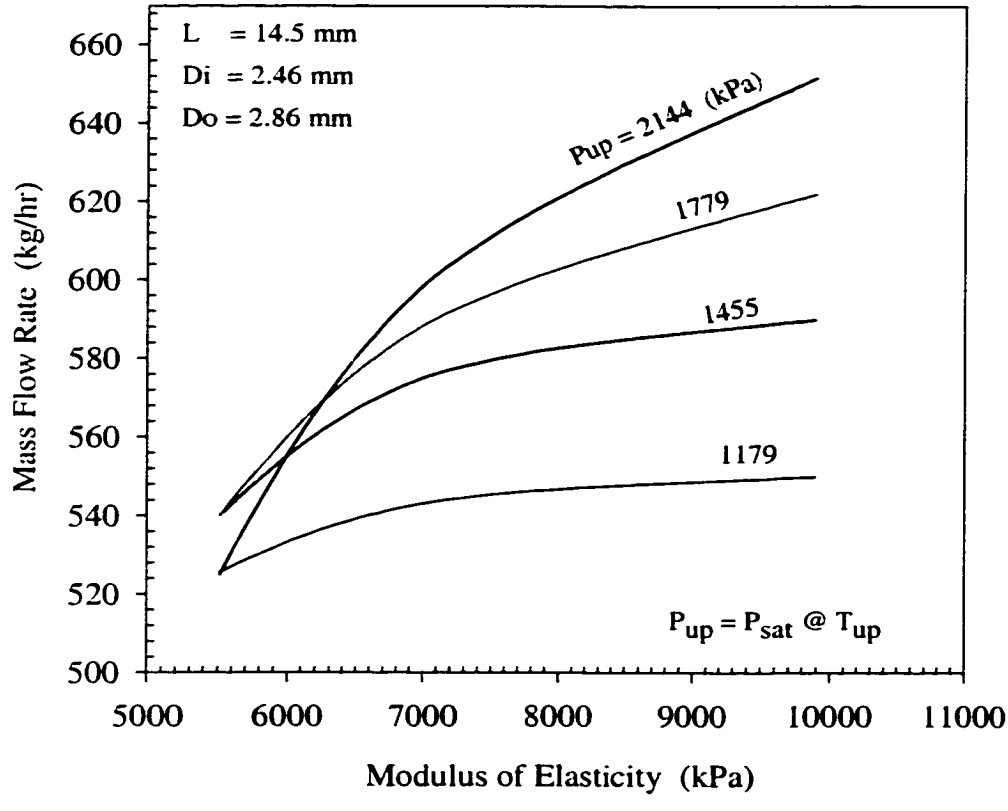

Figure 5.17 Mass Flow Rate Variation with Tube Modulus of Elasticity for R-22 Single Phase Flow through a Flexible Short Tube Orifice $(L/D)_3$.

affected the tube resistance for the same applied pressure. This is shown by the increase in mass flow under all the upstream pressures. A rapid decrease in flow rate is shown as the tube flexibility decreased for the higher upstream pressures. This is a sign that the tube resistance to the exerted force reduced as the tube gets more flexible, and so the resultant free flow area upon deformation decreased.

The third tube configuration $(L/D)_3$ had higher mass flow rates compared to the other configurations due to the larger internal free area compared to $(L/D)_1$ and $(L/D)_2$. For the same tube length but larger inner diameter, almost qualitative similar trends to Figure 5.15 were observed in Figure 5.17. A rapid drop in flow rate for the higher upstream pressure as tube gets more flexible is shown in Figure 5.17. A rough explanation for the trends shown in Figure 5.17 can be related to the increase of flow rates. Generally, increasing the pressure differential across the tube increases the mass flow rate. The net force exerted on the tube surface is proportional to this pressure differential. For the same pressure differential across the tube, increasing the tube inner diameter led to an increase in the resistible force and; therefore an increase in the flow free area. Thus, the mass flow rates increased. Similar to that shown in Figure 5.15, as the tube modulus of elasticity decreased beyond almost 6500 kPa, there was a sharp change in the slope of the mass flow as the upstream pressure increased.

Condenser Pressure Variation Effect on Tube Deformation and Pressure Profiles

The upstream pressure is an important operating parameter that affects the performance of the flexible short tube. Figure 5.18 shows the pressure profiles inside the tube for upstream saturation temperatures of 39.5 °C, 46.2 °C, and 49.5 °C with corresponding saturation pressures of 1514 kPa, 1779 kPa, and 1920 kPa, respectively. The evaporator temperature (29.5 °C) and pressure (1176 kPa) were held constant. Three subcoolings were used: 10°C, 16.7°C and 20°C. Only single-phase flow was considered. Therefore, the downstream pressure was always equal to or above the saturation pressure corresponding to the inlet temperature.

As the inlet upstream pressure increased, the pressure drop at the inlet of the tube increased at the same downstream pressure. This can be related to the higher inlet loss as the mass flow rate increased. Therefore, the local pressure everywhere along the tube was lower for the higher upstream pressure compared to the lower pressure. Very close to the inlet, a smooth pressure recovery region was established (Figure 5.18).

Downstream of the recovery region, a pressure drop was observed at an axial distances from 3.5 mm to 4.5 mm from the front edge of the orifice. The higher the upstream pressure, the more observable the dip at the same axial location. This may be attributed to the more stress on the tube material as a result of increasing the upstream pressure which led the tube to constrict more than that at the lower upstream pressure

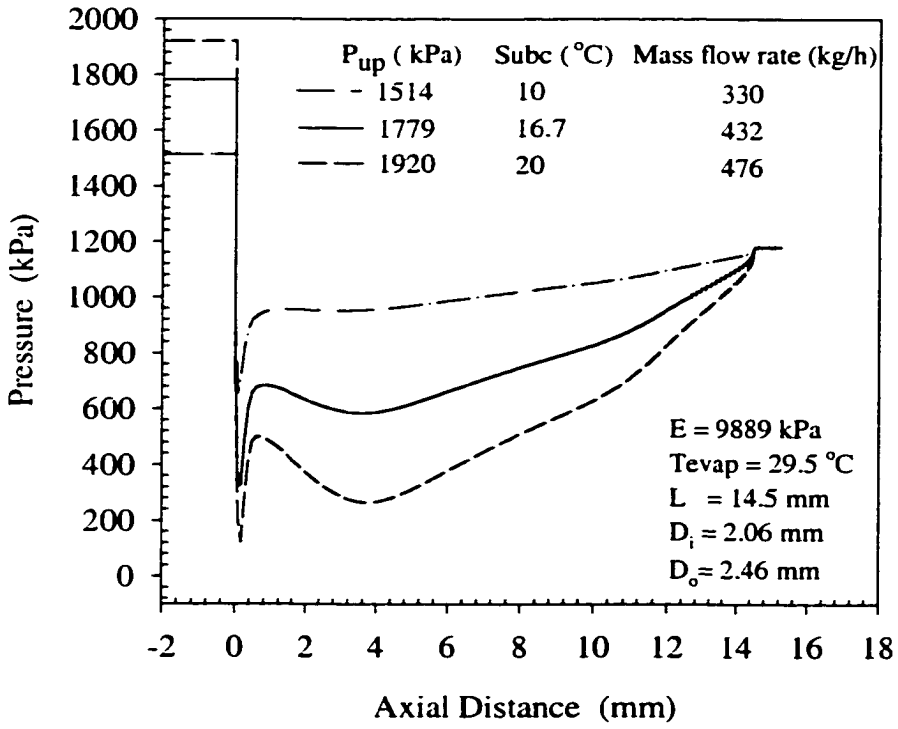

Figure 5.18 Pressure Profiles for R-22 Single Phase Flow through a Flexible Short Tube Orifice $(L/D)_1$ at Three Subcooling Levels for the Same Evaporating Temperature.

(Figure 5.19). For all upstream pressures, the pressure distribution inside the tube showed an increase downstream of the dip as a result of the diverging shape of the tube inner area downstream of the minimum constricted cross section area.

Figure 5.19 demonstrates how the tube deformed as upstream pressure was increased. The tube deformation was larger for increasing upstream pressure. The reduction in the tube inner diameter for the same material was small as a result of increasing the upstream pressure compared to that of changing the tube modulus of elasticity. As the upstream pressure increased by 27% (from 1514 kPa to 1920 kPa), there was a 33% reduction in the tube inner cross sectional area for the higher modulus of elasticity, 9889 kPa (1435 psi). Figure 5.19 shows that as the upstream pressure increased, the new tube shape was approaching a converging-diverging nozzle. This may help explain the large dip in the pressure profile for 1920 kPa corresponding to the throat minimum area.

Effect of Condenser Pressure on Mass Flow Rate

The mass flow rate through short tube orifices is dependent on the upstream pressure. Figure 5.20 shows the variation of mass flow rate through the first tube configuration $(L/D)_1$ as a function of the upstream pressure for different material flexibility. The mass flow rate increased as the upstream pressure increased. Figure 5.20 illustrates that the slope of the mass flow rate changed as a function of the tube modulus of elasticity. This was also observed by Kim et al (1996) in his experimental data. As

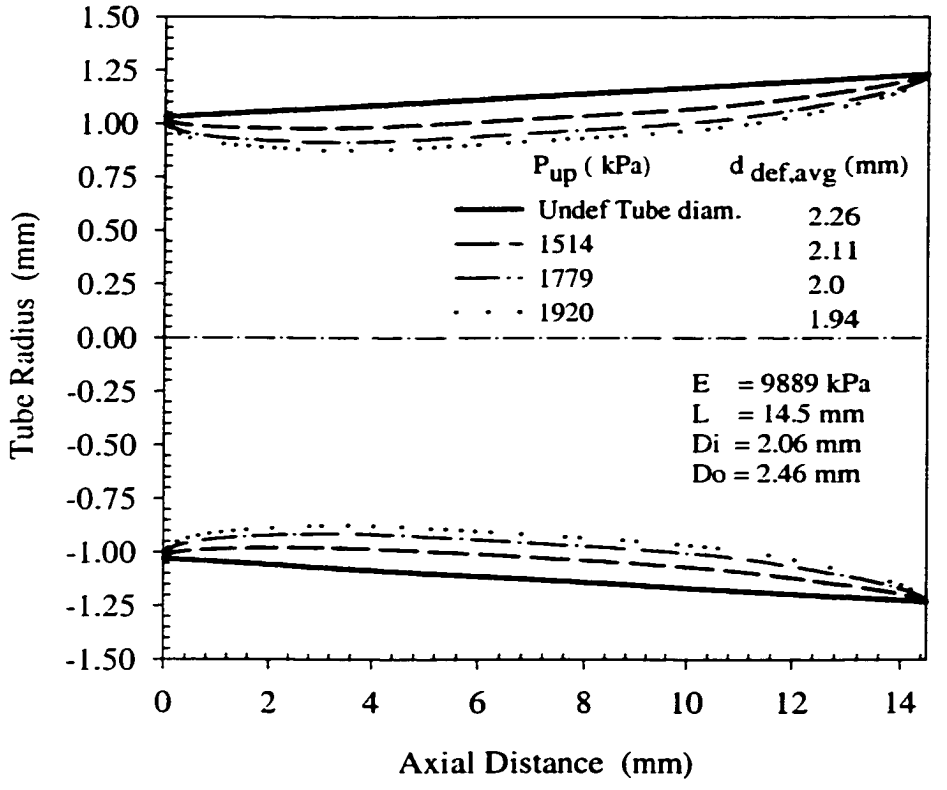

Figure 5.19 Radius Variation along the Axis of a Short Tube Orifice $(L/D)_1$ as a Result of R-22 Single Phase Flow at Three Upstream Pressures.

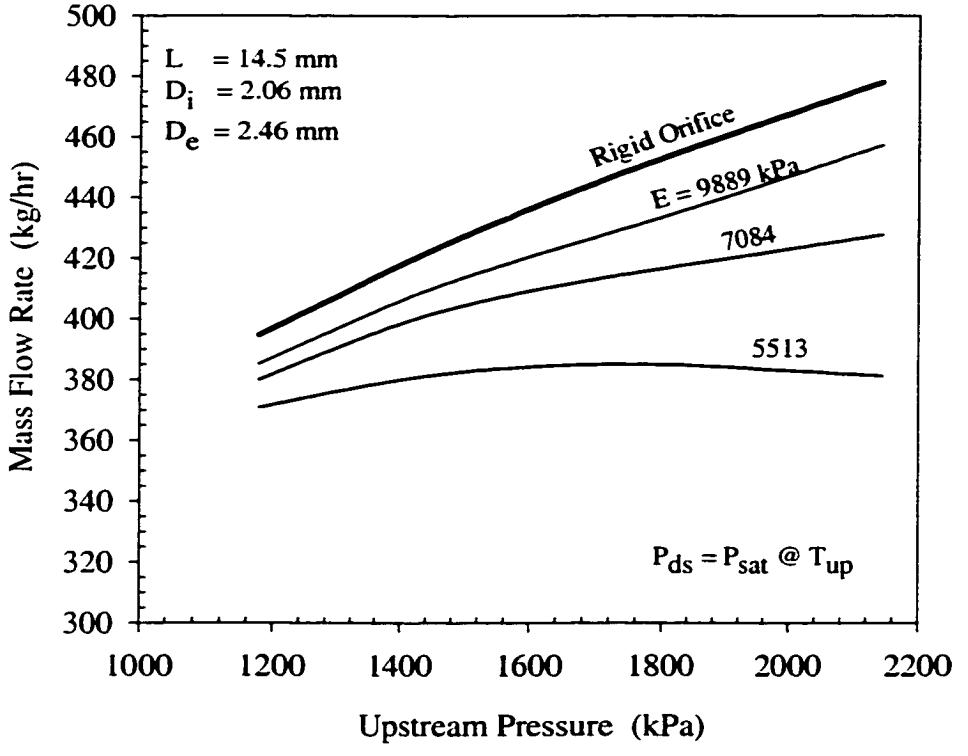

Figure 5.20 Mass Flow Rate Variation Versus Upstream Pressure for R-22 Single Phase Flow through a Flexible Short Tube Orifice $(L/D)_i$ at Three Moduli of Elasticity.

the modulus of elasticity decreases, the tube flexibility increases and hence the tube contracts more as upstream pressure increases. This concept can be noticed in the figure for the lower modulus orifice that produced a mass flow rate that averaged 10% lower than the higher modulus orifice (9889 kPa). Kim et al (1996) concluded that, based on experimental data, this average percentage was 6% for the two moduli (7084 kPa, and 9889 kPa). For the same moduli, this percentage was 4% for numerical results. Figure 5.20 illustrates that as the upstream pressure increased, the mass flow rate increased for the higher modulus of elasticity tubes. However, as the tube gets more flexible (lower modulus of elasticity), there was a tendency of the flow rate to decrease as the upstream pressure increased beyond a certain value. For a very flexible tube, the higher exerted force produced by the higher upstream pressure created an overly deformed tube which restricted the flow.

The effect of tube geometry on mass flow rate as the upstream pressure and tube modulus of elasticity change is shown in Figures 5.21 and 5.22. As the upstream pressure increased, mass flow rate increased differently for each tube modulus of elasticity. For the lower modulus tube (5513 kPa), mass flow rate increased to a certain value as the upstream pressure increased and then decreased. This may be attributed to an excessive stress exerted on the tube surface when the upstream pressure increased

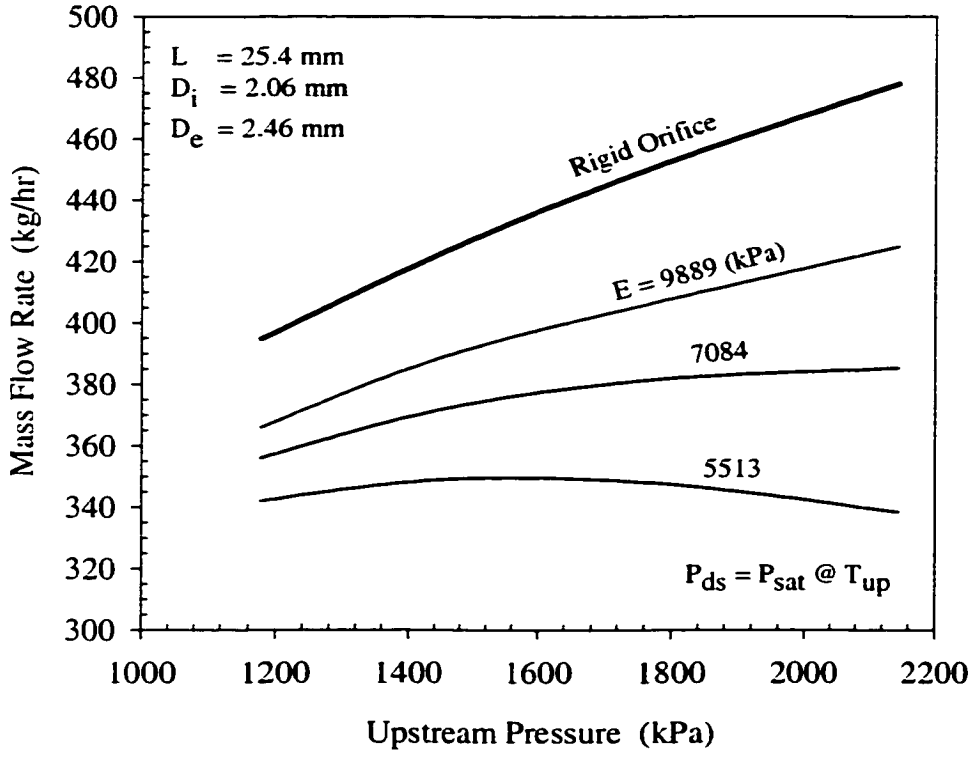

Figure 5.21 Mass Flow Rate Variation Versus Upstream Pressure for R-22 Single Phase Flow through a Flexible Short Tube Orifice $(L/D)_2$ at Three Moduli of Elasticity.

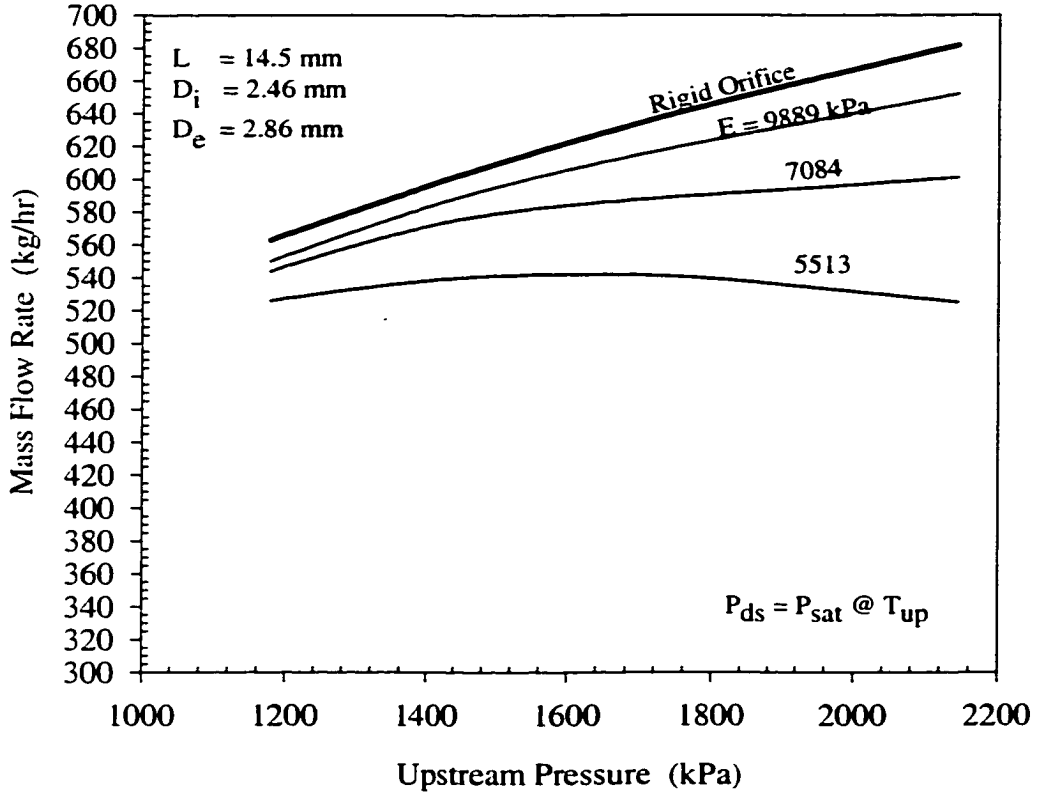

Figure 5.22 Mass Flow Rate Variation versus Upstream Pressure for R-22 Single Phase Flow through a Flexible Short Tube Orifice $(L/D)_3$ at Three Moduli of Elasticity.

beyond a certain value for which the tube resistance could not stand. Thus, it led to a large tube deformation that caused the mass flow to decrease. The trends are qualitatively similar to these of $(L/D)_1$; however, the lower modulus tube produced a mass flow that averaged 13% lower than the higher modulus tube for $(L/D)_2$ and 11% for $(L/D)_3$. On the other hand, as the upstream pressure decreased, all curves would approach a fixed value. It can be concluded that at upstream pressures lower than 1179 kPa, all the studied moduli of elasticity would produce close flow rates. This might indicate that the tube would almost equally resist the stress exerted by the lower upstream pressures. For a lower enough upstream pressure, the force exerted on the tube would be small enough that little deformation would be produced and the tube would behave as a rigid tube.

The trends of flow rate for $(L/D)_3$ configuration was qualitatively very similar to that of $(L/D)_1$. Quantitatively, the flow rates almost doubled because of the increased tube inner diameter. For $(L/D)_1$ at a higher upstream pressure, a 45% decrease of modulus of elasticity yielded a 17% decrease in mass flow rate. However, this percentage reached 4% at the lower upstream pressure. Similarly for $(L/D)_2$, this percentage was 20% at the higher pressure and 7% at the lower upstream pressure. As the tube diameter increased, $(L/D)_3$, there was a 19% decrease in mass flow rate as the modulus of elasticity decreased by 45% at the higher upstream pressure and 4% at the lower upstream pressure. These percentages were almost similar to that for $(L/D)_1$.

A summary for the numerical predicted mass flow rate is given in Table 5.1. A list of the average tube diameter after tube deformation is presented in Table 5.2 as well.

Mass Flow Rate Correlation Development

A mass flow rate correlation was developed to predict single-phase flow at the inlet of the flexible short tube for R-22. The correlation was based on the numerical results. The single-phase flow orifice equation was modified to include a pre-flashing pressure called P_{th} instead of the downstream pressure. The orifice equation and its assumptions are listed below, Aaron and Domanski (1990):

$$\dot{m} = C A_s \sqrt{\frac{2 \rho g_{ca} (P_{up} - P_{down})}{(1 - \beta^4)}} \tag{5.1}$$

Because the flexible short tube has a small surface area and a low thermal conductivity, the orifice is assumed adiabatic. The tube was modeled in a horizontal shape such that the potential effects were neglected. It was observed that the pressure at the inlet was near the saturation pressure and the temperature at the inlet was almost near the upstream liquid temperature (Aaron and Domanski 1990). This observation supported the assumption of isothermal flow. Because the study dealt with a single-phase liquid flow, the flow was assumed steady. There was no external work performed by the refrigerant on the control volume.

Table 5.1 Summary of Numerical Predicted Results for Mass Flow Rate of R-22 Single Phase Flow.

	MASS FLOW RATE (kg/h)								
	$(L/D)_1$, $D_{un,avg}$ = 2.26 (mm)			$(L/D)_2$ $D_{un,avg}$ = 2.26 (mm)			$(L/D)_3$ $D_{un,avg}$ = 2.66 (mm)		
P_{up} (kPa)	E1= 5513 (kPa)	E2= 7084 (kPa)	E3= 9889 (kPa)	E1= 5513 (kPa)	E2= 7084 (kPa)	E3= 9889 (kPa)	E1= 5513 (kPa)	E2= 7084 (kPa)	E3= 9889 (kPa)
1179	371	380	385	342	356	366	526	544	550
1455	382	402	410	349	372	389	540	576	590
1779	385	416	432	348	382	407	540	590	622
2144	381	428	457	338	385	425	525	601	652

*** *Subcooling = 16.7 °C*

*** *Downstream pressure is the saturation pressure corresponding to the inlet temperature.*

*** *$(L/D)_1$: L=14.5 mm, D_i=2.06 mm, D_o=2.46 mm*

*** *$(L/D)_2$: L=25.4 mm, D_i=2.06 mm, D_o=2.46 mm*

*** *$(L/D)_3$: L=14.5 mm, D_i=2.46 mm, D_o=2.86 mm*

Table 5.2 Summary of Numerical Results of Average Inner Diameter after Deformation for R-22 Single Phase Flow.

	Average Diameter (mm)								
	$(L/D)_1$ $D_{un,avg}$ = 2.26 (mm)			$(L/D)_2$ $D_{un,avg}$ = 2.26 (mm)			$(L/D)_3$ $D_{un,avg}$ = 2.66 (mm)		
P_{up} (kPa)	E1= 5513 (kPa)	E2= 7084 (kPa)	E3= 9889 (kPa)	E1= 5513 (kPa)	E2= 7084 (kPa)	E3= 9889 (kPa)	E1= 5513 (kPa)	E2= 7084 (kPa)	E3= 9889 (kPa)
1179	1.93	1.99	2.07	1.91	1.9	2.07	2.25	2.34	2.43
1455	1.86	1.95	2	1.85	1.94	2.03	2.18	2.28	2.39
1779	1.79	1.9	2	1.78	1.89	1.99	2.1	2.22	2.35
2144	1.72	1.84	1.95	1.7	1.82	1.95	2	2.15	2.29

*** *Subcooling = 16.7 ^{o}C*

*** *Downstream pressure is the saturation pressure corresponding to the inlet temperature.*

*** *$(L/D)_1$: L=14.5 mm, D_i=2.06 mm, D_o=2.46 mm*

*** *$(L/D)_2$: L=25.4 mm, D_i=2.06 mm, D_o=2.46 mm*

*** *$(L/D)_3$: L=14.5 mm, D_i=2.46 mm, D_o=2.86 mm*

For these assumptions to be valid, the control volume was chosen between the upstream pressure and very close to the tube inlet what was called the throat pressure as a result of a similar to converging-diverging shape of the tube after deformation.

According to the above-mentioned assumptions in addition to neglecting the value of the ratio of the tube diameter to the upstream tube diameter to the fourth power, β^4, compared to one, the orifice equation is written in the form:

$$m^{\bullet} = A_s * \sqrt{2 \rho g_{ca} \left(P_{up} - P_{th}\right)} \qquad (5.2)$$

assuming the flow coefficient is unity, and replacing the downstream pressure with the throat pressure.

The pre-flashing pressure, throat pressure, was correlated to the different operating and geometrical parameters after normalization through a nonlinear correlation based on the numerical results using a nonlinear regression program as:

$$P_{th} = Psat \left\{ \begin{array}{c} 0.4541 + 7.507\,(PRAT1)^{-0.4422}\,(TPAT)^{1.369} - 1.614\,(PRAT2)^{0.4253} \\ + 0.0058\,(L/D)^{1.225} + 1.322\,Ln\,(E/Er)^{-0.1424} \end{array} \right\} \qquad (5.3)$$

Where;

$PRAT1 = P_{up}/P_c$

$PRAT2 = (P_c - P_{down})/P_c$

$TRAT = (T_{sat} - T_{up})/T_c$

Er = Reference Modulus of Elasticity, 129×10^6 kPa (Rigid tube)

Equation (5.3) can be used to roughly predict refrigerant mass flow rate through flexible short tube orifices under certain limitations. These limitations are listed in Table 5.3.

Table 5.3 Limitations for Implementing Equation 5.3.

Parameter	Limit
P_{up}	1179 kPa (171 psi) – 2144 kPa (311 psi)
P_{down}	742 kPa (108 psi) – 1448 kPa (210 psi)
L	14.5 mm (0.57 in) – 25.4 mm (1 in)
D_i	2.06 mm (0.081 in) – 2.46 mm (0.097 in)
D_o	2.46 mm (0.097 in) – 2.86 mm (0.113 in)
Subcooling	16.7 °C (single phase)
E	5513 kPa (800 psi) – 9889 kPa (1435 psi)

The validity of the predicted flow model was verified by comparing the correlation-based predicted flow rates with the numerical results and published experimental data by Kim et al (1996). Although the experimental data had a 1.2% oil by mass flowing with the refrigerant, there were similar trends with both the correlation-based values and the numerical results for two different moduli of elasticity as shown in Figures 5.23.

Figure 5.23 shows the dependence of mass flow rate on upstream pressure for two moduli of elasticity (7084 kPa and 9889 kPa), comparing the numerical and the correlation-based results to the experimental data. It is shown the slope change of the mass flow rate as the upstream pressure increased beyond 1450 kPa. This change was observed in the numerical results as well as in the correlation-based values. The maximum difference percentage between the correlation-based mass flow rate and the experimental results was 13%, while the maximum difference between the numerical and experimental data was 16%. The correlation underpredicted the flow rate by almost 3% compared to the numerical results.

Similarly, for the higher modulus tube, Figure 5.23 shows higher mass flow rates compared to those for the less modulus of elasticity. This is due to the less tube deformation at the higher modulus of elasticity compared to the lower modulus under the same applied pressure load. Also, the maximum difference percentage between the correlation-based mass flow rate and the experimental results was almost 13%, while this difference was 14% between the numerical and experimental data. The absolute difference percentage between the predicted flow rate using the non linear model and the numerical results was almost around 2%.

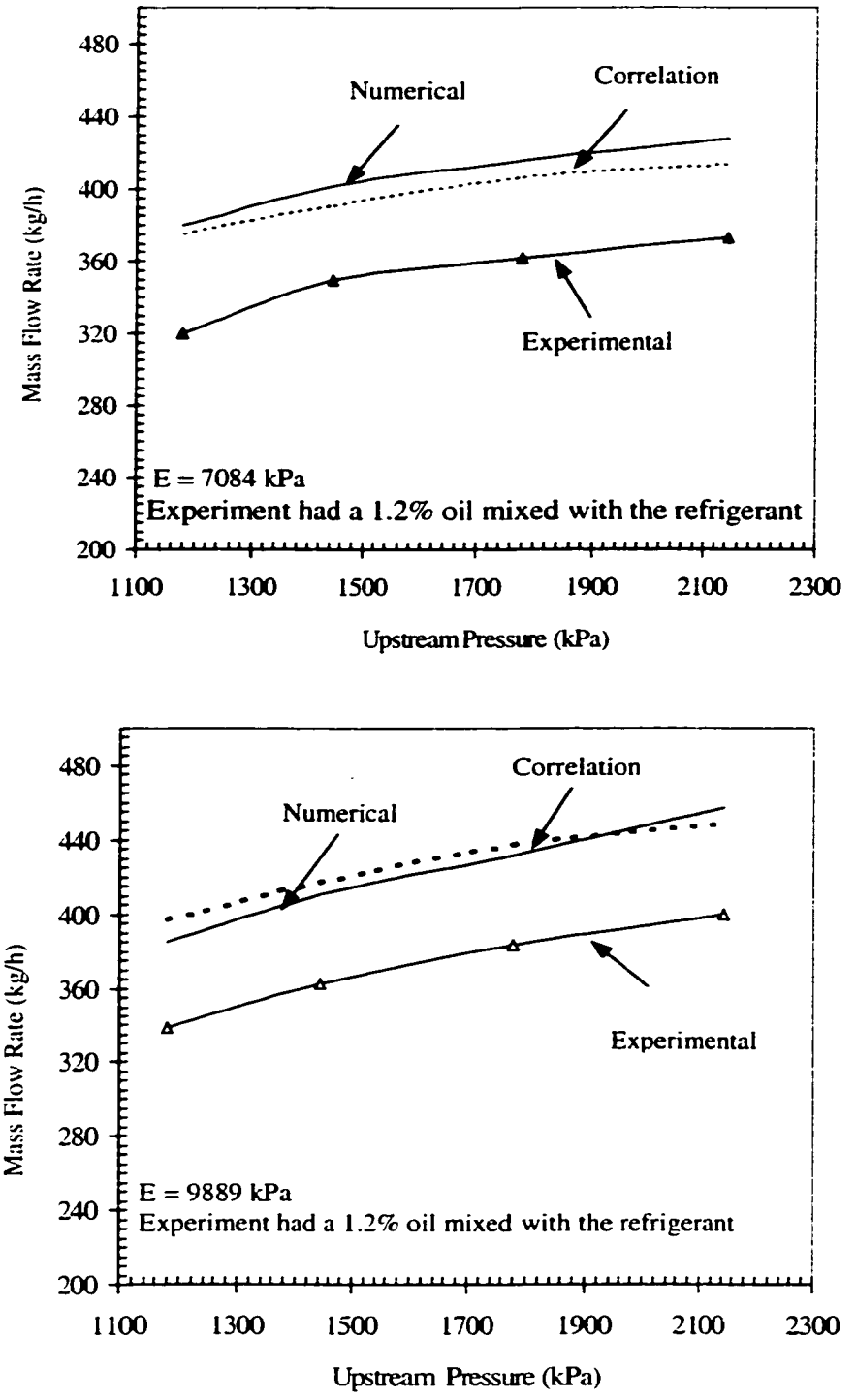

Figure 5.23 A Comparison between the Numerical and the Correlation-Based Mass Flow Rate with the Experimental Values for Two Moduli of Elasticity.

A correction factor was observed between both numerical and correlation-based values with the experimental results. This correction factor minimized the difference between the flow rate trends. Figure 5.24 illustrates a comparison between the corrected numerical and correlation-based results with the experimental values for two moduli of elasticity. This correction factor was found to be 87.24%, approximately, which can be used to roughly predict experimental data based on numerical estimations. As shown in Figure 5.24, applying this correction factor reduced the difference between the numerical and correlation-based values with the experimental results to almost 2%.

Summary of R-22 Results

Upon deformation, the tube shape resembled a converging-diverging nozzle. The tube had a chamfered-like inlet and outlet as a result of deformation caused by upstream pressure. A significant increase (almost from 3° to 8°) in the chamfering-like inlet angle was observed as the modulus of elasticity decreased. The lower the modulus of elasticity, the less pressure drop at the tube inlet due to the chamfered-like inlet after deformation, and the higher pressure drop along the tube due to the higher tube contraction.

Increasing the tube inner diameter for the same tube length produced a significant change in the pressure profiles compared to those for increasing the tube length under the same upstream pressure. The maximum pressure drop occurred at the

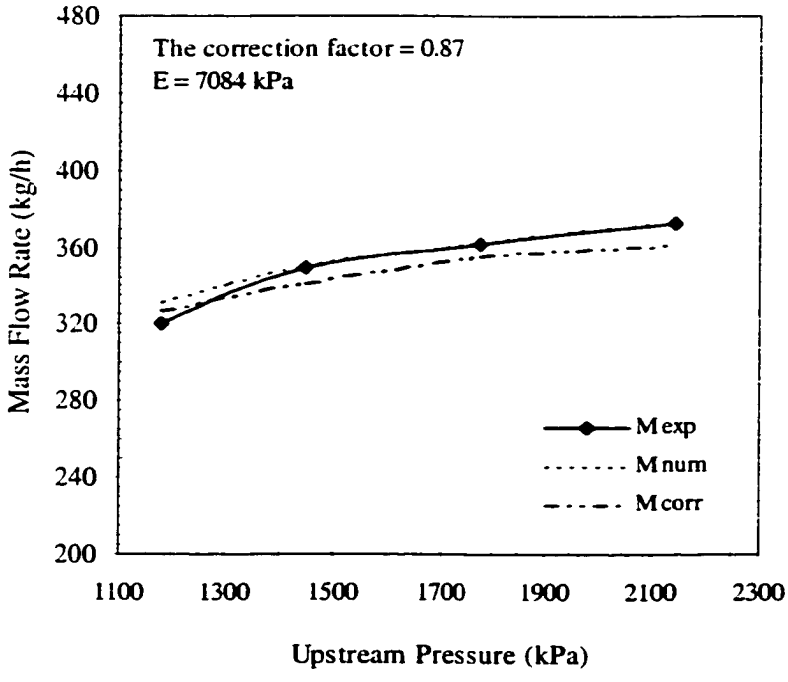

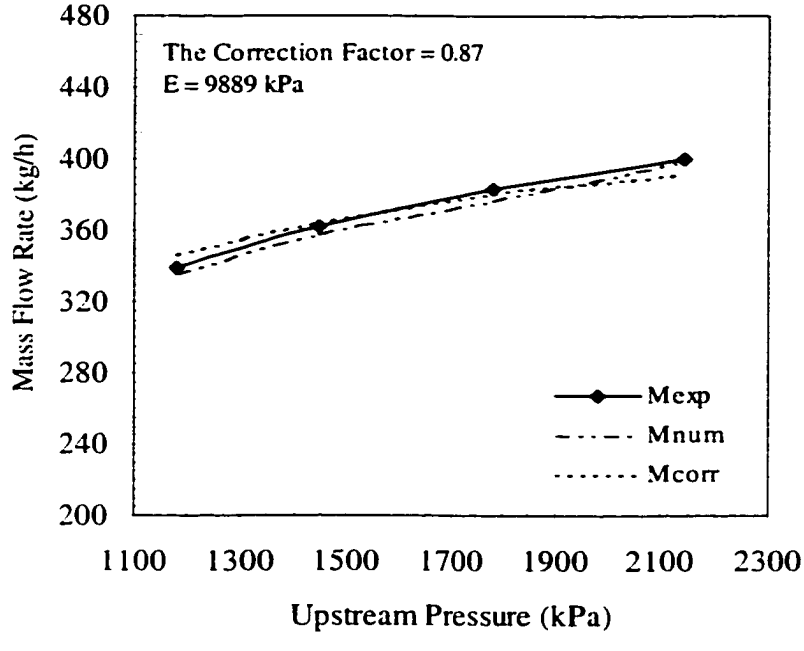

Figure 5.24 Comparing the Corrected Numerical and Correlation-Based Mass Flow Rate with the Experimental Values for Two Moduli of Elasticity.

dip (4 mm from the inlet) for $(L/D)_3$ was almost 5% above the other two geometries $(L/D)_1$ and $(L/D)_2$. Hence the diameter has a significant effect on pressure drop and accordingly on mass flow rate more than the tube length.

As the modulus of elasticity decreased, the mass flow rate decreased for all upstream pressures and it approached each other beyond a certain value of modulus of elasticity. Similarly, as the upstream pressure increased, the mass flow rate increased for all moduli of elasticity; however, the lower modulus tube exhibited a lower flow rate that tended to decrease as the upstream pressure increased.

CHAPTER VI

RESULTS AND DISCUSSION FOR R-134a AND R-410a

As a result of international agreements and treaties for the phase out of refrigerants that directly affect the ozone depletion and lead to the global warming, R-134a and R-410a are being used as replacements for R-12 and R-22, respectively. The behavior of these replacement refrigerants with orifices needs to be tested. Hence as a part of this study, a numerical investigation of the flow behavior of R-134a and R-410a through flexible short tube orifices under various operating conditions was performed. One tube configuration with different material moduli of elasticity, 5513 kPa (800 psi), 7084 kPa (1028 psi), and 9889 kPa (1435 psi) was chosen and simulated. The pressure variation inside flexible short tubes along with tube deformation and consequently its effect on mass flow rate is presented in this chapter for both R-134a and R-410a.

Pressure Variation Inside Short Tube

Tracking of refrigerant pressure variation inside flexible short tubes leads to a better understanding and prediction of flashing and formation of two-phase mixture when the internal pressure reaches the saturation pressure corresponding to the inlet refrigerant temperature. This information mainly helps the designer to modify the tube design and, accordingly, improve the heat pump performance.

Figure 6.1 shows the pressure variation of R-134a inside a flexible short tube at successive coupled (global) iterations until the pressure converged. The pressure profile

inside the non deformed flexible short tube is shown in this figure corresponding to the first iteration. Similar to R-22 profiles inside the flexible short tube, very small dips in the pressure profiles were observed close to the tube inlet downstream of the pressure recovery. The figure shows the gradual change in pressure profiles between coupled iterations till there was almost a negligible change in the pressure trend between the third and fourth coupled iterations.

Using R-410a through the same tube configuration at the same condensing temperature (46 °C) and subcooling (16.7 °C) yielded the pressure profiles shown in Figure 6.2. Under the same condensing temperature, R-410a exhibits almost 50% higher in upstream pressure than R-22. Figure 6.2 displays qualitative similar trends to these of R-22 at the same condensing temperature. However, Figure 6.2 illustrates large pressure dip midway through the tube as the upstream pressure increased for the same tube geometry compared to R-22, Figure 5.5, and R-134a, Figure 6.1. Further, at the first coupled iteration, the figure displays the smooth pressure profile for the flow through the tube before deformation. The converged pressure profile at the fourth coupled iteration, after which there was no significant change in the profile, is shown in the figure as well.

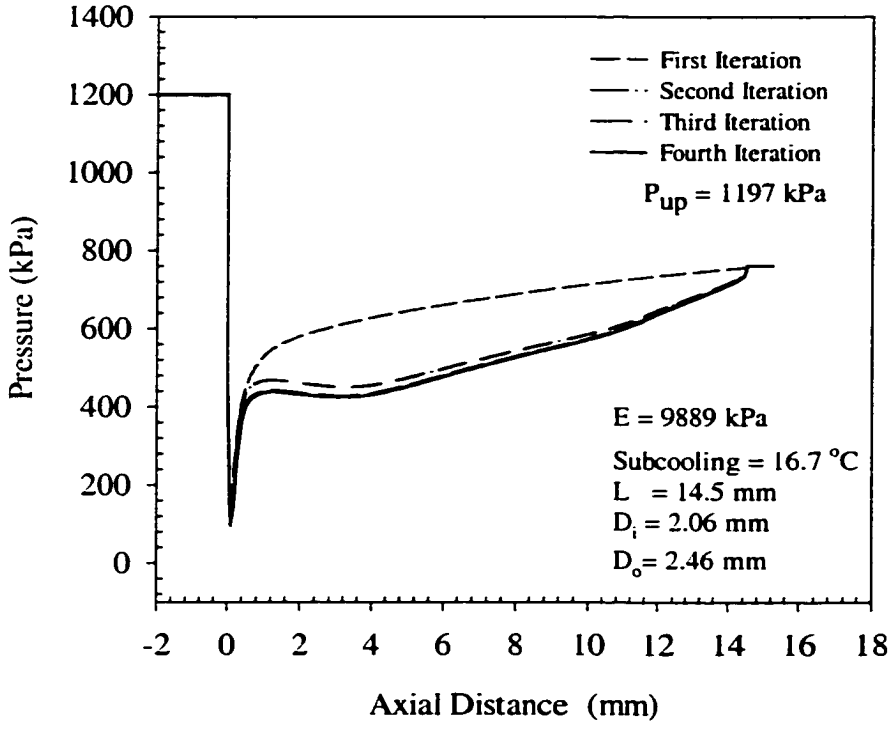

Figure 6.1 : Pressure Profiles for R-134a Single Phase Flow through a Flexible Short Tube Orifice $(L/D)_1$ at Successive Global Iterations.

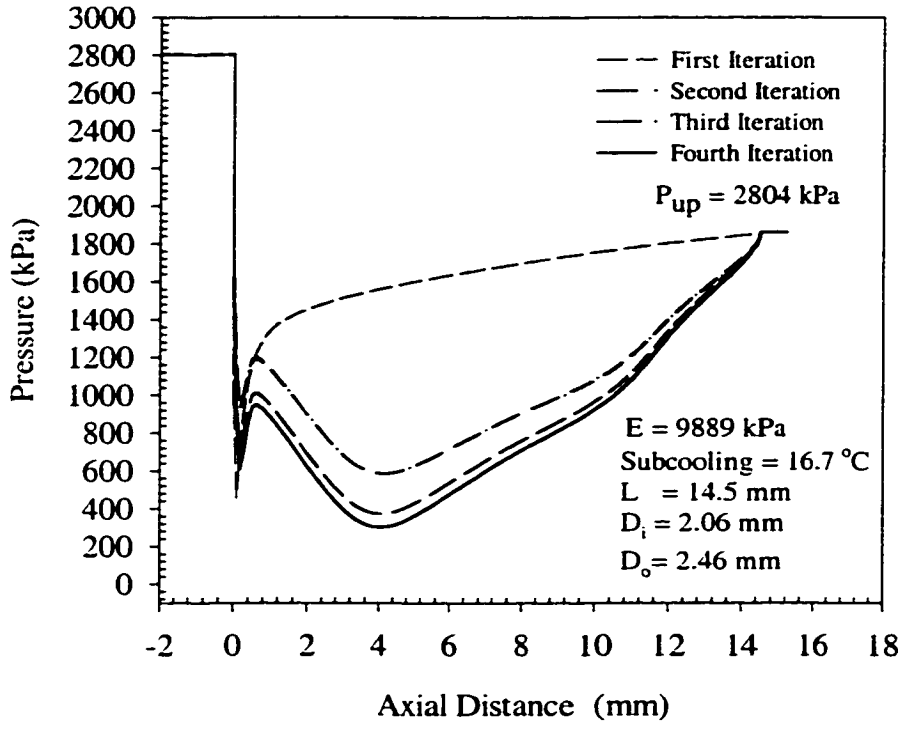

Figure 6.2 Pressure Profiles for R-410a Single Phase Flow through a Flexible Short Tube Orifice $(L/D)_1$ at Successive Global Iterations.

The pressure profiles for flow of R-134a and R-22 through a flexible short tube at different tube moduli of elasticity and at the same condensing temperature are shown in Figures 6.3a and 6.3b, respectively. Figure 6.3a indicates that the more flexible tube (5513 kPa) yielded the lower axial pressure profile and, accordingly the maximum pressure drop along the flexible tube. A sharp pressure drop was captured at the inlet, as shown in the figure, due to a rapid acceleration of the flow as a result of the sudden contraction in the tube cross sectional area. As the modulus of elasticity decreased, the inlet edge buckled forming a larger chamfering angle upon tube deformation. Therefore, the sharp pressure drop decreased at the inlet. Figure 6.3a displays that as the tube flexibility increased by 45% (decrease in modulus of elasticity) from 9889 kPa to 5513 kPa, a 28% increase in the pressure drop at the dip (almost 4 mm from the tube inlet) was observed. Downstream of the dip, a pressure recovery due to the divergent section of the tube was noticed (Figure 6.3a).

The pressure profiles for R-410a single-phase flow through a flexible short tube at two moduli of elasticity are illustrated in Figure 6.4. The figure shows the effect of using R-410a, which has almost 50% higher pressure than R-22 when operating at the same condenser temperature. The figure shows a large dip in the pressure profiles downstream of the tube inlet compared to R-134a (Figure 6.3a) and R-22 (Figure 6.3b) at the same condensing temperature. Furthermore, the sharp pressure drop at the tube inlet decreased as the tube became more flexible, as shown in Figure 6.4. This is an indication of the chamfered-like inlet of the tube upon deformation. The more flexible the material, the larger the chamfering effect at the inlet and, accordingly the less the pressure drop at

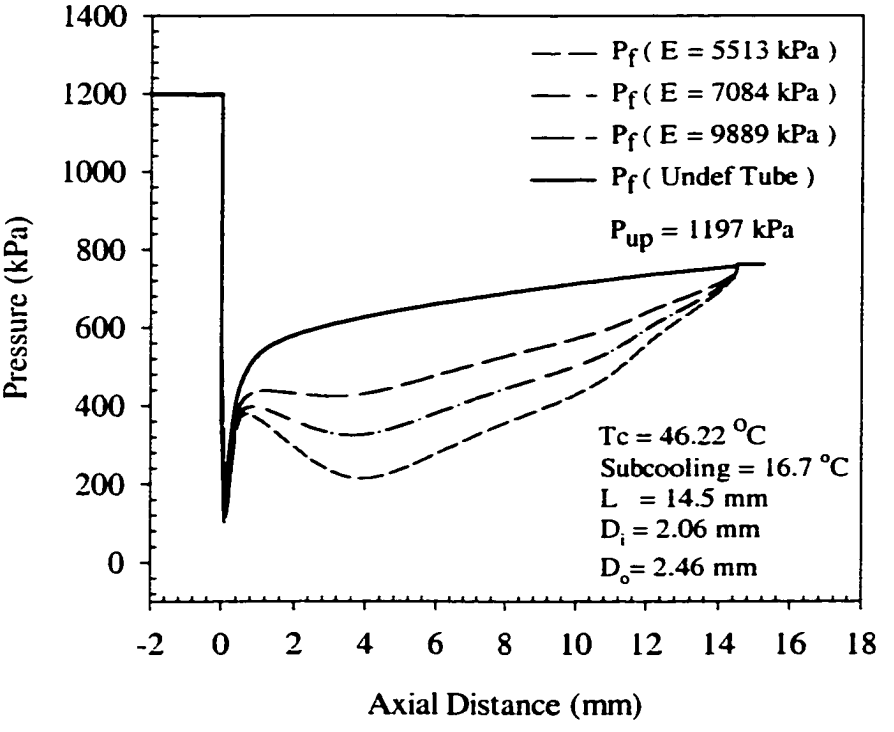

Figure 6.3a Pressure Profiles for R-134a Single Phase Flow through a Flexible Short Tube Orifice $(L/D)_t$ at Three Moduli of Elasticity.

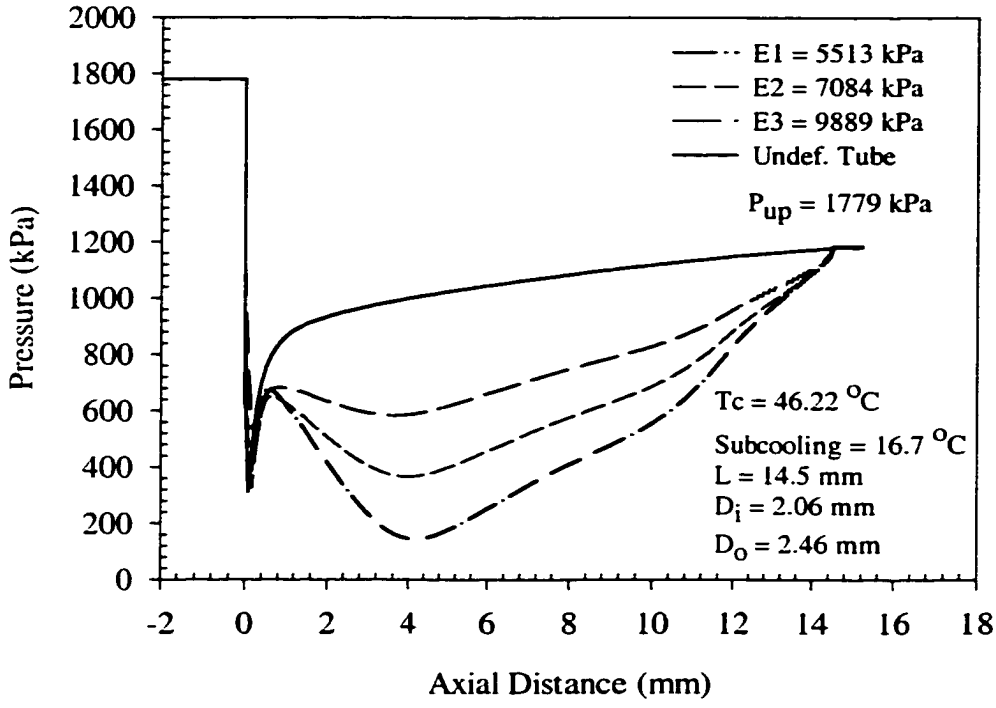

Figure 6.3b Pressure Profiles for R-22 Single Phase Flow through a Flexible Short Tube Orifice $(L/D)_1$ at Three Moduli of Elasticity.

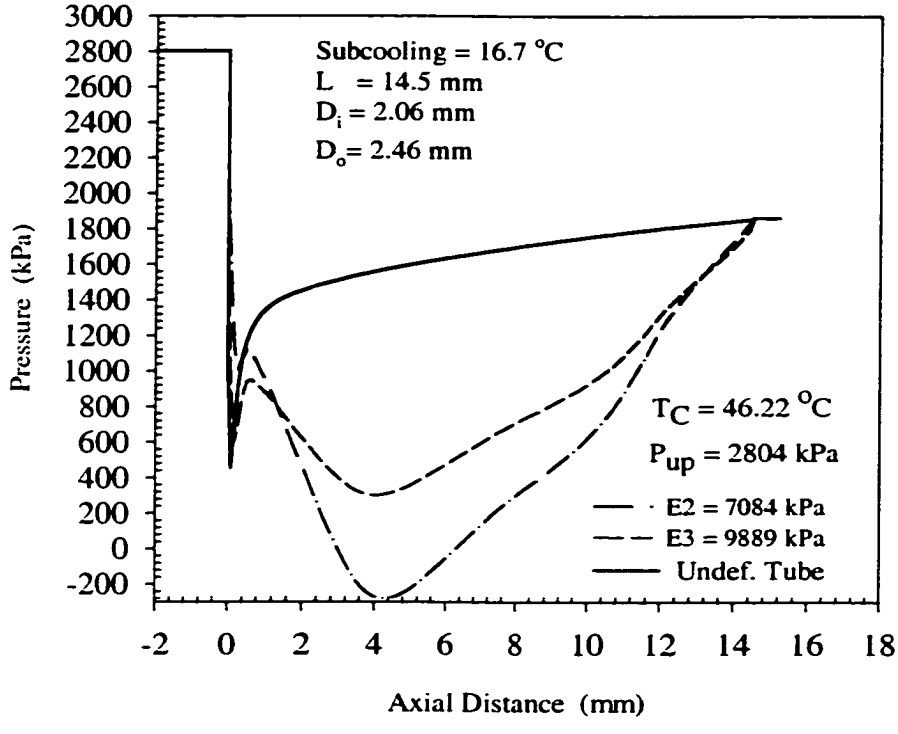

Figure 6.4 Pressure Profiles for R-410a Single Phase Flow through a Flexible Short Tube Orifice $(L/D)_1$ at Two Moduli of Elasticity.

the tube inlet. Figure 6.4 indicates that an unrealistic negative pressure was obtained almost at the minimum cross sectional area along the tube when the system used R-410a and for the more flexible tube. This could indicate the limit to the accuracy of the numerical scheme for such a large deformation for this upstream pressure. It is possible that reformation of the mesh would be needed for this case to more accurately estimate the pressure distribution. A significant pressure recovery downstream of the dip is shown in Figure 6.4 due to the larger diverging angle of the exit section of the tube after deformation.

Flexible Short Tube Deformation

The tube deforms as a result of the net force from the flow pressure difference between the internal and external sides. Figure 6.5 illustrates that the more flexible material had the higher tube radial displacement and, accordingly, the higher deformed and contracted cross sectional area. For the tube configuration, $(L/D)_1$, Figure 6.5 shows that as the modulus of elasticity decreased by 45% (tube flexibility increased), the radial displacement increased by 83%. The radial displacements are zero at both ends of the tube because of the constraint used at these ends (neglecting axial deformation compared to the radial deformation).

In a qualitatively similar fashion, Figure 6.6 displays the radial displacement of the tube as a result of flow of R-410a. The results show an excessive radial deformation of the tube compared to R-134a. This is due to the higher operating pressure of R-410a

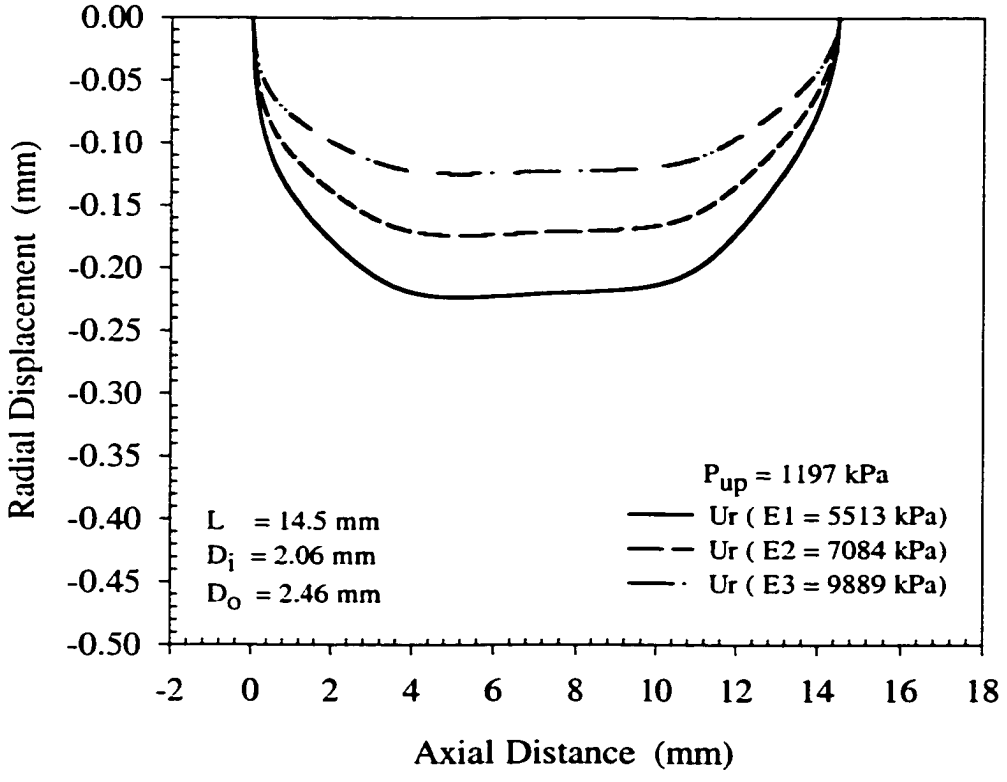

Figure 6.5 Radial Displacement Comparison along a Flexible Short Tube Orifice $(L/D)_t$ as a Result of R-134a Single Phase Flow at Three Moduli of Elasticity.

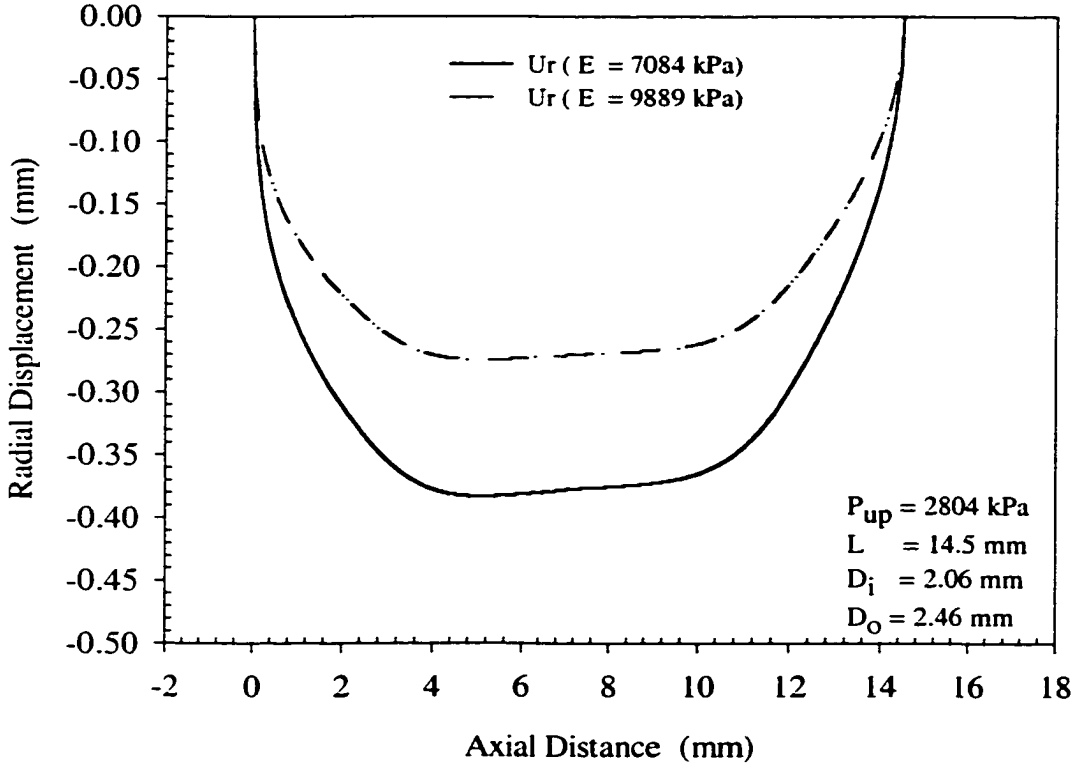

Figure 6.6 Radial Displacement Comparison along a Flexible Short Tube Orifice $(L/D)_i$ as a result of R-410a Single Phase Flow at Three Moduli of Elasticity.

over R-134a under the same condensing temperature. The radial displacement increased by almost 37% as the modulus of elasticity decreased by 28%.

The tube radial displacements were reformed into radius values (Figures 6.7 and 6.8) for R-134a and R-410a, respectively. This better helps in understanding the axial pressure variation along the tube. Figure 6.7 shows the gradual change in the tube shape as the modulus of elasticity decreased. The figure illustrates the inner tube area including the non deformed divergent area and the subsequent deformed converging-diverging-like area. A noticeable increase in the chamfering-like angle was observed at both tube inlet and exit as the modulus of elasticity decreased (flexibility increased). The minimum tube cross sectional area approximately occurred at an axial distance of almost 3.5 mm from the tube inlet. This explains the slight dip in the pressure profiles (Figure 6.3a). The deformed area was 36% of the undeformed area at this location. Further, the area decreased by 10% at this location as the tube modulus of elasticity decreased by 28% (from 9889 kPa to 7084 kPa).

When R-410a was used in the system for the same short tube geometry at two moduli of elasticity and under the same operating conditions, it yielded the deformed shape shown in Figure 6.8. The chamfered-like inlet and outlet are more visible, as shown in the figure, as well as the converging-diverging shape. This clearly justified the different changes in the pressure profiles (Figure 6.4). Quantitatively, the maximum percentage of reduction in the tube cross sectional area (almost 4 mm from the inlet) for the lower modulus of elasticity was 69 %. As the tube modulus of elasticity decreased by 28%, the reduction in tube diameter increased by 28%.

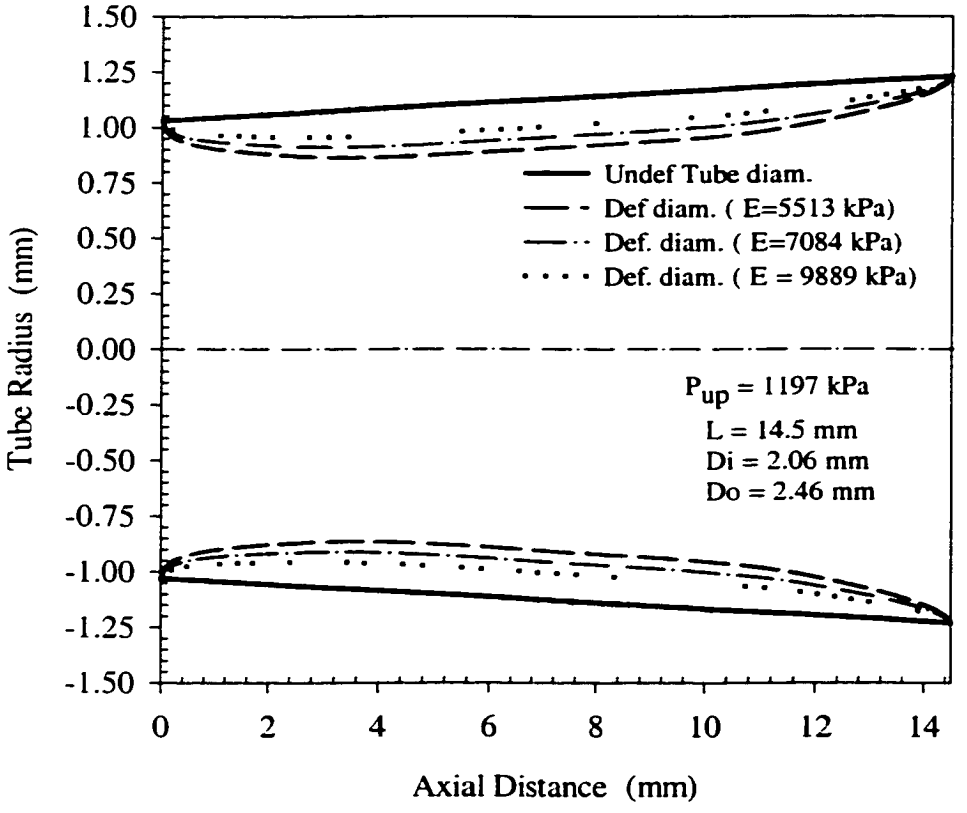

Figure 6.7 Short Tube $(L/D)_1$ Radius Variation along the Tube Axis as a Result of R-134a Single Phase Flow at Three Moduli of Elasticity.

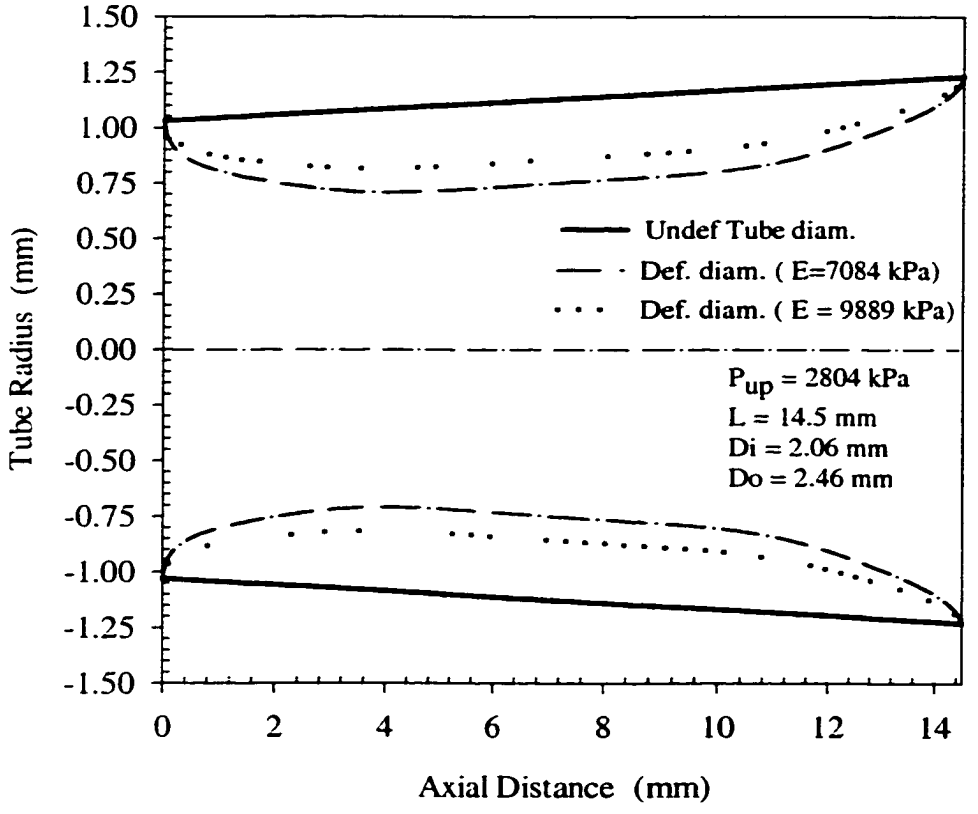

Figure 6.8 Short Tube $(L/D)_1$ Radius Variation along the Tube Axis as a Result of R-410a Single Phase Flow at Two Different Moduli of Elasticity.

Effect of Condenser Pressure on Pressure Profiles

The refrigerant pressure surrounding the external body of the flexible short tube is assumed constant and equal to the upstream pressure (Drucker 1992). Thereby, the upstream pressure variation is an important operating parameter to be considered. The pressure variation along the flexible short tube as the upstream pressure changed for the same evaporator temperature (29.5 °C) is presented in Figures 6.9 and 6.10 for R-134a and R-410a, respectively. R-134a exhibits approximately 35% less in operating pressure compared to R-22 at the same condensing temperature. The downstream pressure was always equal to or above the saturation pressure corresponding to the inlet temperature.

Figure 6.9 shows that as the inlet upstream pressure increased, the sharp pressure drop at the inlet edge of the tube increased for the same evaporating temperature. Increasing the pressure differential across the short tube orifice would increase the mass flow rate. The tube inlet loss is directly proportional to the mass flow rate. Therefore, increasing the pressure differential across the orifice increased the inlet loss and, accordingly increased the pressure drop at the inlet. Moreover, the axial pressure values decreased everywhere inside the tube from the upstream side to the downstream side. A smooth pressure recovery region very close to the tube inlet as a result of flow reattachment to the tube followed by a dip in the profiles was established as shown in the figure. Figure 6.9 indicates that the higher the upstream pressure the more observable dip at the same axial location. Increasing the upstream pressure would lead to an increase of

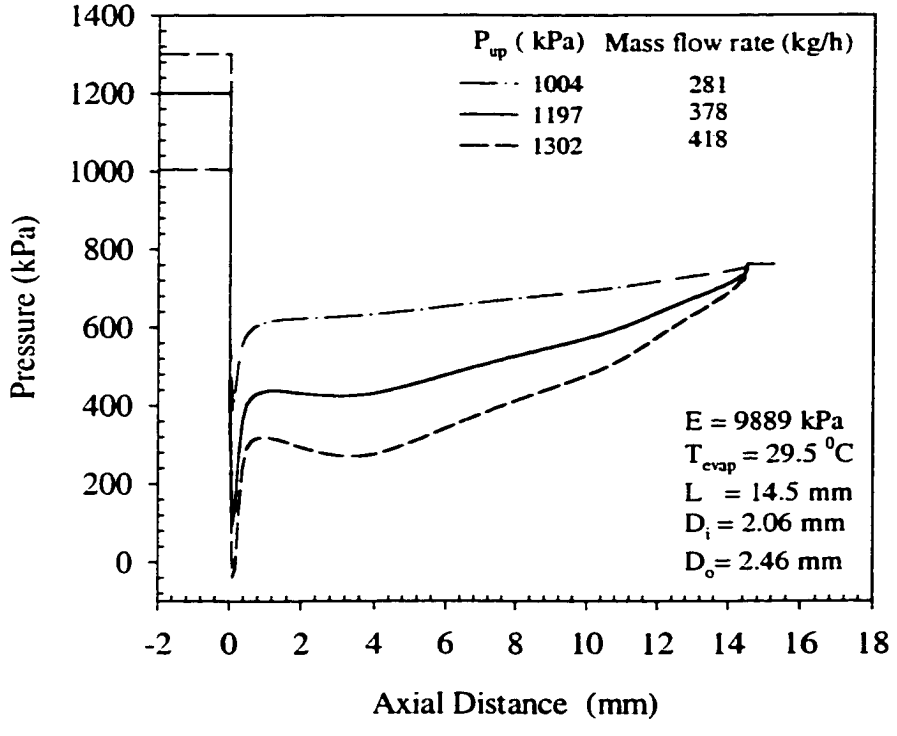

Figure 6.9 Pressure Profiles for R-134a Single Phase Flow through a Flexible Short Tube Orifice $(L/D)_1$ at Different Condensing Temperatures.

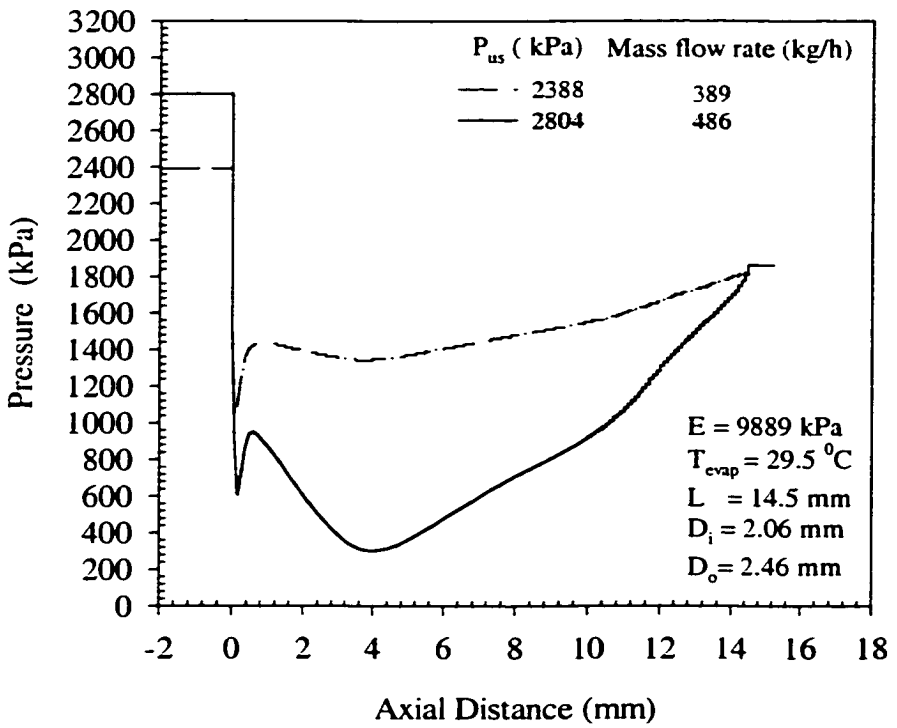

Figure 6.10 Pressure Profiles for R-410a Single Phase Flow through a Flexible Short Tube Orifice $(L/D)_1$ at Two Subcooling Temperatures.

the stresses on the tube material which accordingly leads the tube to constrict more than that at the lower upstream pressure. Quantitatively, as the upstream pressure increased from 1004 kPa to 1302 kPa (30%), the pressure at the dip decreased by 56%.

The effect of upstream pressure on the pressure profile for R-410a flow on the same tube configuration and under the same constant subcoolings is shown in Figure 6.10. Two upstream pressures are shown. Unrealistic negative internal pressures were calculated with R-410a at higher upstream pressures at an evaporating temperature at 29.5 °C. Figure 6.10 shows an increase of the pressure profile slope in the recovery region as the upstream pressure increased. This may be attributed to the larger divergent angle of the tube exit when the upstream pressure increased that decelerated the flow and increased the pressure.

Effect of Condenser Pressure on Tube Deformation

The final tube shape after deformation can be used to better understand the pressure profile trends along the tube. Figure 6.11 displays the effect of upstream pressure change on tube deformation for R-134a. The figure shows that the tube deformed more as the upstream pressure increased for the same material elasticity. This explains the pressure decrease along the tube as the upstream pressure increased (Figures 6.8). The change in the tube inner free area after deformation was small as the upstream pressure increased in the shown range. An increase in both inlet and exit cross section area was shown in the figure. This was experimentally observed by Kim et al (1996). As the upstream pressure increased, the average deformed diameter decreased due to the

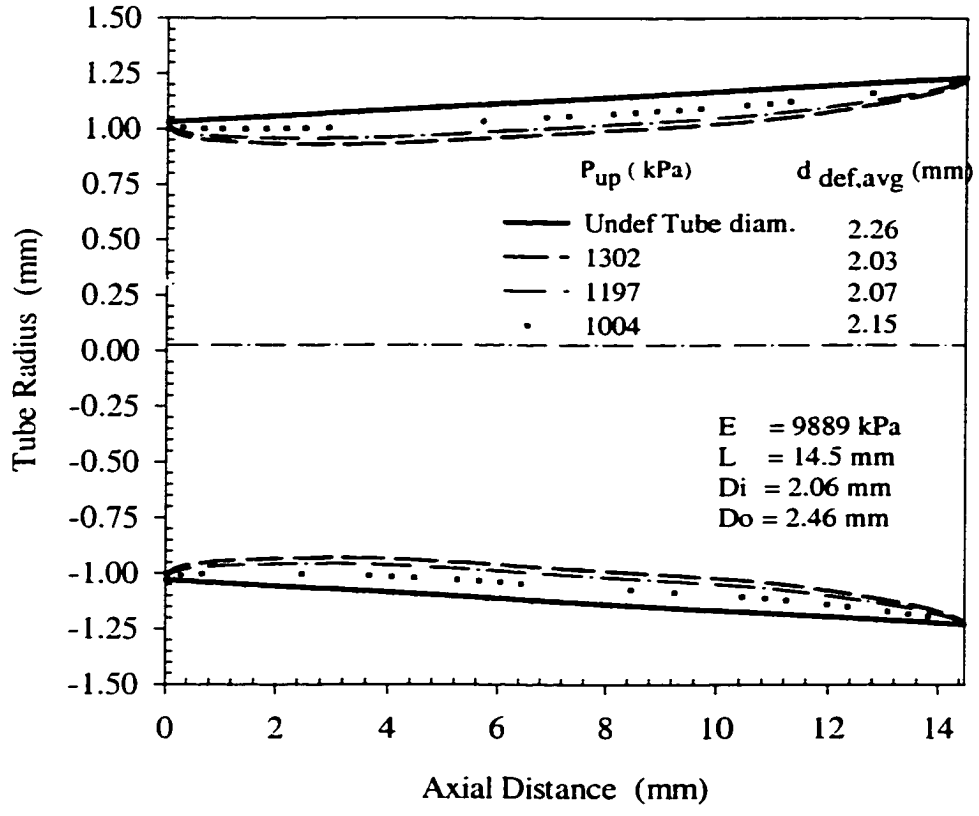

Figure 6.11 Short Tube $(L/D)_1$ Radius Variation along the Tube Axis as a Result of R-134a Single Phase Flow at Three Upstream Pressures.

increase of the force exerted on the tube outer surface for the same material. While the upstream pressure increased by 30%, the average tube diameter decreased by almost 6% for the higher modulus tube and within the chosen range of upstream conditions.

Similarly, Figure 6.12 illustrates the final estimated tube shape when R-410a was used in the system under the same subcoolings. The shape was for the higher modulus tube (9889 kPa). For the 5513 kPa case, unrealistic negative pressures were calculated. The figure shows that for R-410a, a 17% increase in the upstream pressure led to an 8% decrease in the tube deformed average diameter. It is shown the final converging-diverging nozzle shape of the tube after deformation including the chamfered-like shape at the inlet and exit of the tube. This shape extremely explains the pressure profiles trend shown in Figure 6.10. Comparing to Figure 6.8, it can be observed that the effect of changing the tube modulus of elasticity was as significant on tube deformation as that of changing the upstream pressure in the studied range.

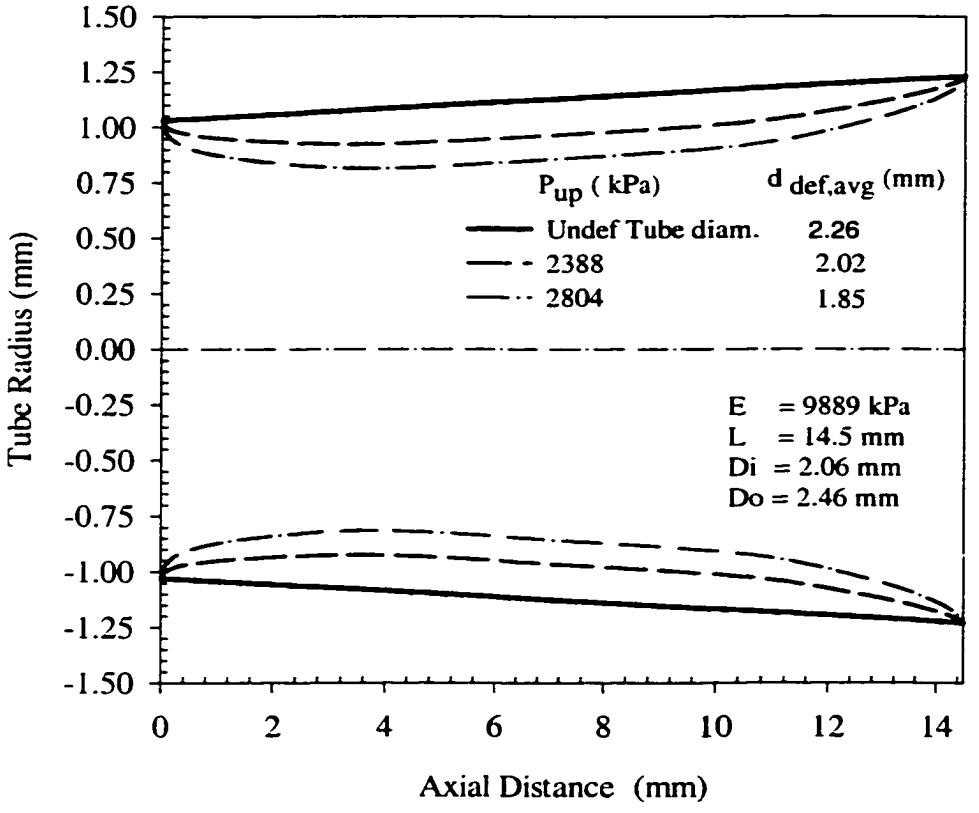

Figure 6.12 Short Tube $(L/D)_1$ Radius Variation along the Tube Axis as a Result of R-410a Single Phase Flow at Two Upstream Pressures.

Comparing R-22, R-134a, and R-410a Results

Under the same condensing and evaporating temperatures, each refrigerant has a different operating pressure. R-22 exhibits almost a 50% higher operating pressure than R-134a at the same condensing temperature. However, R-410a exhibits a 50% higher operating pressure than R-22 under the same condensing temperature. The condensing temperature used in the comparison was 46.2 °C. The corresponding upstream pressures were 1179 kPa, 1779 kPa , and 2804 kPa for R-134a, R-22, and R-410a, respectively.

Figure 6.13 shows the effect of using different refrigerants on the tube deformation of a flexible short tube orifice. The same evaporating and condensing temperatures were used in this figure. R-410a had the higher pressure difference and, accordingly the higher mass flow rate compared to R-22 and R-134a when the tube modulus of elasticity was almost above 7000 kPa. The flow rate of R-410a dropped rapidly as the modulus of elasticity decreased. In contrast, the flow rate is appeared to approach constant values for both R-134a and R-22. Generally, as the modulus of elasticity increases, the tube gets stiffer, and the mass flow rate increases. Once the tube modulus decreased beyond almost 7000 kPa, the tube could not resist the force exerted by R-410a, so it contracted so much that flow rate was actually below that of R-134a and R-22. Figure 6.13 shows that R-22 produced almost 14% higher flow rate than R-134a for the stiffer tube and almost 7% for the more flexible tube. This is due to the higher operating pressure of R-22 than R-134a under the same condensing and evaporating temperature. On the other hand, R-410a had almost a 13% higher flow rate than R-22

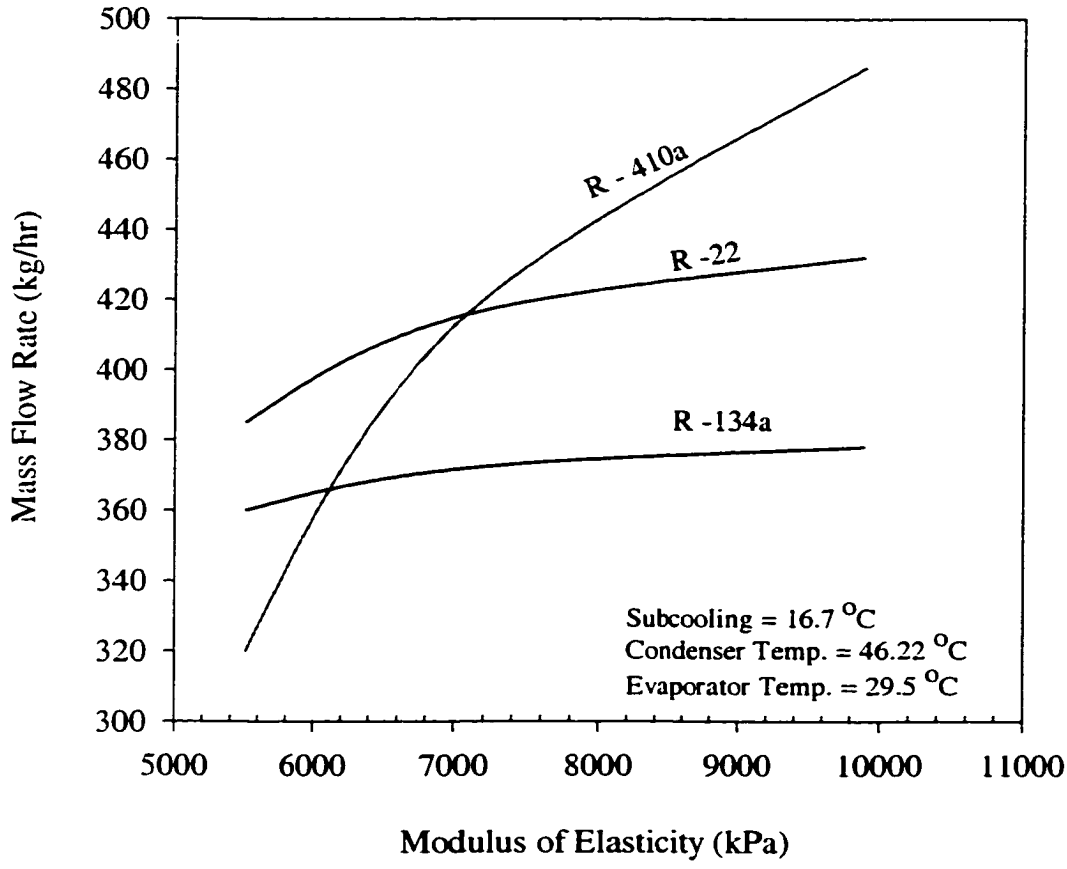

Figure 6.13 Mass Flow Rate Variation versus Modulus of Elasticity When Different Refrigerants Flow through a Flexible Short Tube $(L/D)_t$ under the Same Condensing and Evaporating Temperatures.

and a 29% higher than R-134a for the stiffer tube. However, due to the larger deformation for the more flexible tube, the mass flow of R-410a sharply decreased to almost 17% less than R-22 and 11% less than R-134a. Although Figure 6.14 displays that R-410a had the lowest diameter ratio for all moduli, it produced the higher flow rate as the tube gets stiffer due to the higher pressure differential it had within the same condensing and evaporating temperatures.

Figure 6.14 shows the diameter ratio ($D_{def,avg}/D_{undef,avg}$) variation as a function of the tube modulus of elasticity. Qualitatively, all three refrigerants exhibited a similar trend as the tube modulus increased. R-410a yielded the lowest diameter ratio meaning the highest deformed shape of the tube. A slope change is shown in the figure when the modulus decreased below almost 7000 kPa. This may indicate an overly deformation of the tube when R-410a was run through tubes with lower modulus of elasticity. Figure 6.14 also displays that beyond a modulus of elasticity of nearly 7000 kPa, there was a tendency of the diameter ratio to significantly decrease. Quantitatively, at a modulus of elasticity of 7084 kPa, R-22 had almost a 5% more effect on tube deformation than R-134a; while R-410a produced 11-15% tube deformation more than R-22 and R-134a, respectively.

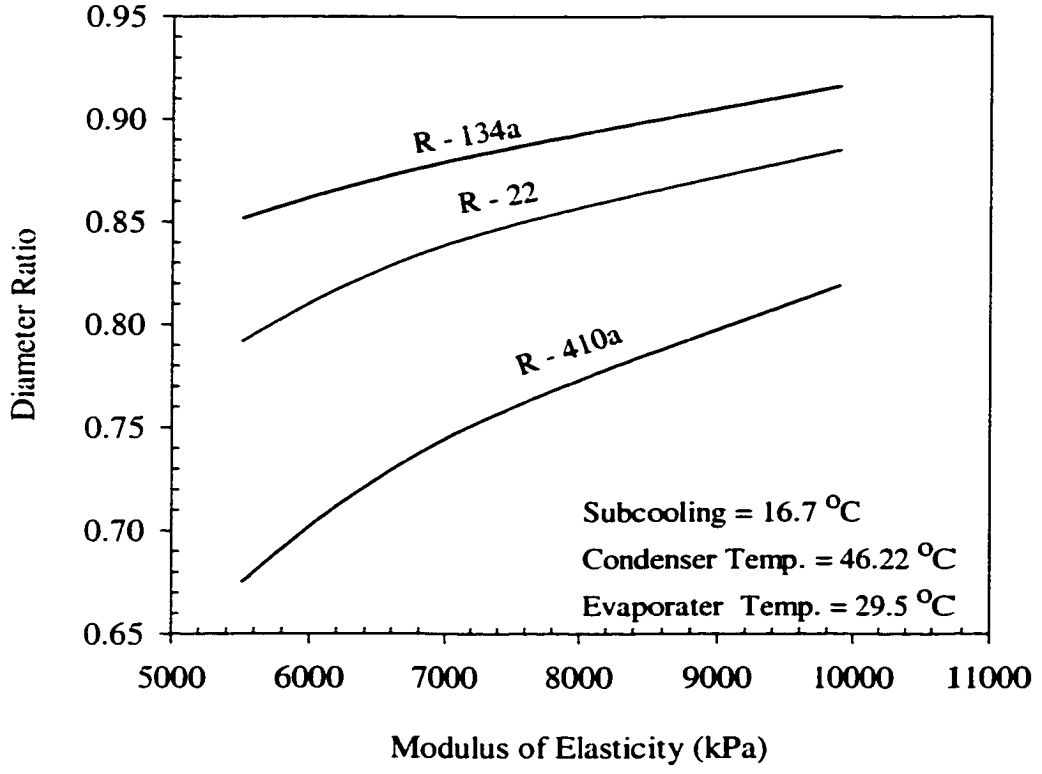

Figure 6.14 Diameter Ratio Variation versus Tube Modulus of Elasticity When Different Refrigerants Are Run through a Flexible Short Tube $(L/D)_1$.

CHAPTER VII

CONCLUSIONS AND RECOMMENDATIONS

The concern of this study was modeling single-phase flow of refrigerants R-22, R-134a, and R-410a through flexible short tube orifices with L/D ratios ranging from 5.5 to 11.5. Two moduli of elasticity (7084 kPa, and 9889 kPa) typical to the true manufactured tube material modulus of elasticity in addition to a lower modulus of elasticity (5513 kPa) were evaluated. A FEM commercial package, ANSYS with its CFD counterpart, FLOTRAN, was used to model the flow and deformation of the tube. Upstream pressure values were chosen as those typical to heat pump operating conditions. For R-22, the upstream pressures were 1179 kPa, 1455 kPa, 1779 kPa, and 2144 kPa. For R-134a and R-410a, the study focused on only one L/D ratio and considered three different condensing temperatures, 39.49 °C, 46.22 °C, and 49.5 °C keeping the same evaporating temperature, 29.5 °C. A published experimental study for refrigerant mass flow rate of R-22 through a flexible short tube (Kim et al 1996) and a comprehensive experimental work on rigid short tube orifices (Kim 1993) were used as baselines for model validation.

Conclusions

For all refrigerants flowing through all L/D ratios and under all the operating conditions, the tube shape resembled a converging-diverging nozzle when deformed. Interestingly, the tube had a chamfered-like angle and depth at both the inlet and outlet as

a result of deformation. The angle and depth of this deformation changed as a function of the tube flexibility as well as the applied load resulting from the upstream pressure. A significant increase in the chamfering-like inlet angle (5° to 8°) was observed as the modulus of elasticity decreased. The more flexible the tube, the less pressure drop at the tube inlet due to the increase of the chamfered-like inlet after deformation. However, as the tube got more flexible, there was a higher pressure drop along the tube due to the higher tube contraction area. Quantitatively, while the modulus of elasticity decreased (flexibility increased) by 28%, the maximum pressure drop at the dip (almost 4 mm from the short tube inlet) increased. This increase was nearly 21% for (L/D_1), 28% for (L/D_2), and 42% for (L/D_3) for the lowest modulus tube over the stiff tube and for R-22. Therefore, increasing the tube inner diameter, for the same tube length, produced a significant change in the pressure profiles compared to those for increasing the tube length under the same upstream pressure. Hence, the diameter has a significant effect on pressure drop and accordingly on mass flow rate relative to the tube length.

As the modulus of elasticity decreased, the mass flow rate decreased for all upstream pressures due to the increased cross sectional area contraction. Similarly, as the upstream pressure increased, the mass flow rate increased for all moduli of elasticity; however, the lower modulus of elasticity exhibited a lower flow rate that tended to decrease as the upstream pressure increased indicating a higher contraction in the tube cross sectional area. The maximum percentages of reduction in tube diameter (L/D_1) at almost 4 mm from the inlet for the lowest modulus of elasticity were 20% and 32%, respectively when the upstream pressure increased from 1179 kPa, to 2144 kPa. However, for (L/D_2), the tube internal area contracted 36% under 1179 kPa upstream

pressure, while this percentage was nearly 54% under the higher upstream pressure, 2144 kPa. For (L/D_3), the tube internal area contracted by 38% and 57% of the original non deformed area when the upstream pressure increased from 1179 kPa to 2144 kPa.

A comparison between the estimated mass flow rates with those from the experiments showed a close agreement. The only experimental data were for R-22. However, the numerically estimated mass flow rates were almost 14% higher than the experimental results. The study showed that the more flexible tube restricted the mass flow rate by 2 to 6% less than the less flexible tube one depending on the upstream pressure.

Results for both R-134a and R-410a qualitatively showed very similar trends to R-22. However, the tube was more constrained in the case of R-410a and less constrained in the case of R-134a compared to R-22 at the same condensing temperature, (46°C). For R-134a, the minimum tube cross sectional area occurred at an axial distance approximately equal to 3 mm from the tube inlet. The maximum percentage of reduction in the area at this location was 36%. However, for R-410a, this percentage of reduction of tube diameter for the lower modulus of elasticity was 43 %. At the same condensing temperature, R-410a has nearly 50% more upstream pressure than R-22, while the upstream pressure for R-134a was almost 35% below R-22. Therefore, for the same modulus of elasticity, R-410a showed a higher mass flow rate than R-22, while R-134a showed a less flow rate compared to R-22. Quantitatively, at a modulus of elasticity of 7084 kPa, R-22 had a 5% higher tube deformation than R-134a, while R-410a produced 11% more deformation than R-22. The mass flow rate for the stiff tube (9889 kPa), was

almost 14% higher for R-22 due to the higher pressure differential for the same condensing and evaporating temperature. On the other hand R-410a had almost 13% higher than R-22 and 29% higher than R-134a.

The FEM model produced physically realistic results as long as the tube deformation was not too large. As the tube elasticity increased and/or the applied pressure load excessively increased. the model showed unrealistic pressure distribution results which might indicate the collapse of the tube. Moreover, the model yielded a reasonable visualization of pressure distribution and tube deformation that would be difficult to measure through experiments due to the flexible short tube geometry. The model predicted reasonable flow rates compared to published experimental results.

Recommendations

Although this study dealt with single-phase flow, the true applications of refrigerant flow in heat pumps are mostly two-phase flow. This study provided a starting point for understanding how the flexible orifices deform for a range of variables (L/D), upstream pressure, and modulus of elasticity). Thus, it can serve as a base for future investigations of two-phase flow through flexible short tube orifices.

There is still a need for more experimental evaluation of flow through flexible short tube orifices, particularly, measuring the pressure variation along the tube under deformation.. The present study dealt with an internally tapered tube because experimental data were available. Investigating different tube aspect ratios with certain

chamfering at the tube inlet in addition to tube internal shape is highly recommended. A wider range of tube flexibility can be also taken into consideration.

There are a number of new refrigerants whose behavior through flexible short tube might be tested under different operating conditions. Moreover, refrigerant flow with which a certain percentage of oil is mixed, as the case in true heat pump applications, is recommended for future study to investigate the effect of oil on flexible short tube behavior

Unrealistic pressure distribution results for an excessive tube deformation were shown. This phenomenon could be primarily caused by an improper grid generation. Thus, a mesh regeneration with either unstructured elements and/or with different element degrees could be recommended for such case. Horizontal as well as vertical displacement constraints were applied to both ends of the tube. Unconstraining the upstream end of the tube may provide more realistic results in that case.

The limitations on the application of the estimated mass flow rate model was noted earlier. Therefore, the model would need to be modified to have wider applications. This modified model could take into consideration the effect of oil contamination, different tube geometries, and be more general for any refrigerant.

REFERENCES

Aaron, A. A., Domanski, P. A. 1990. Experimentation, analysis, and correlation of refrigerant-22 flow through short tube restrictors. *ASHRAE Transactions* 96(1): 729-742.

Bailey, J. F. 1951. Metastable flow of saturated water. *Trans of ASME.* 73: 1109-1116.

Baxter, V., Fischer, S., and Sand, J. R. 1998. Global warming implications of replacing ozone-depleting refrigerants. *ASHRAE Journal* 40(9): 23-30.

Chisholm, D. 1967a. Flow of incompressible two-phase mixtures through sharp-edged orifices. *Journal of Mechanical Eng. Science* 9(1): 72-77.

Chisholm, D. 1967b. Flow of compressible two-phase mixtures through throttling devices. *Chemical and Process Eng.* 48: 73-78.

Davies, D., and Daniels, T. C. 1973. Single and two-phase flow of dichloro-difluoromethane (R-12) through sharp-edged orifice. *ASHRAE Transactions* 79(1): 109-123.

Drucker, A. S. 1992. Variable area refrigerant expansion device having a flexible orifice. US Patent 5134860.

Drucker, A. S. and Abbott, A. D. 1993. Variable area refrigerant expansion device having a flexible orifice. US Patent 5214939.

Drucker, A. S. and Cann, P. L. 1991. Variable area refrigerant expansion device having a flexible orifice. US Patent 5031416.

Erbay, H. A. and Demiray, H. 1995. Finite axisymmetric deformations of elastic tubes: an approximation method. *J Engng. Math.* (29): 451-472.

Fauske, H. K. 1962. Contribution to the theory of two-phase, one-component critical flow, ANL-6633. Chicago: Argonne National Laboratory.

Ferziger, J. H., and Peric, M. 1997. *Computational Methods for Fluid Dynamics.* Berlin: Springer-Verlag.

Goldstein, S. D. 1981. A computer simulation method for describing two-phase flashing flow in small diameter tubes. *ASHRAE Transactions* (2):151-194.

Henry, R. E. and Fauske, H. K. 1971. The two-phase critical flow of one-component mixtures in nozzles, orifices, and short tubes. *J of Heat Transfer, Trans ASME,* 93: *May,* 179-187.

Hsu, Y. Y. and Graham, R. W. 1976. *Transport Process in Boiling and Two-Phase System*. New York: Hemisphere Publishing Co.

Kim, Y. 1993. Two-phase flow of HCFC-22 and HFC-134a through short-tube orifices. Ph.D. Dissertation, Texas A&M University, College Station, TX.

Kim, Y. and O'Neal D. L. 1995. A comparison of critical flow models for estimating two-phase flow of HCFC-22 and HFC-134a through short tube orifices. *Int. J. Refrig*. 00(0): 1-9.

Kim, Y. and O'Neal D. L.1994a. Two-Phase flow of R-22 through short-tube orifices. *ASHRAE Transactions* 100(1): 323-334.

Kim, Y. and O'Neal, D. L. 1994b. A semi-empirical model of two-phase flow of refrigerant-134a through short tube orifices. *Experimental Thermal and Fluid Science*, 9(4): 426-435.

Kim, Y. C., O'Neal, D. L., and Payne, W. V. 1996. Characteristics of refrigerant flow through flexible short tube orifices. Report ESL/TR-94/CA01, Energy System Laboratory, Texas A&M University, College Station, TX.

Krakow, K. I. and Lin, S. 1988. Refrigerant flow through orifices. *ASHRAE Transactions* 94(1): 484-506.

Kuehl, S. J. and Goldschmidt, V. W. 1992. Flow of R-22 through short-tube restrictors. *ASHRAE Transactions* 98(2): 59-64.

Levy, S. 1965. Prediction of two-phase critical flow rate. *J of Heat Transfer, Trans ASME Series C* 87(1): 53-58.

Mei, V. C. 1982. Short tube refrigerant restrictors. *ASHRAE Transactions* 88(2): 157-168.

Mikol, E. P. 1963. Adiabatic single and two-phase flow in small bore tubes. *ASHRAE Journal*, November: 75-86.

Moody, F. J. 1965. Maximum flow rate of a single component two-phase mixture. *J of Heat Transfer, Trans ASME Series C* 87(1): 134-142.

Nallasamy, M. 1987. Turbulence models and their applications to the prediction of internal flows: A review. *Computers and Fluids* 15(2): 151-194.

Reddy, J. N. 1993. *An Introduction to the Finite Elements Method*. New York: McGraw-Hill Book Company.

Rodi, W. 1993. *Turbulence Models and their Applications in Hydraulics: A state-of-the-art review*. Rotterdam, The Netherlands: A. A. Balkema.

Sajben, M. 1961. Adiabatic flow of flashing liquids in pipes. *J of Basic Eng., Trans. ASME* 83: 619-631.

Starkman, E. S., Schrock, V. E., Neusen, K. F., and Maneely, D. J. 1964. Expansion of a very low quality two-phase fluid through a convergent-divergent nozzle. *J of Basic Eng., Trans. ASME* 86: 247-255.

Swanson Analysis System, Inc 1995. *Theory*. Vol IV, *ANSYS User's Manual*. Houston, PA.

Tannehill, J. C., Anderson, D. A., and Pletcher, R. H. 1997. *Computational Fluid Mechanics and Heat Transfer*. Second Edition. Washington, DC: Taylor and Francis.

Versteeg, K H and Malalasekera, W. 1995. *An Introduction to Computational Fluid Dynamics, The Finite Volume Method*. Harlow, Essex, England: Longman.

Wallis, G. B. 1969. *One-Dimensional Two-Phase Flow*. New York: McGraw-Hill Book Company.

Wallis, G. B. 1980. Critical two-phase flow. *Int. J Multiphase Flow* 6: 97-112.

Zaloudek, F. R. 1963. The critical flow of hot water through short tubes. HW-77594, Hanford, WA: Hanford Laboratory.

VITA

Ramadan Bassiouny Mohamed Abdel Ghani was born on December 25, 1965, in Burgaya, Minia, Egypt. Upon completing high school, he was admitted to the undergraduate studies at the Faculty of Engineering and Technology, Minia University. In 1987, he was sent by his faculty to Jordan for training. After graduation with a bachelor's degree from the Department of Mechanical Engineering as the first of his class in 1988, Ramadan was appointed a teaching assistant in the same department. In 1989 he joined the Egyptian army for one year in which he worked with GTE, USA Telephone Company. Then, he enrolled at Minia University for the master's degree in 1990. In 1993, he finished his M.S. degree from the Department of Mechanical Engineering at Minia University. From 1993 till the Spring of 1996, he worked as a teaching assistant at the same department. In the Spring of 1996, he was awarded a mission from the Egyptian government to travel to the U.S. for a Ph.D. degree. Upon arrival in the U.S., he joined the Doctoral program in Mechanical Engineering at Texas A&M University in the Summer of 1996. His area of interest was thermal fluids, HVAC, and CFD.

Ramadan is married and has a cheerful daughter and son named Esra' and Tareq. His permanent mailing address is: Department of Mechanical Engineering, Faculty of Engineering and Technology, Minia University, Minia 61111, EGYPT.